Advances in Urban Ventilation Assessments using Large-Eddy Simulation

Von der Fakultät für Mathematik und Physik
der Gottfried Wilhelm Leibniz Universität Hannover

zur Erlangung des akademischen Grades
Doktor der Naturwissenschaften
Dr. rer. nat.

genehmigte Dissertation von

M.Sc. Tobias Gronemeier

2021

Abstract

Today, the majority of the world's population lives in city areas. This renders the urban climate to be the most impacting local climate to the global society. To understand and improve the urban climate, local governments demand urban ventilation assessments (UVAs). Such UVAs often simplify the highly complex urban climate in order to make an assessment possible. In order to simplify the assessed case, the general behaviour of the urban ventilation must be understood so that important impacts are not neglected. However, many interactions inside the urban atmospheric boundary layer are still unknown. In this thesis, two aspects of these unknown interactions of urban climate are studied in detail: (a) the ventilation of courtyards, particularly, the influence of lateral openings on courtyard ventilation; and (b) the interaction between neighbourhood ventilation and mean building parameters like mean building height and building density under different atmospheric stratification. These two aspects are investigated by means of large-eddy simulations.

To confirm the liability of the utilized simulation model PALM, an evaluation study was conducted prior to the investigation of the two above-mentioned aspects. The comparison of simulation results against wind-tunnel data revealed differences in mean wind speed and wind direction of 5 % and 4°, respectively, on average. The maximum differences occurred within the first grid points adjacent to obstacles and rapidly decreased with distance. Turbulence parameters like turbulence intensity and the spectral energy-density distribution agreed to a similar degree. Differences were found to be well within the acceptable margins. Hence, it was concluded that the model is able to correctly simulate the urban boundary layer.

In the following part, the ventilation of courtyards through lateral openings was investigated. Various courtyard configurations were analysed in an idealized building setup. Lateral openings were found to have nearly no effect on the ventilation of wide courtyards. However, for deep courtyards, pollutant concentration and the residence time of pollutants were found to be significantly influenced by lateral openings. Most configurations showed a negative impact on air quality by lateral openings. Depending on the placement of the opening and the surrounding ventilation conditions, however, lateral openings could also positively impact the air quality by removing pollutants. It could be shown that the impact of lateral openings is complex and should not be neglected in case of building-scale ventilation assessments.

In the last part of this thesis, the effect of atmospheric stratification on the ventilation of neighbourhood areas was investigated. In a real-case building setup of Hong Kong city, the ventilation was compared for neutral and unstable stratification in a weak-wind summer scenario. It was found that the overall ventilation is higher in an unstably stratified atmosphere due to the enhanced vertical mixing. The correlation between the plan area index (building density) and the ventilation was found to be stronger under unstable conditions compared to neutral stratification. Mean building height, however, was found to have no significant impact on the ventilation which contradicted findings by other studies. It could be shown that the overall ventilation differs between neutral and unstable stratification. To get an overall estimation of the city ventilation, UVAs should therefore cover different stratification scenarios.

Keywords: courtyard ventilation, large-eddy simulation, urban boundary layer, urban ventilation

Contents

List of Abbreviations

ABL	Atmospheric boundary layer
CFD	Computational fluid dynamics
CFL	Courant-Friedrichs-Lewy (time-step criterion)
DNS	Direct numerical simulation
EWTL	Environmental Wind Tunnel Laboratory (located at the University of Hamburg, Germany)
IBL	Internal boundary layer
LES	Large-eddy simulation
LPM	Lagrangian particle model
ML	Mixed layer
MOST	Monin-Obukhov similarity theory (Ähnlichkeitstheory)
RANS	Reynolds-averaged Navier-Stokes
SGS	Sub-grid scale
TKE	Turbulent kinetic energy
UBL	Urban boundary layer
UVA	Urban ventilation assessment

1 Introduction

Over half of the global population lives in city areas (UN-Habitat, 2013). It is estimated that this percentage increases to 68 % by 2050 (UN-Habitat, 2020). As a result, the majority of the world's population experiences an urban climate every day. Hence, the urban climate is the most important local climate for the global society.

A measure to achieve and guarantee a healthy urban climate is to ensure good ventilation of urban areas which mitigates, for example, air pollution and heat stress. In order to improve and sustain proper ventilation, local governments demand ventilation assessments as part of the planning process of building construction or city development (e.g. Ng, 2009; Ministerium für Verkehr und Infrastruktur Baden-Württemberg, 2015). Such urban ventilation assessments (UVAs) focus on different aspects of city climate like wind and thermal comfort, as well as air quality. High wind speeds reduce the wind comfort and can even impose health risks to pedestrians (e.g. Blocken and Carmeliet, 2004). Strong gusts make walking and cycling through streets or sitting in outside restaurants uncomfortable or even dangerous (Lawson and Penwarden, 1975). Thermal comfort focuses on the thermal sensation of people and evaluates temperature, radiation and wind speed together with the human energy balance to distinguish between cosy or hot/cold sensation. While UVAs regularly focus on thermal discomfort due to cold and windy environments, the majority of studies aim at heat events, which will become more common within the context of global warming (e.g. Cheung and Hart, 2014). In warm or even hot situations, well ventilated cities offer good thermal comfort by mixing cooler air from rural areas into the heated urban environment reducing the heat stress of city dwellers. Another important aspect of city ventilation is air quality. Cities are densely packed with pollutant sources like car traffic or emissions from domestic fuel (Fenger, 1999). The resulting air pollution imposes serious health risks on the urban population and is accounted for 2 % of world-wide deaths (World Health Organization, 2009). Proper ventilation increases the pollutant removal and enhances the air quality.

It is crucial to consider all relevant aspects of the city morphology that affect ventilation when conducting a UVA. However, urban areas are highly complex with varying obstacle shapes, surface properties as well as a variety of heat and pollutant sources. This results in a deeply heterogeneous urban climate, both, in horizontal and vertical direction. The complex interactions between the different parameters and their effect on the local city climate including the ventilation are still not entirely identified (e.g. Oke, 1987, 2006; Barlow, 2014). Due to this, UVAs tend to and often must simplify the considered situation when assessing the ventilation (e.g. Shi et al., 2015), because the high complexity cannot be fully covered by current assessment methods. Such methods include field measurements, wind-tunnel studies, and computational fluid dynamics (CFD) simulations. Field measurements can only cover very limited areas, and relevant aspects of city ventilation can easily be overseen by the sparse measurement locations. Within wind tunnel studies, larger amounts of measurement locations can be achieved with less expenditure compared to field measurements. However, atmospheric stability is very rarely covered by wind-tunnel experiments as this is physically challenging (Degrazia et al., 2018; Marucci et al., 2018). CFD simulations have the benefit to provide entire three-dimensional and time-dependent information of the studied area. However, they are, like wind-tunnel experiments, merely an imperfect model of the reality and do not include every detail. For example, turbulence and its effects on temperature and pollution concentration is often parameterized instead of directly simulated. Also, depend-

ing on the resolution of the simulation, building geometries are reduced in order to decrease computational costs to a reasonable amount. All these assumptions, however, can result in differences between the outcome of ventilation assessments and the ventilation patterns in reality. It is therefore crucial to know which assumptions can be applied in which situation.

In order to improve urban ventilation assessments, the various interactions between all aspects of the urban canopy and the urban ventilation behaviour are subject to extensive research (Buccolieri and Hang, 2019). These investigations include, but are not limited to,

- the influence of vegetation or other obstacles on pollutant dispersion and ventilation patterns (e.g. Chew et al., 2017; Santiago et al., 2017; Hong et al., 2018; Liu et al., 2018),

- interaction between indoor and outdoor ventilation (e.g. Bo et al., 2017; Suszanowicz, 2018),

- annual variation of ventilation depending on the season and local climate zones (e.g. Dong et al., 2017; Tan and Deng, 2017),

- effects of building layout on ventilation (e.g. Letzel et al., 2012; Yuan et al., 2017; Kurppa et al., 2018), and

- the influence of pollutant sources on the pollution distribution within the urban canopy (e.g. Kwak et al., 2018; Ming et al., 2018; Nguyen et al., 2018).

Within the present work, two aspects are analysed in detail that have a high potential to alter ventilation patterns but are often neglected by urban ventilation assessments: How do courtyard openings modify the ventilation of courtyard cavities and what is the effect of unstable stratification on the correlation between building parameters and city ventilation? Both of these questions aim at the understanding of the urban ventilation and are essential to better plan well-ventilated urban areas. These topics are tackles by utilizing the large-eddy simulation (LES) model PALM (Raasch and Schröter, 2001; Maronga et al., 2015, 2020). In Section 3, the model PALM is evaluated against wind-tunnel experiments to prove PALM's capability to adequately simulate an urban boundary layer flow. After the successful evaluation, the ventilation at building scale is focused in Section 4. It is investigated, if building features, like courtyard openings, have a significant influence on the ventilation patterns of single building blocks. In Section 5, the focus shifts towards a broader look on city ventilation at the scale of single neighbourhoods or city quarters where the atmospheric stratification has a critical influence on the ventilation. The evaluation of PALM and the consequences of considering the two mentioned influence factors (courtyard openings and unstable stratification) on the outcome of ventilation assessments are reviewed and presented in three research articles.

1.1 The Structure of the Urban Boundary Layer

The ventilation patterns of an urban area are strongly influenced by the conditions within the urban boundary layer (UBL). Differences in momentum, heat and humidity fluxes between an urban area and its rural surroundings trigger the development of the UBL (see Fig. 1.1). The UBL can reach to the top of the atmospheric boundary layer (ABL) over large urban areas or in strongly convective conditions, replacing any residual layer from the upwind area.

Large variations of roughness lengths as well as thermal and humidity fluxes do not only exist between an urban area and its rural surroundings but also within the city due to the heterogeneous distribution of buildings, green spaces and water areas, as well as the variety
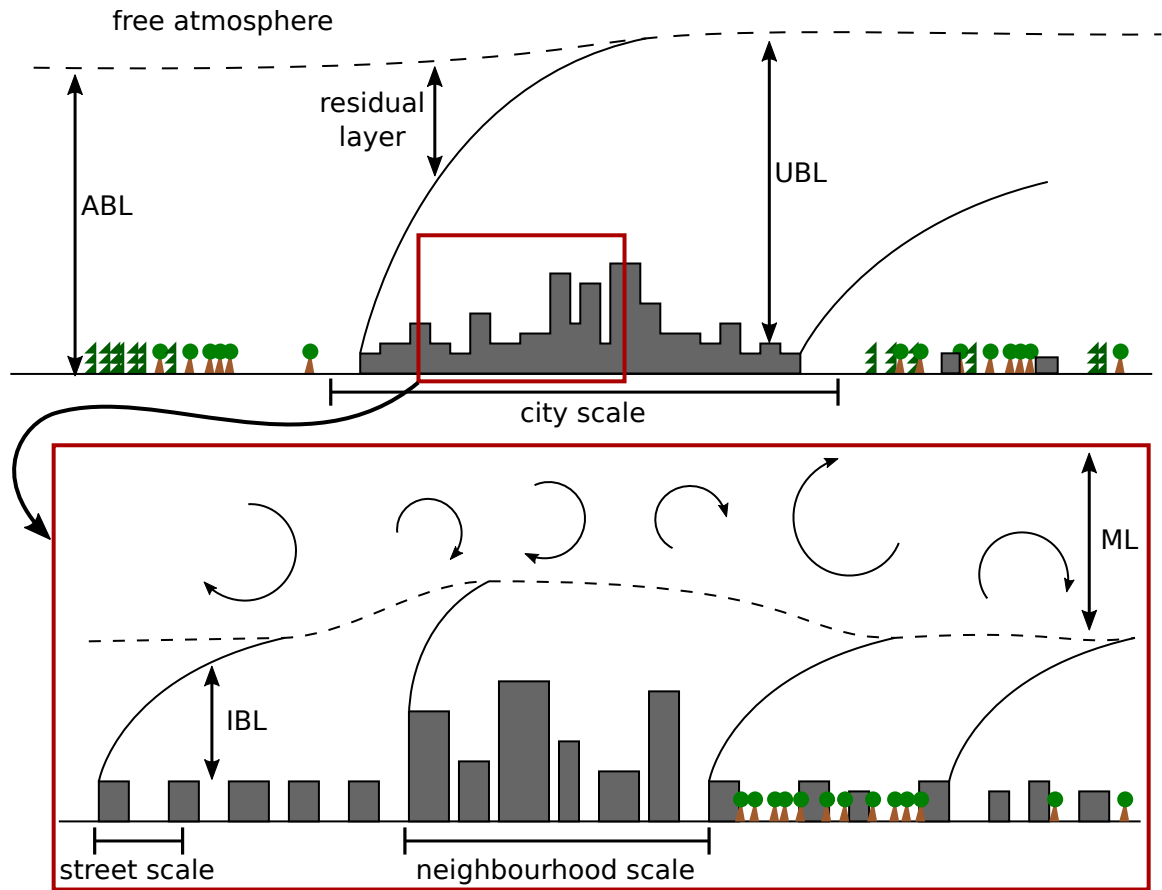
Figure 1.1: General structure of the urban boundary layer.

of used materials. This forms a complex three-dimensional structure of the UBL. Areas of similar mean surface properties create local internal boundary layers (IBL). Above the IBLs, a mixed layer (ML) is formed due to the generally high heat flux within an urban area. The ML forms the upper part of the UBL and reaches to the top of the ABL. In cases of a weak heat flux or at the windward city border, a residual layer is present above the UBL.

The different effects and mechanisms within the UBL can be divided into three different scales: the building or street scale $(10\,\text{m} - 100\,\text{m})$, the neighbourhood scale $(100\,\text{m} - 1000\,\text{m})$ and the city scale $(10\,\text{km} - 20\,\text{km})$ (Britter and Hanna, 2003; Barlow, 2014). When focusing on ventilation, the actual building properties such as shape and surface materials have a large influence on the building or street scale. Tall buildings, for example, can increase turbulence and the mean wind speed at pedestrian height level (e.g. Blocken and Carmeliet, 2004). Bulk parameters like mean building height or building density are of more importance on the neighbourhood scale and affect the development of the IBLs (e.g. Grimmond and Oke, 1999). On the city scale, large-scale features of the rural surroundings affect the city ventilation and influence the overall UBL formation and structure. Such features include, for example, surrounding mountains or nearby coast lines creating wind systems like mountain/valley breeze or sea/land breeze (e.g. Yang and Li, 2011).

While the impact of geographical large-scale features on the city ventilation can be substantial, the possibilities for city planners are limited to actively influence ventilation patterns on city scale. On street or neighbourhood scale, however, the ventilation can be strongly influenced by appropriate building arrangement if the effects on ventilation are correctly understood. Precise investigations of ventilation patterns via urban ventilation assessments are therefore a substantial part of modern city planning.

1.2 Urban Ventilation Assessments

Urban ventilation assessments (UVAs) or air ventilation assessments are a measure to investigate the ventilation properties within the vicinity of single buildings, city quarters or even entire city areas. Local governments demand such assessments prior to construction to ensure safe conditions for the city dwellers (e.g. van Aalst et al., 1998; Ng et al., 2005; Ng, 2009; Mills, 2006; VDI, 2008, 2020; Ministerium für Verkehr und Infrastruktur Baden-Württemberg, 2015). Their purpose can be manifold. The main aspects to be considered in a UVA are wind comfort, thermal comfort and air quality.

When focusing on wind comfort, the wind field is analysed for strong-wind conditions that may impose dangerous situations for pedestrians. Strong winds can develop if the mean wind is funnelled into street canyons, or high turbulence levels are created at building edges, causing the wind comfort to be reduced. Due to the complex building layout forming wide open areas and narrow street canyons, wind comfort can be very different within the city area (Blocken and Carmeliet, 2004). The combined effect of multiple buildings then needs to be assessed using a UVA.

The thermal comfort describes the thermal sensation and considers the human energy balance (e.g. Fanger, 1970). It is influenced by the temperature, humidity and radiation distribution within the urban area, but is also influenced by the wind field, and hence, by the ventilation. In the cold season, strong winds can reduce thermal comfort in combination with cold temperatures. A UVA can help to identify unfavourable building layouts and design sheltered areas where a cosy thermal comfort can be guaranteed in cold strong-wind conditions. In connection with global warming, however, UVAs are more focused on high temperatures that induce thermal discomfort as well (e.g. Müller et al., 2014; Cheung and Hart, 2014; Kazak, 2018). During hot summer days, thermal comfort can be reduced by a lack of shading and hence increased solar radiation at the surface within a city. City surfaces tend to absorb more heat compared to the average rural areas. The stored heat is released during night time, resulting in high air temperatures and causing an uncomfortable thermal environment. Good ventilation can ensure the exchange of hot city air with cooler air from rural areas to improve thermal comfort.

Air quality is another important aspect of city ventilation, and hence, regularly focused by UVAs. Urban areas are densely packed with pollutant sources (Fenger, 1999). The resulting air pollution imposes serious health risks on the city dwellers and is accounted for 2 % of world-wide deaths (World Health Organization, 2009). An effective way to mitigate health risks caused by air pollution is to reduce the concentration and the exposure time of the urban population to air pollution (Beelen et al., 2014; Shah et al., 2015). UVAs help to identify the behaviour of pollutant dispersion within the complex urban area. Results can be used to prevent obstructing air passageways or to create new ventilation paths through densely built-up areas.

Different methods are utilized to perform a UVA: field measurements using long-term and temporary measurement stations to investigate the status quo, or wind-tunnel experiments and numerical simulations to study planning scenarios or various meteorological conditions in relatively short time (e.g. Ministerium für Verkehr und Infrastruktur Baden-Württemberg, 2015). Measurements on site, i.e. within the actual city area, capture the exact conditions in the area of interest but they are limited to the status quo and cannot consider any plannings. Further, measurements usually only capture the situation at a limited number of points. Important features relevant to the ventilation might easily be overseen by the sparse measurement locations. Wind-tunnel experiments have the advantage to also consider planned constructions with different variations. Also, data can be monitored at multiple positions with less expenditure within wind-tunnel experiments compared to field measurements. Additionally, two dimensional measurements are available like Particle-Image Velocimetry even

though these are limited to simple building setups where the view of the instruments must not be obstructed by other buildings (Blocken et al., 2016). However, wind-tunnel experiments are limited mostly to dynamically-driven meteorological scenarios. It is generally very complicated to treat a non-neutral stratification or weak-wind scenarios within wind-tunnel experiments (Degrazia et al., 2018; Marucci et al., 2018).

Numerical simulations in form of computational fluid dynamics (CFD) simulations, however, are capable to monitor data at every position within the simulation domain independent of the building structures. CFD simulations are also capable to cover complex meteorological scenarios but increase in computational costs, and hence, in monetary costs the more details are considered.

The most common types of CFD simulations are Reynolds-averaged Navier-Stokes (RANS) simulations, which calculate the mean atmospheric conditions and yield the mean ventilation within the study area. Effects of atmospheric turbulence on the mean conditions are parameterized. This is the to-date mostly used method for CFD simulations due to its computationally cheap costs compared to other, more advanced CFD methods (Blocken et al., 2016). However, the effect of turbulence elements on the mean flow field is strongly influenced by the utilized turbulence parameterization. Flow features like re-circulation zones of bluff bodies or the effect of convection on the building scale are often difficult to simulate and require additional parameterizations and assumptions (Cheng et al., 2003; Defraeye et al., 2010; Hattori et al., 2013).

A more advanced technique are large-eddy simulations (LES) that directly simulate the relevant turbulence elements and parameterize only the small-scale turbulence (e.g. Ferziger, 1996). Considering large-scale turbulence improves simulation results over RANS simulations such as that re-circulation zones and corner flows are better represented. Also, convection can be directly simulated with no need for additional parameterization. This allows for better representation of the interaction between convection and ventilation. However, LES requires a smaller grid spacing and time step compared to RANS simulations which makes an LES computationally more expensive. Hence, urban ventilation assessments utilizing LES are still quite rare.

Depending on the chosen method, the costs to perform a UVA can vary significantly. To keep the costs at a minimum and UVAs achievable for larger areas, the analysed details are often reduced to the most necessary ones that influence the aspects of urban ventilation focused by the UVA. For CFD studies, the grid size directly impacts the computational costs. To limit the costs, grid sizes are chosen to be as coarse as possible to still cover all required details important for the UVA. In turn, the considered building geometry gets distorted and details are getting lost. To distinguish between important and irrelevant building features, their possible impact on the ventilation must be known, which, however, is not always the case. An example for this are openings of courtyard cavities. Their impact on air quality is to date only poorly understood (Hall et al., 1999; Ok et al., 2008).

Another influencing factor, that is regularly reduced in detail, is the impact of atmospheric stability on city ventilation. RANS simulations are not capable to directly simulate thermal up- and down-draughts, developing in unstable atmospheric conditions, due to the lack of resolved turbulence. LES, on the other hand, are still too costly to be considered as a standard method used for UVAs. Therefore, the effect of thermal turbulence on urban ventilation is mostly parameterized or only neutral stratification is considered to estimate the ventilation. However, the details of ventilation behaviour within an unstably stratified atmosphere can vary significantly compared to that under neutral stratification.

These assumptions and reduced coverage of details by UVAs can lead to an over- or under-estimation of the ventilation. Mitigation strategies, based on wrongly identified ventilation patterns, could even worsen the actual ventilation situation increasing health risks for city

dwellers. Therefore, it is important to further improve the understanding of urban ventilation.

1.3 Specific Problems of Urban Ventilation Assessments

For conducting an urban ventilation assessment, various methods can be used as described in Section 1.2. However, none of these methods are capable to consider every aspect of the UBL in high detail. Depending on the chosen method, different assumptions must be made in order to utilize the method. These assumptions can originate from technical limitations (e.g. ignoring thermal stratification in wind tunnels or reducing the level of detail of the building geometry in coarse CFD simulations) or even from a lack of information available (e.g. three-dimensional building structures are not available).

Such simplifications can be done on different scales, e.g. assuming less surface details or assuming an idealized atmospheric setup. Within this thesis, two different assumptions on two different scales are analysed in detail: (a) reduced building features by neglecting courtyard openings and (b) neglecting atmospheric stability when focusing on city ventilation. To analyse these two aspects, the LES model PALM (see Sect. 2.1) is chosen.

Even though LES models present a powerful tool to study the interactions within urban areas, they are a mere imperfect representation of the real world. To understand the capabilities and inaccuracies of a simulation model, a proper evaluation study is essential (Masson, 2006; Oke, 2006; Franke et al., 2007; Blocken, 2015). Therefore, prior to focusing the two above-mentioned aspects, an evaluation study of the applied model PALM is presented in Section 3. This evaluation study aims at the dynamic core of PALM and focuses on the model's capabilities to represent the flow within an urban area, which is the basis of each urban ventilation assessment. The dynamic core of PALM refers to the simulation of the flow dynamics that form the core of the model. The flow dynamics describe the transport of all simulated quantities like momentum, heat, and other scalar quantities. Hence, the dynamic core represents the foundation of the simulation model. Evaluating a CDF model can be achieved by comparing simulation results against real-world measurements and wind-tunnel experiments (e.g. Schatzmann et al., 2010). In Section 3, results from a wind-tunnel experiment conducted at the Environmental Wind Tunnel Laboratory (EWTL) at the University of Hamburg, Germany, are used as reference for the evaluation study. Wind-tunnel data are preferred as reference data compared to real-world measurements because in wind-tunnel experiments, the experimental conditions are well-defined. These conditions can then be used for the CFD simulations. This limits the deviations between simulation and reference data due to uncertainties in the initial and boundary conditions.

1.3.1 Urban Ventilation on Building Scale: Courtyard Ventilation

At building scale, many different aspects alter ventilation. The most influential are the actual building shapes (e.g. Xie et al., 2005; Ng et al., 2011), as determined by numerous wind-tunnel experiments, real-world measurements and CFD simulations (e.g. Blocken and Carmeliet, 2004). This also includes the ventilation of courtyards. However, openings of such courtyards are to date only rarely studied and their effect on the courtyard ventilation is poorly understood. Courtyards are a common feature throughout cities of all sizes around the globe. Thus, a potentially large number of city dwellers might be influenced by poorly ventilated courtyard cavities, especially if the courtyards serve as recreation areas.

Only a few studies investigated the influence of openings on courtyard ventilation. Hall et al. (1999) performed the first wind-tunnel study and compared the ventilation of a closed and an opened courtyard for an isolated building with undisturbed oncoming wind. They
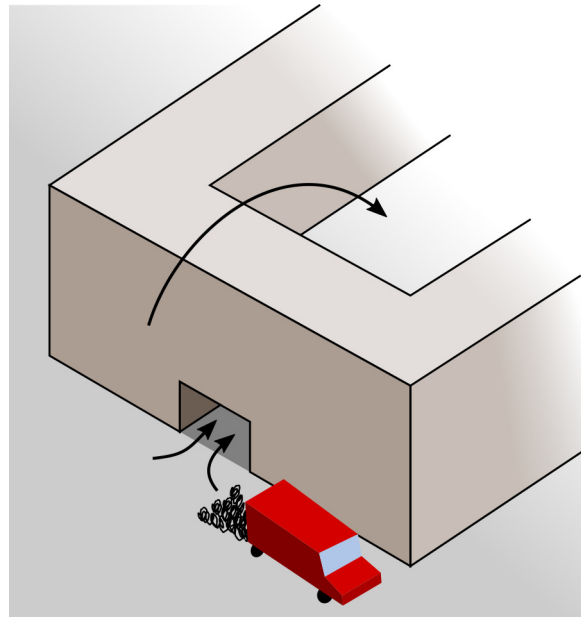
Figure 1.2: Pollutants from traffic exhausts may enter courtyards through the top and lateral openings.

identified that openings can significantly affect courtyard ventilation. The removal of pollutants released within the courtyard cavity changed depending on the orientation of the openings with respect to the mean wind direction. Even though pollutant sources can be situated within courtyards, the more common source of pollution are the surrounding streets. Hence, the more relevant question is how lateral openings affect the transport of pollutants from the streets into the courtyard cavities.

Another study by Ok et al. (2008) showed that the mean wind speed increases within the courtyards if lateral openings are present. The wind speed was found to be highest in the case of multiple openings at the windward side of the courtyard-forming building. Their study, as well as that of Hall et al. (1999), however, focused on single idealised courtyard setups while in reality, courtyards are usually part of an urban building array forming several courtyards and creating a complex flow field around each courtyard.

A more realistic setup was studied by Kurppa et al. (2018) where they focused on pollution distribution within different city-block designs in a part of Helsinki. The pollutant concentration was reported to be lower within courtyards compared to street canyons even if the courtyard cavities were not fully enclosed by buildings. A detailed analysis of the pollutant transport into the courtyards was, however, not part of that study.

The influence of pollution on human health depends, besides other aspects, on the concentration (Kampa and Castanas, 2008). Closed courtyards or backyards are separated by their surrounding buildings from the high pollutant concentrations in the street canyons. The only way these pollutants can get into the courtyard is by entrainment through the roof-level opening. In the same way fresh air from above-roof level can be mixed in, reducing the pollutant concentration in the courtyard (Weber and Weber, 2008; Zauli Sajani et al., 2016). However, lateral openings create a direct connection between street canyons and courtyard cavities allowing pollutants to directly enter courtyards at street level height (see Fig. 1.2). Courtyard openings might therefore act as significant pollutant sources for courtyard cavities. Both, mean and maximum pollution concentration might be critically different between opened and closed courtyards.

From the findings of the above mentioned studies, the following two questions arise:

> What is the effect of lateral openings on courtyard pollution and ventilation within an urban environment?

> How do lateral openings affect maximum concentrations and residence time scales within courtyards?

These two questions are addressed and answered in a detailed investigation of the influence of lateral openings on courtyard ventilation. The respective study is presented in Section 4.

1.3.2 The Influence of Stratification on City Ventilation

On the building scale, individual building geometries and features like courtyard openings influence the local ventilation. When taking a look at the ventilation properties of a neighbourhood or a city quarter, a more general look needs to be taken onto the building configuration. On the neighbourhood scale, building parameters like mean building height or building density are used to identify the ventilation potential of city quarters.

Grimmond and Oke (1999) analysed various different city layouts on their morphological properties trying to formulate a model predicting the general roughness characteristics, and hence, the aerodynamic properties from different city areas. Even though a robust model could not be formulated, they still found a connection between the different building properties like plan area index or frontal area index and surface roughness, and hence, ventilation.

Comparing two idealized building arrays of different building heights, Hang et al. (2011) found a connection between building height and ventilation. The taller buildings caused higher velocities within the street canyons than the shallower building array. They found a stronger blocking effect of the oncoming flow by the taller buildings. The tall buildings forced the air to go through the street canyons, while in the shallow building case, the flow was mainly diverted over the building array.

Chen et al. (2017) investigated the influence of height variation and building density on city ventilation also using idealized building arrays. Higher ventilation was found for building arrays with varying building height compared to a homogeneous building configuration. Also, better ventilation was observed for less densely packed building arrays.

The above mentioned studies focused only on neutral conditions. Under strong-wind conditions, a neutral stratification is a valid assumption as buoyancy effects can be neglected over the mechanically induced turbulence. However, especially weak-wind conditions can impose a major challenge for city ventilation (Ng, 2009). With a weak background wind being present, the air exchange is limited and pollutants as well as heat accumulates within a city posing possibly dangerous health risks to city dwellers. To ensure a safe environment for the population, proper city ventilation must also be guaranteed during weak-wind conditions. Hence, there is a need to study such scenarios.

Under weak-wind conditions, flow patterns change within and above the city (see Fig. 1.3) which also influences the transport of pollutants and heat. Yang and Li (2011) investigated the influence of the stratification on the ventilation in Hong Kong City by means of RANS simulations. They could show an improved ventilation for unstable stratification compared to a neutral stratification and reported that the thermal influence was most significant under weak-wind conditions. Within the study, two different idealized building setups were considered with one having additional secondary streets, i.e. a reduced plan area index. This reduced plan-area-index case showed an improved ventilation. However, the idealized building array consisting of only 21 artificial building blocks and also the parameterized turbulence representation within their RANS simulation allowed only for a general evaluation of the ventilation. A detailed analysis of ventilation patterns within different city areas was not conducted.
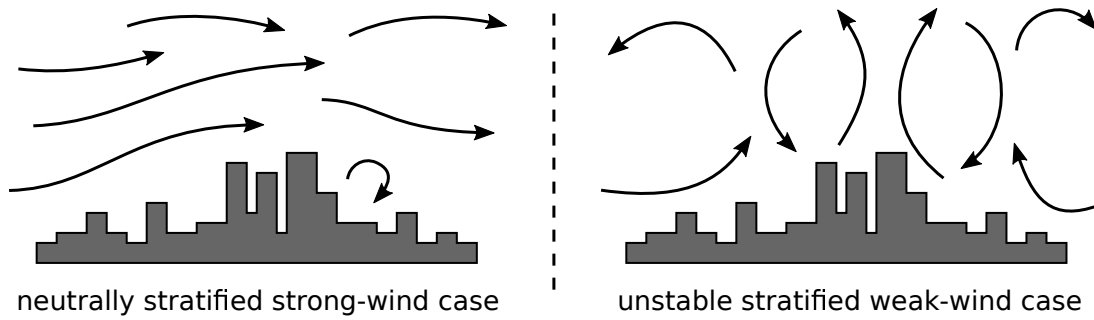
neutrally stratified strong-wind case   unstable stratified weak-wind case

Figure 1.3: Expected flow conditions above a city during a neutrally stratified strong-wind case and an unstably stratified weak-wind case.

A study by Park et al. (2013) utilized LES to compare the ventilation inside an idealized building array under heated and non-heated conditions. They found that the span-wise flow increased in strength for the heated condition also showing an improved ventilation under unstable conditions.

The studies by Yang and Li (2011) and Park et al. (2013) showed that ventilation changes for different stratification. However, a detailed analysis is missing how different building parameters influence the city ventilation under different atmospheric stratification. The questions to be raised, are:

> Does the building height still have the same impact on the ventilation if an unstably stratified weak-wind case is considered instead of a neutrally stratified strong-wind case?

> How does the correlation between plan area index (building density) and ventilation change under different atmospheric stratification?

The knowledge of such relation between building parameters and ventilation can be of high value for city planners in order to make a first estimation of the ventilation of newly planned urban areas. By means of high-resolution turbulence-resolving simulations, these questions are addressed in Section 5.

2 Methods

Observations, wind-tunnel experiments and CFD models are tools to study the urban boundary layer. For this thesis, a CFD model was chosen to tackle the research questions raised in Section 1.3. CFD models allow a detailed analysis of the ventilation and the interaction between ventilation and different aspects of the meteorological situation and the building setup by isolating single effects in an idealised case study.

The RANS technique is unsuitable due to its lack of properly representing turbulence effects on corner flows and re-circulation zones (Cheng et al., 2003). These flow features might have a large impact on the ventilation of courtyards, especially when including small-scale structures like courtyard openings. Also, RANS simulations cannot directly simulate thermally induced up- and down-draughts in a convective boundary layer. Only the mean effect of these thermally induced turbulence features are considered through parameterization (Defraeye et al., 2010; Hattori et al., 2013). Another common simulation approach is the direct numerical simulation (DNS) which resolves the entire turbulence spectrum without the use of any turbulence parameterization (Moin and Mahesh, 1998). However, the computational demands still exceed the current available resources to perform a DNS of atmospheric turbulence where the Reynolds number Re is typically in the order of 10^9 (Yang and Griffin, 2021). As a compromise between the computational demanding DNS and the fully parameterized turbulence used by RANS simulations, the large-eddy simulation (LES) method simulates only the most energy-containing turbulence elements, while small-scale turbulence is parameterized (e.g. Ferziger, 1996). This allows for larger grid sizes, and hence, reduces the required amount of total grid points (and thus computational demands), compared to DNS, while still resolving turbulent flow features like corner flows (Xie and Castro, 2006, 2009) and thermally induced turbulence (e.g. Deardorff, 1972; Schmidt and Schumann, 1989; Moeng and Sullivan, 1994). The LES method currently presents the best trade-off between accuracy and computational costs, and is thus be used in the studies presented in this thesis.

2.1 The PALM Model System

The German city-climate project "Urban Climate Under Change, [UC]^2" aims to develop an LES model which is capable of representing the processes inside the complex urban environments (Scherer et al., 2019). During the [UC]^2 project, the scientific LES model PALM (Raasch and Schröter, 2001; Maronga et al., 2015, 2020) is used as a basis and is further developed to simulate complex urban situations in high detail (Maronga et al., 2019). Even though the development is still ongoing, PALM has already been successfully deployed for research projects studying processes in urban areas and building canopies (e.g. Letzel et al., 2008, 2012; Park et al., 2012, 2015; Hellsten et al., 2015; Lo and Ngan, 2015; Kurppa et al., 2018; Geletič et al., 2021). Therefore, the PALM model is well suited to study urban ventilation and is, hence, used in the studies presented in this thesis.

2.1.1 Governing Equations

PALM has a large number of different features of which many specifically deal with the urban boundary layer (e.g. the building representation, the building-surface model, or the indoor-climate model). However, only a few of these features were actually used in this thesis

in order to isolate specific effects on the urban boundary layer. Hence, the following model description covers only those parts of PALM which are actually used in the following sections of this thesis. A full description of all available features of PALM is given by Maronga et al. (2015, 2020).

PALM is based on the non-hydrostatic, filtered, incompressible, Bousinesq-approximated Navier-Stokes equations. The momentum equations read as:

$$\frac{\partial \overline{u_i}}{\partial t} = -\frac{\partial \overline{u_i}\,\overline{u_j}}{\partial x_j} - \varepsilon_{ijk}f_j\overline{u_k} + \varepsilon_{i3j}f_3 u_{g,j} - \frac{1}{\rho_0}\frac{\partial \overline{p^*}}{\partial x_i} + g\frac{\overline{\theta} - \langle\overline{\theta}\rangle}{\langle\overline{\theta}\rangle}\delta_{i3} - \frac{\partial}{\partial x_j}\left(\overline{u_i''u_j''}\right). \quad (2.1)$$

The equations for mass conservation and energy conservation are

$$\frac{\partial \overline{u_i}}{\partial x_i} = 0, \quad (2.2)$$

$$\frac{\partial \overline{\theta}}{\partial t} = -\frac{\partial \overline{u_j}\overline{\theta}}{\partial x_j} - \frac{\partial}{\partial x_j}\left(\overline{u_j''\theta''}\right) + Q_\theta, \quad (2.3)$$

with $i, j, k \in \{1, 2, 3\}$. The velocity components are denoted by u_i with $u_1 = u$, $u_2 = v$ and $u_3 = w$ and the direction by x_i with $x_1 = x$, $x_2 = y$ and $x_3 = z$; t represents the time, ε the Levi-Civita symbol and δ the Kronecker delta. The Coriolis parameter is defined as $f = (0, 2\Omega\cos(\phi), 2\Omega\sin(\phi))$ with $\Omega = 0.729 \times 10^{-4}\,\text{rad s}^{-1}$ being the angular velocity of Earth and ϕ being the geographical latitude. The geostrophic wind is denoted by u_g, ρ_0 describes the density of dry air, p^* is the perturbation pressure, and g is the gravitational acceleration. Finally, θ denotes the potential temperature, and Q_θ additional source or redistribution terms. A horizontal average over the entire model domain is marked as $\langle\cdot\rangle$ while the overline and double prime mark filtered and sub-grid scale (SGS) quantities, respectively. Additionally, a passive scalar can be simulated via

$$\frac{\partial \overline{s}}{\partial t} = -\frac{\partial \overline{u_j}\,\overline{s}}{\partial x_j} - \frac{\partial}{\partial x_j}\left(\overline{u_j''s''}\right) + Q_s, \quad (2.4)$$

where s denotes the scalar concentration, and Q_s is a source term. For readability, the overline is omitted for all quantities, except for the turbulent fluxes, in the following.

The above mentioned equations describe a dry situation. Humidity effects were neglected in all studies presented in this thesis. The full set of equations including humidity effects are described by Maronga et al. (2015).

The Equations 2.1 – 2.4 do not represent a closed set of equations. The turbulent fluxes $\overline{u_j''\phi''}$ with $\phi \in \{u_i, \theta, s\}$ are unknowns. Hence, additional formulations are required to close set of equations.

2.1.2 Turbulence Closure

In order to solve the Equations 2.1, 2.3, and 2.4, the turbulent fluxes $\overline{u_j''\phi''}$ with $\phi \in \{u_i, \theta, s\}$ need to be parameterized. For this so-called turbulence closure, a 1.5-order closure based on the method presented by Deardorff (1980), with modifications made by Moeng and Wyngaard (1988) and Saiki et al. (2000), is used in PALM. Local gradients of the resolved (filtered)

quantities approximate the turbulent fluxes:

$$\overline{u_i'' u_j''} - \frac{2}{3} e \delta_{ij} = -K_{\mathrm{m}} \left(\frac{\partial u_i}{\partial x_j} + \frac{\partial u_j}{\partial x_i} \right), \tag{2.5}$$

$$\overline{u_i'' \theta''} = -K_{\mathrm{h}} \frac{\partial \theta}{\partial x_i}, \tag{2.6}$$

$$\overline{u_i'' s''} = -K_{\mathrm{h}} \frac{\partial s}{\partial x_i}, \tag{2.7}$$

where K_{m} and K_{h} denote the SGS eddy diffusivities of momentum and heat, respectively, and $e = \frac{1}{2} \overline{u_i'' u_i''}$ denotes the SGS turbulent kinetic energy (TKE).

The parameterized turbulent momentum flux, defined in Equation 2.5, is reduced by $-\frac{2}{3} e$. The subtracted term is added to the perturbation pressure forming the modified perturbation pressure

$$\pi^* = p^* + \frac{2}{3} \rho_0 e. \tag{2.8}$$

This leads to the modified version of the momentum equations:

$$\frac{\partial u_i}{\partial t} = -\frac{\partial u_i u_j}{\partial x_j} - \varepsilon_{ijk} f_j u_k + \varepsilon_{i3j} f_3 u_{g,j} - \frac{1}{\rho_0} \frac{\partial \pi^*}{\partial x_i} + g \frac{\theta - \langle \theta \rangle}{\langle \theta \rangle} \delta_{i3} + \frac{\partial}{\partial x_j} \left(K_{\mathrm{m}} \left(\frac{\partial u_i}{\partial x_j} + \frac{\partial u_j}{\partial x_i} \right) \right). \tag{2.9}$$

The eddy diffusivities are calculated using the SGS-TKE:

$$K_{\mathrm{m}} = c_{\mathrm{m}} l \sqrt{e}, \tag{2.10}$$

$$K_{\mathrm{h}} = \left(1 + \frac{2l}{\Delta} K_{\mathrm{m}} \right), \tag{2.11}$$

with $c_{\mathrm{m}} = 0.1$ according to Lilly (1967) and Deardorff (1980), $\Delta = \sqrt[3]{\Delta x \Delta y \Delta z}$ with Δx, Δy and Δz being the grid sizes along each direction, and l being the SGS mixing length defined as

$$l = \begin{cases} \min \left(1.8z, \Delta, 0.76 \sqrt{e} \left(\frac{g}{\langle \theta \rangle} \frac{\partial \theta}{\partial z} \right)^{-\frac{1}{2}} \right) & \text{for } \frac{\partial \theta}{\partial z} > 0, \\ \min(1.8z, \Delta) & \text{for } \frac{\partial \theta}{\partial z} \leq 0. \end{cases} \tag{2.12}$$

Finally, e needs to be calculated. To acquire an equation for e, first, the equation of the total kinetic energy E is derived from the non-filtered Navier-Stokes equations multiplied by u_i:

$$\frac{\partial E}{\partial t} = -\frac{\partial u_j E}{\partial x_j} - \frac{1}{\rho_0} \frac{\partial u_i p^*}{\partial x_i} + u_i g \frac{\theta - \langle \theta \rangle}{\langle \theta \rangle} \delta_{i3} - \epsilon_{\mathrm{total}}, \tag{2.13}$$

where $\epsilon_{\mathrm{total}}$ describes the dissipation rate of kinetic energy. Subtracting the filtered part of Equation 2.13 from Equation 2.13 yields the prognostic SGS-TKE equation:

$$\frac{\partial e}{\partial t} = -\frac{\partial u_j e}{\partial x_j} - \left(\overline{u_i'' u_j''} \right) \frac{\partial u_i}{\partial x_j} + \frac{g}{\langle \theta \rangle} \left(\overline{u_3'' \theta''} \right) - \frac{\partial}{\partial x_j} \overline{u_j'' \left(e'' + \frac{p''}{\rho_0} \right)} - \epsilon, \tag{2.14}$$

where the SGS flux of e and pressure are parameterized as

$$\overline{u'' \left(e'' + \frac{p''}{\rho_0} \right)} = -2 K_{\mathrm{m}} \frac{\partial e}{\partial x_j}, \tag{2.15}$$

and the SGS dissipation rate is defined as

$$\epsilon = \left(0.19 + 0.74\frac{l}{\Delta}\right)\frac{e^{\frac{3}{2}}}{l}. \tag{2.16}$$

2.1.3 Discretization

The equations are solved using finite differences on a rectilinear staggered Arakawa-C grid (Harlow and Welch, 1965; Arakawa and Lamb, 1977). The grid spacing in vertical direction (Δz) can vary with height while Δx and Δy are constant. Scalar quantities like θ and s are defined at the centre of a grid volume, while horizontal velocity components are shifted by minus half a grid spacing along their respective direction, and the vertical velocity component is shifted by half a grid spacing upwards. For discretization, an upwind-biased fifth-order differencing scheme is used for the advection terms (Wicker and Skamarock, 2002) in combination with a third order Runge-Kutta time-stepping scheme according to Williamson (1980).

The time step Δt has to be chosen in a way that the numerical solution stays stable. Hence, two stability criteria have to be met: the Courant-Friedrichs-Lewi (CFL) criterion according to Courant et al. (1928):

$$\Delta t_{\mathrm{CFL}} \leq \min\left(\frac{\Delta x}{u(x,y,z)}, \frac{\Delta y}{v(x,y,z)}, \frac{\Delta z(z)}{w(x,y,z)}\right), \tag{2.17}$$

and the diffusion criterion according to Roache (1972):

$$\Delta t_{\mathrm{diff}} \leq 0.125 \min\left(\frac{\min(\Delta x^2, \Delta y^2, \Delta z^2(z))}{\max(K_{\mathrm{m}}(x,y,z), K_{\mathrm{h}}(x,y,z))}\right). \tag{2.18}$$

Both, Δt_{CFL} and Δt_{diff}, are first calculated at every grid point. The minimum value over all grid points is then used as the time step for the prognostic equations:

$$\Delta t = c_{\Delta t} \min(\Delta t_{\mathrm{CFL}}, \Delta t_{\mathrm{diff}}), \tag{2.19}$$

where $c_{\Delta t} = 0.9$ is a security factor.

2.1.4 Pressure Solver

According to the Boussinesq approximation, the flow is incompressible, and hence, must be divergence-free, i.e., Equation 2.2 must be fulfilled. Solving Equation 2.9, however, does not automatically ensure that the computed velocity field is free of divergence. To remove the divergence of the flow, a predictor-corrector method (e.g., Patrinos and Kistler, 1977) is used where the perturbation pressure is calculated after each time step. First, Equation 2.9 is solved ignoring the pressure term. This results in a predicted velocity $u_{i,pre}^{t+\Delta t}$ at time $t + \Delta t$. This predicted preliminary velocity is used to calculate the predicted final velocity:

$$u_i^{t+\Delta t} = u_{i,pre}^{t+\Delta t} - \Delta t \frac{1}{\rho_0}\frac{\partial \pi^{*t}}{\partial x_i}. \tag{2.20}$$

Combining Equation 2.2 and 2.20 yields the Poisson equation for π^*:

$$\frac{\partial^2 \pi^{*t}}{\partial x_i^2} = \frac{\rho_0}{\Delta t}\frac{\partial u_{i,pre}^{t+\Delta t}}{\partial x_i}. \tag{2.21}$$

Solving Equation 2.21 gives the modified perturbation pressure π^{*t} that is then used in

Equation 2.20 to derive the divergence-free solution for the flow field.

When using the Runge-Kutta time-stepping scheme, several sub-time steps are calculated (Williamson, 1980). For each of these sub-time steps, Equation 2.21 is solved and the resulting π^* is calculated from a weighted average over all sub steps.

In the presented studies of this thesis, two different methods are used to solve Equation 2.21, depending on the boundary conditions. For cyclic lateral boundary conditions (see details in Sect. 2.1.5), a fast Fourier transform (FFT) can be utilized where Equation 2.21 is Fourier transformed along both horizontal directions and the resulting tri-diagonal matrix is solved along the z-direction (see, e.g., Schumann and Sweet, 1988). To compute the FFT, the FFTW library (Frigo and Johnson, 1998) is used. Due to the technical realization of the implementation of the FFT method (Raasch and Schröter, 2001), only cyclic boundary conditions are possible when applying the FFT method.

Alternatively, Equation 2.21 can be solved using the multi-grid scheme. The multi-grid scheme uses an iterative successive over-relaxation method to solve the Poisson equation on different grid levels (i.e. coarser versions of the domain grid of the simulation, e.g. Hackbusch, 1985). In contrast to the implementation of the FFT method, the technical realization of the multi-grid method also allows to apply non-cyclic lateral boundaries. Hence, this method is used for all non-cyclic simulations of this thesis.

2.1.5 Boundary Conditions

A model has several boundaries: physical boundaries at the ground and at each obstacle surface, and non-physical boundaries in lateral and top direction, because of the limited size of the model domain. At these boundaries, specific boundary conditions must be considered for each prognostic variable. PALM offers several different boundary condition depending on the type of the boundary and the variable. The conditions used in this thesis are discussed in the following.

Bottom Boundary Conditions

At the bottom of the simulation domain, a solid surface is considered. This implies a Dirichlet condition for the wind velocity components with $u(z=0) = v(z=0) = w(z=0) = 0$. For the perturbation pressure, a Neumann condition with $\pi^*(z=0) = \pi^*(z=\Delta z)$ is used in order to maintain $w(z=0) = 0$ after applying the pressure solver. A similar Neumann condition is also used for the scalar quantities e, θ and s. For θ and s, a vertical flux is prescribed at the bottom boundary to represent solar heating (in case of θ, see Sect. 5) and the release of pollutants by traffic (in case of s, see Sect. 4).

Simply applying Dirichlet or Neumann conditions, however, does not fully resolve the physical interactions between the solid surface and the atmosphere that can be observed in reality. Effects like surface friction and heat transfer between the surface and the atmosphere needs to be considered. Because the momentum and heat transfer between surface and atmosphere happens on the sub-grid scale, these transfers cannot be explicitly resolved. To parameterize these transfers, a constant flux layer is assumed between the surface and the first atmospheric grid level. This assumption follows the Monin-Obukhov similarity theory (MOST). Using MOST, the vertical fluxes of momentum and heat at the first grid level above the surface, $\overline{w''u''}_0$, $\overline{w''v''}_0$, and $\overline{w''\theta''}_0$, are calculated based on prescribed roughness lengths for momentum, z_0, and heat, $z_{0,\mathrm{h}}$. These fluxes are utilized in Equations 2.1 and 2.3 and replace the respective fluxes of the turbulence closure at this grid level.

According to MOST, the vertical profile of the horizontal wind velocity, $u_{\mathrm{h}} = \sqrt{u^2 + v^2}$,

and potential temperature are

$$\frac{\partial u_\mathrm{h}}{\partial z} = \frac{u_*}{\kappa z}\Phi_\mathrm{m}\left(\frac{z}{L}\right), \tag{2.22}$$

$$\frac{\partial \theta}{\partial z} = \frac{\theta_*}{\kappa z}\Phi_\mathrm{h}\left(\frac{z}{L}\right), \tag{2.23}$$

with L being the Obukhov length and u_* and θ_* being the friction velocity and the scaling parameter for potential temperature, respectively. They are defined as

$$u_* = \sqrt[4]{\left(\overline{u''w''}_0\right)^2 + \left(\overline{v''w''}_0\right)^2}, \tag{2.24}$$

$$\theta_* = -\frac{\overline{w''\theta''}_0}{u_*}. \tag{2.25}$$

The similarity functions for momentum, Φ_m, and heat, Φ_h, are implemented according to the Businger-Dyer formulation (e.g. Panofsky and Dutton, 1984):

$$\Phi_\mathrm{m} = \begin{cases} 1 + 5\dfrac{z}{L} & \text{for } \dfrac{z}{L} \geq 0, \\ (1 - 16\dfrac{z}{L})^{-\frac{1}{4}} & \text{for } \dfrac{z}{L} < 0, \end{cases} \tag{2.26}$$

$$\Phi_\mathrm{h} = \begin{cases} 1 + 5\dfrac{z}{L} & \text{for } \dfrac{z}{L} \geq 0, \\ (1 - 16\dfrac{z}{L})^{-\frac{1}{2}} & \text{for } \dfrac{z}{L} < 0. \end{cases} \tag{2.27}$$

For a neutral case, as considered in Section 3 and 4, $\frac{z}{L}$ approaches 0, and hence, Φ_m and Φ_h approach 1. The friction velocity, u_*, is calculated by integrating Equation 2.22 along z between z_0 and $z_\mathrm{mo} = 0.5\Delta z$, which is the first atmospheric grid level above the surface:

$$u_* = \frac{\kappa u_\mathrm{h}}{\ln\left(\frac{z_\mathrm{mo}}{z_0}\right)\Phi_\mathrm{m}}. \tag{2.28}$$

Equation 2.22 can be transformed by using Equation 2.24 into

$$\frac{\partial u}{\partial z} = \frac{-\overline{u''w''}_0}{u_*\kappa z}\Phi_\mathrm{m} \text{ and } \frac{\partial v}{\partial z} = \frac{-\overline{v''w''}_0}{u_*\kappa z}\Phi_\mathrm{m}. \tag{2.29}$$

The momentum fluxes are then derived by vertically integrating Equation 2.29 between z_0 and z_mo.

In case of non-neutral conditions, as considered in Section 5, L is defined as

$$L = \frac{\theta u_*^2}{\kappa g \theta_*}. \tag{2.30}$$

For the study presented in Section 5, the surface heat flux is prescribed as a constant value of $\overline{w''\theta''}_0 = 0.165\,\mathrm{K\,m\,s^{-1}}$. Together with u_* and θ_* from the previous time step, L can be calculated, and thus, the new u_* and θ_*.

The above mentioned method is used to calculate the surface fluxes at horizontal surfaces. At vertically oriented surfaces, momentum fluxes are also calculated using MOST, but assuming a neutral stratification.

The described bottom boundary condition is in accordance to the MOST method shown by Maronga et al. (2015). The method to determine L, presented by Maronga et al. (2020), was not used in the simulations shown in Section 5.
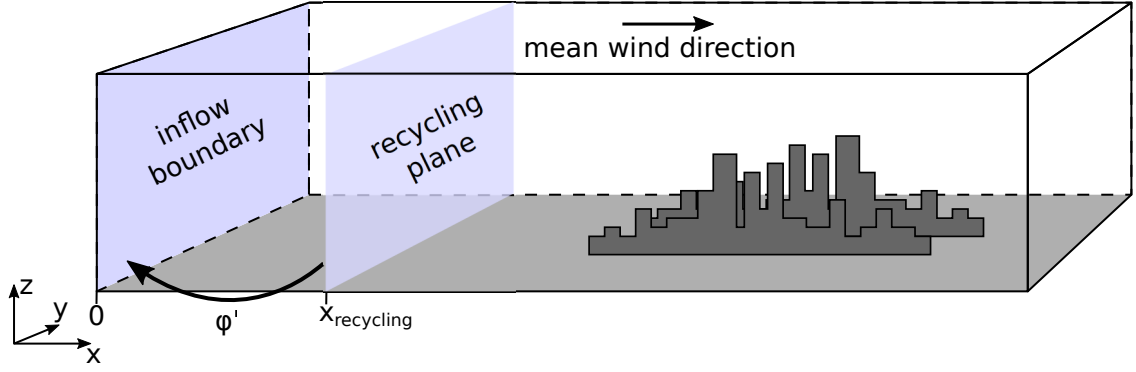
Figure 2.1: Concept of the turbulence recycling method used as inflow-boundary condition. After Maronga et al. (2015).

Top Boundary Conditions

For the horizontal wind speed components, either a Dirichlet condition,

$$u(z_{\text{top}}) = const \text{ and } v(z_{\text{top}}) = const, \tag{2.31}$$

or a Neumann condition,

$$u(z_{\text{top}}) = u(z_{\text{top}} - \Delta z) \text{ and } v(z_{\text{top}}) = v(z_{\text{top}} - \Delta z), \tag{2.32}$$

is used at the top boundary, i.e. at $z = z_{\text{top}}$. For the vertical wind speed, $w(z_{\text{top}}) = 0$ was set for all studies. The perturbation pressure is set to $\pi^*(z_{\text{top}}) = 0$, as well. For the SGS TKE and the scalar concentration, a Neumann condition with

$$e(z_{\text{top}}) = e(z_{\text{top}} - \Delta z) \text{ and } s(z_{\text{top}}) = s(z_{\text{top}} - \Delta z), \tag{2.33}$$

respectively, is utilized, while a Dirichlet condition is applied for θ.

Lateral Boundary Conditions

PALM offers different options for the lateral boundary conditions. The simplest of which is a cyclic boundary condition, where values of the prognostic quantities are mirrored at opposing boundaries. Flow features exiting on one side are immediately entering on the opposing side of the model domain. This method can be applied in both horizontal directions.

When applying cyclic boundary conditions along the mean wind direction, elongated coherent flow features may develop, that are persistent in space and time. These streak-like flow features form naturally and can reach lengths of several kilometres in nature. Due to the limited size of the simulation domain in combination with the cyclic boundary condition, the head of a streak can be cycled into its own tail forming an infinitely long and self-containing streak (Munters et al., 2016). This results in unnaturally stable flow features. To force these structures to break up and dissipate, a shifting method according to Munters et al. (2016) is used. Instead of directly mirroring opposite boundaries, the copied values are shifted by a distance y_{shift} parallel to the boundary before being applied to the opposing boundary. In order for the shifting to work, cyclic boundaries must also be set in y-direction. The shifting method is used in Section 3 and 4.

Cyclic lateral boundary conditions have the disadvantage that the influence of any obstacles within the simulation domain on the flow field are not able to leave the domain. If the simulation domain does not offer enough space in stream-wise direction for the effects of the

obstacles to decay before arriving at the domain border, these effects are cycled through the domain and enter the domain at the windward boundary. This changes the approaching flow and alters the simulation results. To avoid this effect, one method is to enlarge the simulation domain along the stream-wise direction to offer enough space that all effects of the obstacles decay before re-entering the domain. This, however, can increase the computational costs significantly. Another option is to use non-cyclic boundary conditions in stream-wise direction allowing the influence of the obstacles on the flow field to leave the simulation domain. In this case, a smaller simulation domain can be used reducing the computational demand. In Section 5, such non-cyclic boundary conditions are used in stream-wise direction, i.e. along the x-direction.

Non-cyclic boundary conditions impose, however, a challenge at the inflow boundary. At the inflow boundary, no turbulence information is available. Hence, without additional information, a laminar flow is set by the prescribed initial wind profile. Turbulence is then slowly generated inside the domain, for example due to friction at the surface. This would again require a large simulation domain until the approaching flow has developed a sufficient turbulent state. Therefore, an inflow-boundary condition offering additional turbulence information is required. In Section 5, a turbulence recycling method based on the works of Lund et al. (1998) and Kataoka and Mizuno (2002) is used. The turbulent signal of u_i, e, and θ are captured from a so-called recycling plane at $x_{\text{recycling}}$ and added to the fixed inflow profiles at the inflow boundary (at $x = 0$, see Fig. 2.1). At $x = x_{\text{recycling}}$, the turbulent signals are calculated as

$$\varphi' = \varphi - \langle \varphi \rangle_y \quad \text{with} \quad \varphi \in u, v, w, e, \theta, \tag{2.34}$$

where $\langle \cdot \rangle_y$ denotes an average along y-direction. This recycling of turbulent information transforms the laminar inflow into a turbulent inflow and reduces the required domain size. The boundary values are updated at each time step.

PALM's standard outflow-boundary condition for non-cyclic boundaries is a radiation-boundary condition as described by Orlanski (1976):

$$\frac{\partial u_i}{\partial t} + U_{u_i} \frac{\partial u_i}{\partial x} = 0. \tag{2.35}$$

This boundary condition allows turbulence to leave the simulation domain without being reflected back into the domain influencing the simulation results. The transport velocity, U_{u_i}, is calculated as

$$U_{u_i} = \left\langle -\frac{\partial u_i}{\partial t} \left(\frac{\partial u_i}{\partial x} \right)^{-1} \right\rangle_y \tag{2.36}$$

at interior grid points next to the outflow boundary. Further, $U_{u_i} \in [0, \Delta/\Delta t]$, which means, that if the calculated value of U_{u_i} exceeds one of its thresholds, the threshold value is used instead. To use this boundary condition, the flow must always be directed towards the outflow boundary.

In a strong-wind scenario, the outflow boundary is only influenced by the upwind area. Hence, no information is required from the downwind direction and the boundary values can be computed solely depending on the upwind values, as it is done by the radiation-boundary condition. However, in a convective weak-wind scenario, the stronger variation in wind direction causes information to be advected into the domain also at the outflow boundary. Because no information from outside the domain is available, this advection is suppressed by the radiation-boundary condition by setting $U_{u_i} = 0$ in that case. In a convective weak-wind scenario, this lead to strong numerical instabilities during test simulations for the study presented in Section 5. To overcome this limitation, a new boundary condition
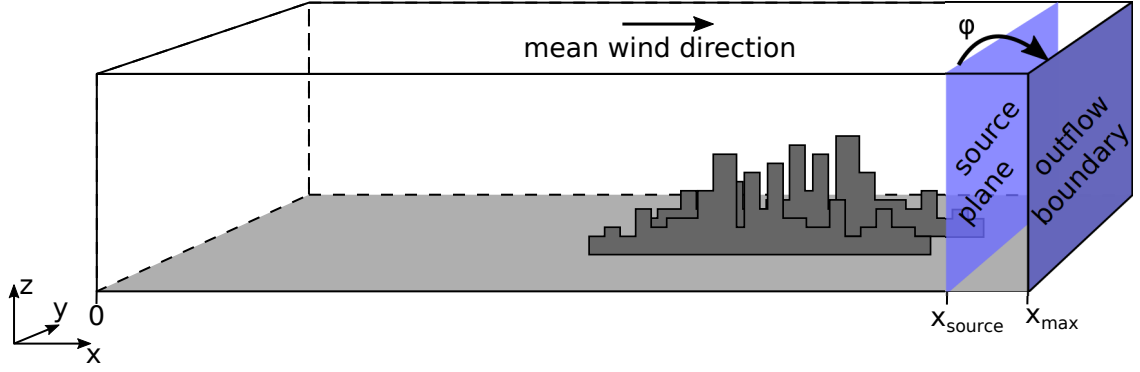
Figure 2.2: Concept of the turbulent outflow method used as outflow boundary condition.

was developed, that provides physically realistic information of the wind and temperature distribution beyond the outflow boundary. Instead of transporting the prognostic quantities $\varphi \in u_i, \theta, e$ from the adjacent grid layer to the outflow boundary, values at a source plane x_{source} are copied to the boundary at x_{max} (see Fig. 2.2). This allows that physically realistic information can enter the domain at the outflow boundary. It has to be noted, however, that this boundary condition is only a technical solution and is not based on a physical concept. If $x_{\mathrm{source}} = x_{\mathrm{max}} - \Delta x$, this outflow condition equals the radiation-boundary condition with $U_{u_i} = \Delta/\Delta t$.

In order for the new outflow condition to avoid the generation of strong numerical instabilities, that were observed when using the radiation-boundary condition in a convective weak-wind case, x_{source} needs to be placed at a certain distance to the outflow boundary. In Section 5, a buffer zone of 500 m between the source plane and the outflow boundary was used which prove to be sufficient. It should also be checked that the general flow situation at the source plane matches those at the outflow boundary. Flow features created by obstacles like corner flows or re-circulation zones should not be present at the source plane. Otherwise, these effects of the obstacles would also appear at the outflow boundary creating unwanted flow features. Therefore, another 500 m-wide buffer zone between the topography features and x_{source} was considered in Section 5.

2.1.6 Initialization

For this thesis, different initial conditions were used for the simulations. The default initial condition is to prescribe vertical profiles for the horizontal wind components and potential temperature, that are used to homogeneously initialize the three-dimensional arrays. To initiate turbulence, uncorrelated Gaussian-distributed random perturbations are imposed to the horizontal velocity fields at the beginning of the simulation until the resolved-scale TKE exceeds a given threshold.

Depending on the meteorological and surface conditions, a certain simulation time is required until the turbulence is fully developed. To reduce this so-called spin-up time, and hence, the computational costs, the cyclic-fill method is applied for the initialization. A simulation with an identical meteorological setup as the main simulation, but with a reduced horizontal domain size and cyclic boundary conditions, is computed until the turbulence is fully developed. At the end of this precursor simulation, the instantaneous three-dimensional arrays of the prognostic quantities are saved. These arrays are used to initialize the domain of the main simulation. Because of the cyclic boundary conditions used in the precursor simulation, the arrays can be seamlessly stringed together repeatedly until the larger domain of the main simulation is completely filled. This presents already fully developed turbulence at

the simulation start, which then reduces the required spin-up time for the main simulation.

2.1.7 Rayleigh Damping

In the simulation of the convective boundary layer, shown in Section 5, gravity waves are triggered by the convection at the top of the boundary layer. To prevent the reflection of these gravity waves at the domain top, a Rayleigh damping is employed within the upper part of the simulation domain. The damping is achieved by adding an additional term to Equation 2.9 and 2.3:

$$-R_{\text{damping}} \cdot (\phi - \phi_{\text{ref}}), \quad \text{with} \quad \phi \in \{u, v, w, \theta\}. \tag{2.37}$$

The reference ϕ_{ref}, used for damping, is defined by the initial profile of the respective variable. The damping coefficient is defined as

$$R_{\text{damping}} = \begin{cases} 0 & \text{for } z < z_{\text{damping}}, \\ 0.01 \sin^2 \left(\dfrac{\pi}{2} \dfrac{z - z_{\text{damping}}}{z_{\text{top}} - z_{\text{damping}}} \right) & \text{for } z \geq z_{\text{damping}}, \end{cases} \tag{2.38}$$

where $z_{\text{damping}} = 1.2\,\text{km}$ describes the height above which the damping takes place.

2.1.8 Large-Scale Subsidence

In Section 5, a large-scale subsidence is considered in order to get a constant boundary-layer height over time while also having a positive heat flux at the surface. The subsidence is realized by adding another tendency term to Equation 2.3:

$$Q_\theta = -w_s \frac{\partial \theta}{\partial z}, \tag{2.39}$$

where w_s is a height-dependent prescribed subsidence velocity.

When applying the large-scale subsidence, the top boundary condition of θ needs to be adjusted to account for the increasing temperature:

$$\theta(z_{\text{top}}, t + \Delta t) = \theta(z_{\text{top}}, t) - \Delta t \cdot w_s(z_{\text{top}}) \frac{\theta(z_{\text{top}}, t = 0) - \theta(z_{\text{top}} - \Delta z, t = 0)}{\Delta z}. \tag{2.40}$$

If also Rayleigh damping is applied (see Sect. 2.1.7), the reference state of θ used by the Rayleigh damping, i.e. the initial profile, is adjusted in the same manner as the top boundary condition.

2.1.9 Building Implementation

PALM uses the mask method (Briscolini and Santangelo, 1989) to represent buildings and topography. A grid volume is set to be either fluid or solid, i.e. either belongs to the atmosphere or to an obstacle. Obstacle walls are defined by setting the wall-normal velocity to zero at the obstacle walls. Velocities inside the obstacle are set to zero as well. In combination with PALM's rectilinear grid structure, this results in a step-wise representation of the topography. MOST is considered at atmospheric grid points adjacent to obstacles (see Sect. 2.1.5).

2.1.10 Lagrangian Particle Model

PALM comes with an embedded Lagrangian particle model (LPM). The LPM is used in Section 4 to study the residence times of pollutants within a courtyard cavity. The LPM simulates the paths of individual particles released inside the model domain. These paths can be tracked and used in post-processing to, e.g., analyse residence times of particles inside specific domain areas as done in Section 4.

The equations describing the particle's position $x_{\mathrm{p},i}$ read as:

$$\frac{\mathrm{d}x_{\mathrm{p},i}}{\mathrm{d}t} = u_{\mathrm{p},i}(t) \ \ \text{with} \ \ i \in \{1,2,3\}, \tag{2.41}$$

where $u_{\mathrm{p},i}(t)$ are the velocity components of a particle in the respective direction. In this thesis, particles are considered as passive without any mass or temperature, i.e. they are affected exclusively by the wind field.

The particle velocity $u_{\mathrm{p},i}$ can be split into a resolved-scale and an SGS part according to Lamb (1978). The resolved-scale part is determined by interpolating the LES velocities onto the particle's position. The SGS part of the velocity is calculated by integrating a stochastic differential equation based on the model of Thomson (1987) with modifications by Weil et al. (2004). Isotropic and Gaussian-distributed turbulence is assumed and the stochastic particle dispersion is parameterized using the SGS-TKE and dissipation rate provided by the LES. A detailed description of the LPM is given in Maronga et al. (2015) with the newest changes described in Maronga et al. (2020).

2.2 Evaluation Methods for Urban Ventilation Analyses

Urban ventilation can be evaluated on different levels with different approaches depending on the focus of a study. As different aspects of the urban ventilation are studied in Section 4 and 5, also different methods are utilized. The study presented in Section 4 focuses on air pollution, and hence, uses scalar concentration and the residence time of pollutants to investigate the ventilation of single courtyard cavities. Section 5 takes a more general look on the urban ventilation within a large built-up urban area. The aim here is to study the overall ventilation and the blockage of the air flow through city quarters. In this case, the velocity ratio is a suitable measure for the urban ventilation.

It has to be noted, that many other parameters can be used to evaluate urban ventilation like the age of air (e.g. Hang et al., 2009), the net escape velocity or the purging flow rate (e.g. Hang et al., 2015). These methods, however, were not utilized in this thesis.

2.2.1 Scalar Concentration Analysis

Analysing scalar concentration and its transport can give a deep insight on the ventilation behaviour of enclosed cavities. In Section 4, the influence of lateral openings on courtyard ventilation and air quality is investigated. A passive scalar is released outside of the courtyards within the surrounding streets to simulate pollutants emitted by traffic. An analysis of the mean concentration s of the passive scalar within the courtyard cavities can then be used as a measurement of how much pollution is transported into the courtyards. Additionally, time series of the scalar concentration at the centre of the courtyard cavities are measured to allow an analysis of peak values. Besides the average concentration, the peak values are important if focusing on health risks.

To further understand the transport of pollutants into the courtyard cavities, the fluxes through the lateral and top openings are monitored. Analysing the fluxes through the openings allows to conclude if pollutants are entrained or detrained through the additional lateral

openings. Insights to the entrainment/detrainment behaviour can be utilized for the positioning of openings during the planning phase of the construction.

Taking Equation 2.4, the transport terms can be split into lateral and vertical transport:

$$\frac{\partial s}{\partial t} = \underbrace{-\frac{\partial us}{\partial x} - \frac{\partial vs}{\partial y} - \frac{\partial \overline{u''s''}}{\partial x} - \frac{\partial \overline{v''s''}}{\partial y}}_{\text{lateral transport}} \underbrace{-\frac{\partial ws}{\partial z} - \frac{\partial \overline{w''s''}}{\partial z}}_{\text{vertical transport}} + Q_s. \tag{2.42}$$

Inside the courtyards, no source is present, hence, $Q_s = 0$. Averaging Equation 2.42 over time and integrating it over the entire courtyard cavity, V, leads to

$$\int_V \frac{\widetilde{\partial s}}{\partial t} \partial V = \underbrace{\int_V \left(-\frac{\widetilde{\partial us}}{\partial x} - \frac{\widetilde{\partial vs}}{\partial y} - \frac{\widetilde{\partial \overline{u''s''}}}{\partial x} - \frac{\widetilde{\partial \overline{v''s''}}}{\partial y} \right) \partial V}_{=:T_l} + \underbrace{\int_V \left(-\frac{\widetilde{\partial ws}}{\partial z} - \frac{\widetilde{\partial \overline{w''s''}}}{\partial z} \right) \partial V}_{=:T_v},$$
$$\tag{2.43}$$

where $\widetilde{\cdot}$ denotes a time average. The left-hand side describes the mean temporal accumulation of s within V. Compared to the terms on the right-hand side, the accumulation is only small due to the constant ventilation of the courtyard cavities. The lateral net transport of pollutants, i.e. through the lateral opening, is described by T_l, while the vertical net transport through the top of the courtyard is described by T_v. Positive values indicate an increase of pollutant concentration, negative values indicate a decrease of concentration through the corresponding opening (lateral or top).

2.2.2 Residence Time

The residence time is another measure to describe the ventilation of an urban area. It is defined as the time an air parcel resides within a certain volume, i.e. the time between its first entering and first leaving of the volume. The mean residence time, which can be obtained from simulating a passive scalar (Eulerian approach), can be taken as a measure of how effectively air is ventilated through a certain volume (Etheridge and Sandberg, 1996; Kato et al., 2003; Bady et al., 2008). A more detailed analysis of residence time, however, requires tracking of single particles (Lagrangian approach) through the analysis volume (Lo and Ngan, 2017). The advantage of the Lagrangian approach is that the time-integrated effect of pollutants can be analysed in much higher detail which gives a better insight of the ventilation within the analysis volume.

In Section 4, the residence time of pollutants is investigated by simulating single particles within courtyard cavities utilizing PALM's LPM. The method is based on Lo and Ngan (2017). Particles are released within the courtyards at a height of 1.8 m being representative for human exposure. As soon as a particle exits the courtyard volume, the age of that particle, which corresponds to the residence time, is stored and the particle itself is removed from the simulation to reduce computational costs.

When focusing on the time-integrated effect of particles onto a certain volume, the exposure time would be an even better measure than the residence time. The exposure time also considers the re-entrainment of particles. However, Lo and Ngan (2017) found that the number of re-entrainment events was only small in their analysis of a street-canyon flow which is comparable to the situation studied in Section 4. Therefore, the computationally less expensive option of measuring the residence time is used in Section 4.

2.2.3 Velocity Ratio

The ventilation of an urban area can also be quantified by the reduction of the wind velocity compared to a reference area. Often, the wind-speed reduction is computed at the pedestrian height level, which is usually defined at $2\,\mathrm{m}$ height. The velocity reduction is defined by the velocity ratio

$$V_r = \frac{V_{2\mathrm{m}}}{V_{\mathrm{ref}}}, \tag{2.44}$$

where $V_{2\mathrm{m}}$ is the mean velocity at $2\,\mathrm{m}$ height within the urban area and V_{ref} is a reference velocity. Often, V_{ref} is defined at a height well above the urban canopy layer (e.g. Ng, 2009; Letzel et al., 2012). However, in this case, V_r does not only account for the velocity reduction due to blockage by buildings, but also considers the vertical velocity profile within the UBL. Comparing V_r under different atmospheric stratification is, hence, dominated by the differences of the vertical wind profiles. Distinguishing between ventilation reduction due to different blockage behaviour of the buildings or due to different vertical velocity profiles is not possible using this definition.

To exclude the influence of the stratification on V_r, V_{ref} must be defined at the same height as $V_{2\mathrm{m}}$. In Section 5, V_{ref} is calculated also at $z = 2\,\mathrm{m}$ but within the approaching flow over the non-obstructed area in front of the city:

$$V_{\mathrm{ref}} = V_{2\mathrm{m}}\big|_{\text{approaching area}}. \tag{2.45}$$

Using this definition of V_{ref}, only the blockage of the flow by the buildings influences V_r while the vertical velocity profile has no influence. Hence, V_r can be used to compare the blockage behaviour of the buildings between different stratification.

The velocities $V_{2\mathrm{m}}$ and V_{ref} are defined using the three-dimensional wind vector, i.e.

$$V_{2\mathrm{m}} = \left.\sqrt{u^2 + v^2 + w^2}\,\right|_{z=2\mathrm{m}}. \tag{2.46}$$

This definition also considers the increased vertical motions in the convective case.

3 Evaluation of the Dynamic Core of the PALM Model System 6.0 in a Neutrally Stratified Urban Environment: Comparison between LES and Wind-tunnel Experiments

3.1 Declaration of Contributions

K. Surm, B. Leitl and F. Harms created and conducted the wind-tunnel experiments. T. Gronemeier, S. Raasch and B. Maronga created the simulation setup. T. Gronemeier carried out the simulations and precursor test simulations with supervision of S. Raasch. T. Gronemeier and K. Surm conducted the data analysis with supervision of B. Leitl, F. Harms, S. Raasch and B. Maronga. T. Gronemeier wrote the manuscript with support of all co-authors. Comments of two anonymous referees helped to improve the final version of the manuscript.

3.2 Research Article

Geoscientific
Model Development

Evaluation of the dynamic core of the PALM model system 6.0 in a neutrally stratified urban environment: comparison between LES and wind-tunnel experiments

Tobias Gronemeier[1], Kerstin Surm[2], Frank Harms[2], Bernd Leitl[2], Björn Maronga[1,3], and Siegfried Raasch[1]

[1]Institute of Meteorology and Climatology, Leibniz University Hannover, Hanover, Germany
[2]Meteorological Institute, Universität Hamburg, Hamburg, Germany
[3]Geophysical Institute, University of Bergen, Bergen, Norway

Correspondence: Tobias Gronemeier (gronemeier@muk.uni-hannover.de)

Abstract. We demonstrate the capability of the PALM model system version 6.0 to simulate neutrally stratified urban boundary layers. Our simulation uses the real-world building configuration of the HafenCity area in Hamburg, Germany. Using PALM's virtual measurement module, we compare simulation results to wind-tunnel measurements of a downscaled replica of the study area. Wind-tunnel measurements of mean wind speed agree within 5 % on average while the wind direction deviates by approximately 4°. Turbulence statistics similarly agree. However, larger differences between measurements and simulation arise in the vicinity of surfaces where building geometry is insufficiently resolved. We discuss how to minimize these differences by improving the grid layout and give tips for setup preparation. Also, we discuss how existing and upcoming features of PALM like the grid nesting and immersed boundary condition help improve the simulation results.

1 Introduction

The PALM model system version 6.0 is the latest version of the large-eddy simulation (LES) model PALM. PALM is a FORTRAN-based code that simulates atmospheric and oceanic boundary layers. The development of version 6.0 followed the framework of the Urban Climate Under Change ([UC]^2) project, which is funded by the German Federal Ministry of Education and Research (Scherer et al., 2019; Maronga et al., 2019). [UC]^2 aims to develop a fully func-tional urban climate model capable of simulating the urban canopy with grid sizes down to 1 m. Maronga et al. (2015, 2020a) provide a detailed description of the PALM model system. A variety of urban boundary layer studies have already used PALM successfully (e.g. Letzel et al., 2008; Park et al., 2012; Kanda et al., 2013; Kurppa et al., 2018; Wang and Ng, 2018; Paas et al., 2020). Built upon PALM version 4.0, the latest version contains many new features and improvements of existing components in the model system. One of the most impactful changes is the new treatment of surfaces within PALM. While previous versions of PALM did not distinguish between different surface types, it is now possible to directly specify a surface type to each individual solid surface within a model domain via the land-surface model (Maronga et al., 2020a) or the building-surface model (Resler et al., 2017; Maronga et al., 2020a). Also, a fully three-dimensional obstacle representation is now possi-ble. Previous versions allowed only a 2.5-dimensional repre-sentation of obstacles (no overhanging structures like bridges or gates). These additions required extensive re-coding of PALM 4.0, which affected the dynamic core of the model. The re-coding included the modularization of the code base, which led to a re-ordering and re-grouping of code parts into several internal modules (e.g. constant flux-layer module, boundary-conditions module, and turbulence-closure mod-ule). Changes to the dynamic core are technical changes, only. The underlying physical equations in version 6.0 are identical to version 4.0.

Other studies evaluated previous versions of PALM against wind-tunnel measurements, real-world measurements, and other computational fluid dynamics (CFD) codes (Letzel et al., 2008; Razak et al., 2013; Park et al., 2015; Gronemeier and Sühring, 2019; Paas et al., 2020). The significant changes to PALM's code base in version 6.0, however, produce different results compared to former versions. These differences are due to either roundoff errors or code defects. Roundoff errors occur because the order of code execution differs from version 6.0 to 4.0. Old code defects may have been repaired when the dynamic core was modified, while new code defects may have been introduced. Hence, version 6.0 requires a new evaluation, from scratch, to ensure confidence in the results of the PALM model system.

Because of the complexity of PALM, evaluating the model is a lengthy and costly exercise. A complete validation of all model components would easily go beyond the scope of a single article. In this study, we therefore focus on the evaluation of the model's flow dynamics, which make up the core of the model system and build the foundation for all other features within PALM. To isolate the dynamics from all other code parts, we operate PALM in a pure dynamic-driven mode, i.e. we switched off all thermal effects (temperature and humidity distribution, radiation, surface albedo, heat capacity, etc.). We can then compare the simulation results with wind-tunnel measurements using the methodology of Leitl and Schatzmann (2010). While it is virtually impossible to neglect temperature or humidity effects in real-world measurements, wind-tunnel experiments can provide exactly the same idealized conditions as those used in our idealized simulation. Paas et al. (2020) compared PALM simulations to measurements of a mobile measurement platform. Although they found overall good agreement between PALM and the measurements, some non-resolved obstacles like trees complicated the comparison at several points and led to differences in results. Hence, we decided to compare PALM against an idealized wind-tunnel experiment for this study.

We use a real-world building configuration from the HafenCity area of Hamburg, Germany. A real-world building setup is advantageous in that it can include a variety of building configurations, ranging from solitary buildings to complex street canyons, within a single simulation. Likewise, it may show the capability of PALM to correctly reproduce a complex, realistic wind distribution.

We initially designed the evaluation study as a blind test where only the boundary conditions (building layout, approaching flow profile, location of measurements) but no further results of the wind-tunnel experiment were available to conduct the PALM simulation. Such a blind test has the benefit of preventing model tuning and indicates how accurately a model can reproduce reference data based only on boundary conditions. This procedure also reflects a more realistic use case where reference data might not exist. However, after comparing results from both PALM and wind-tunnel experiments, we identified several errors in the simulation setup. Errors in building height and the roughness representation within the upwind region were most prominent. We then updated the PALM setup with all identified flaws corrected and re-simulated the case. Although there are methods to adjust CFD results to better match to measurements (e.g. Blocken et al., 2007), these adjustments depend on the individual case, must be re-calculated for each case, and are only usable if detailed reference data are available. We did not implement such setup tuning for the revised simulation setup. We made corrections solely to input parameters that were available but not considered (layout of roughness elements within the wind tunnel) or not correct (incorrect building heights) during the initial blind-test simulation.

2 Experimental setup

2.1 Wind-tunnel experiment

We used measurements made at the Environmental Wind Tunnel Laboratory (EWTL) facility "WOTAN" at the University of Hamburg, Germany. The 25 m long wind tunnel provides an 18 m long test section equipped with two turn tables and an adjustable ceiling. The cross section of the tunnel measures 4 m in width and 3 m in height. Figure 1 shows a photograph inside the wind tunnel for reference. For each wind-tunnel campaign, a neutrally stratified boundary layer flow is generated by a carefully optimized combination of turbulence generators at the inlet of the test section and a compatible floor roughness. For the present study, we modelled a boundary layer flow to match full-scale conditions for a typical urban boundary layer measured at a 280 m tall tower in Billwerder, Hamburg. The mean wind profile fits a logarithmic wind profile with a roughness length $z_0 = (0.66 \pm 0.22)$ m and a power law with a profile exponent $\alpha = 0.21 \pm 0.02$. Figure 2 depicts the approaching flow profile for a modelled wind direction of 110°.

The miniature replica of the HafenCity, Hamburg, Germany, has a scale of $m = 1/500$ and represents an area of 2.6 km^2 (see Fig. 1). Standard quality measurements during the wind-tunnel experiment proved scale-independence of the results (based on Townsend's hypothesis of self similarity) and allowed scaling of the results from model scale (ms) to full scale (fs). Scaling of space l, time t, and velocity u is achieved via

$$l_{fs} = \frac{l_{ms}}{m},$$ (1)
$$t_{fs} = \frac{t_{ms}}{m}, \text{and}$$ (2)
$$u_{fs} = u_{ms}.$$ (3)

We used a two-dimensional laser doppler anemometry (LDA) system to measure component-resolved flow data at sampling rates of 200–800 Hz (model scale). This measurement method resolves even small-scale turbulence in time at

Figure 1. Photograph of the building setup within the wind-tunnel facility "WOTAN" for an approaching flow of 290°. Please note that contrary to the depicted orientation, an approaching flow from 110° was used in this study.
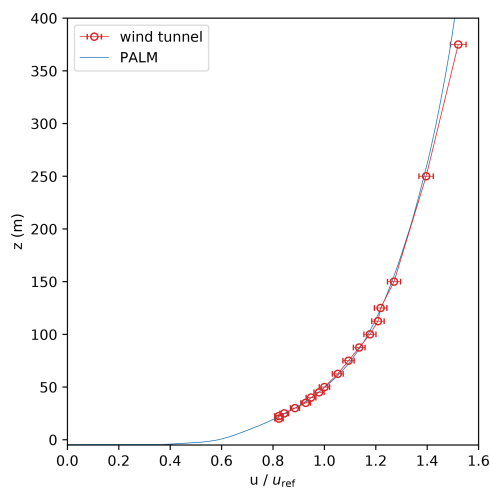

Figure 2. Mean profiles of the approaching flow for the wind-tunnel experiment and the PALM simulation normalized with the reference velocity $u_{ref} = u(z = 50\,\text{m})$. Note that $z = 0\,\text{m}$ is defined at street-level height while the lowest level within both experiments was at $z = -5\,\text{m}$, which is the water-level height.

most measurement locations. We recorded a 3 min time series at each measurement location, which corresponds to a period of about 25 h at full scale. Prandtl tubes continuously monitored the reference wind speed close to the tunnel inlet. For the model evaluation case presented here, measurements were taken at 25 different locations within the building setup as shown in Fig. 3. As the measurements were orig-

inally planned and used for a different study focusing on near-ground ventilation and pedestrian wind comfort, locations were not specifically chosen for the present study. However, the measurements still cover a variety of aspects of the flow within the building canopy including open areas, narrow and wide street canyons, and intersections.

2.2 PALM simulation

We used the PALM Model System 6.0, revision 3921, to conduct the simulation for this study. We operated PALM using a fifth-order advection scheme after Wicker and Skamarock (2002) in combination with a third-order Runge–Kutta time-stepping scheme after Williamson (1980). Maronga et al. (2015, 2020a) provide a detailed description of the PALM model. We conducted the simulation at full scale with a domain size of 6000 m by 2880 m horizontally and 601 m vertically at a spatial resolution of $\Delta x = \Delta y = \Delta z = 1\,\text{m}$ in each direction. This domain resulted in approximately 10.4×10^9 grid points in our staggered Arakawa C-grid (Harlow and Welch, 1965; Arakawa and Lamb, 1977). The study region, i.e. the HafenCity area, was situated downstream of the simulation domain. We aligned the mean flow direction with the x direction. Hence, we rotated the model domain counter clockwise by 200° to produce a mean wind direction of 110°.

Figure 4 displays the building layout used in PALM. PALM uses the mask method (Briscolini and Santangelo, 1989) for topography, where a grid volume is either 100 % fluid or 100 % obstacle. In combination with PALM's rectilinear grid, this method can cause non-grid aligned buildings
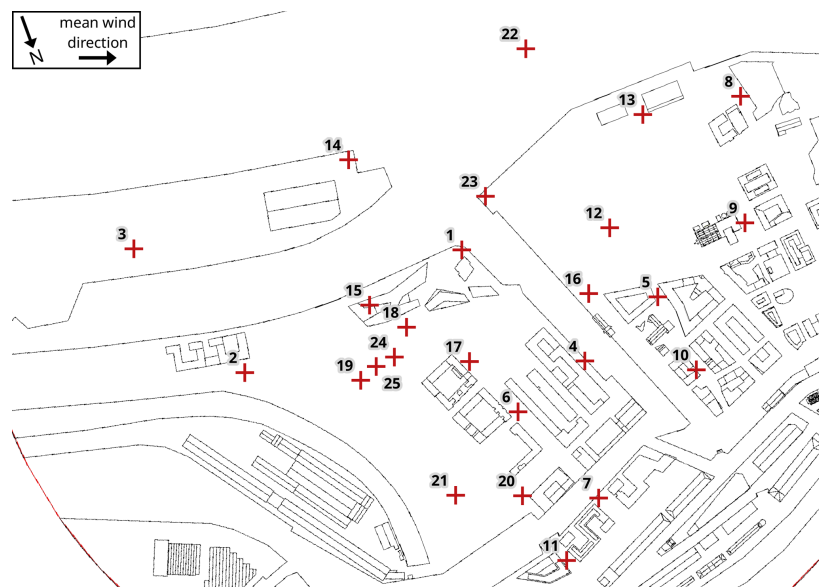
Figure 3. Building layout used in the wind-tunnel experiment. Measurement locations are marked and labelled by their respective number.
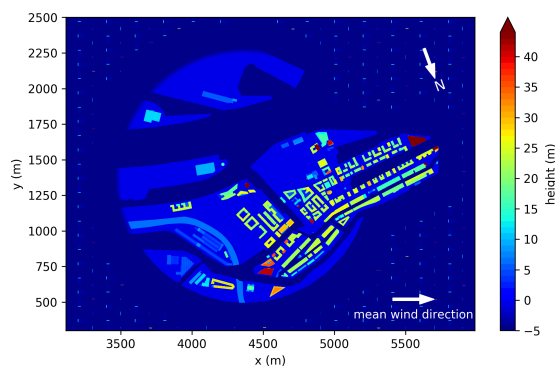

Figure 4. Building layout and heights as used in the PALM simulation. The x direction is oriented to follow the mean wind direction. The total domain size is 6000, 2880, and 601 m in the x, y, and z direction, respectively. Note that $z = 0$ m is defined at street-level height while the lowest level within both experiments was at $z = -5$ m, which is the water-level height.

to have inconsistent geometries (step-like) when compared with the wind-tunnel replica.

We based the setup for this study on the settings used by Letzel et al. (2012). A heterogeneous building setup usually requires a non-cyclic boundary condition along the mean flow direction to ensure that building-induced turbulence is not recycled into the analysis area. However, tests with non-cyclic boundary conditions along the mean flow showed that simulations would require extremely long simulation times to generate a stationary state. Hence, we used cyclic bound-

ary conditions instead, which reduced the required CPU time significantly. We extended the domain in mean flow direction (x direction) to allow the building-induced turbulence to dissipate before the flow hits the target area again due to the cyclic conditions. Because we simulated an ideal, neutrally stratified case that neglected trace gases and the like within the city area, there was no disadvantage to use cyclic boundary conditions. After a simulation time of 1.5 h, the simulation reached a steady state.

We assumed a constant flux layer between the surface and the first computational grid level to calculate the surface shear stress. The exact value of the roughness length, z_0, for the building surfaces is not known from the wind-tunnel experiment. Therefore, it was estimated as $z_0 = 0.01$ m. This value was recommended by Basu and Lacser (2017) who state that $z_0 \leq 0.02 \cdot \min(\Delta z)$. Due to the staggered grid, the first computational level was positioned $0.5 \Delta z$ above the surface. Hence, $z_0 = 0.02 \cdot 0.5 \cdot 1 \, \text{m} = 0.01$ m.

The estimated roughness length of the approaching flow in the wind-tunnel experiment was $z_0 = (0.66 \pm 0.22)$ m (see Sect. 2.1). Surface-flux parameterizations cannot represent such a large roughness length at the simulated resolution (1 m). Therefore, we explicitly resolved the roughness using roughness elements of the exact same shape and layout as those elements used in the wind-tunnel experiment. This methodology produced a boundary layer flow in the simulation similar to that observed in the wind-tunnel experiment (see Fig. 2).

To match the conditions within the wind tunnel, we considered a strictly neutral atmosphere with potential tempera-

ture being constant over time. We also neglected the Coriolis force.

Munters et al. (2016) reported persistent streak-like artefacts in the flow field that are oriented along the mean wind direction for LES of neutral flows using cyclic boundary conditions. Such streaks naturally develop within the neutral boundary layer, reach lengths of several kilometres, and move along the mean wind direction while remaining stationary in the span-wise direction. These streaks form randomly and have a limited lifetime. In combination with cyclic boundary conditions, however, the start and end of a streak can merge, forming an infinite streak that is self-containing and persistent in time. To avoid the artificial persistence of these structures by cyclic boundary conditions, we use the shifting method of Munters et al. (2016). This method breaks up the infinite and persistent streak-like artefacts and ensures a natural dissipation. We shifted the flow by 300 m in the y direction, i.e. perpendicular to the mean wind direction, before entering the domain at the left boundary.

The wind field initializes with a turbulent wind field from a precursor simulation via the cyclic-fill method (Maronga et al., 2015). The setup of the precursor simulation was similar to the main simulation but with a reduced domain size of 600 m by 600 m in the horizontal direction. To initialize the precursor simulation, we measured the normalized approaching wind profile in the wind tunnel and scaled the wind speed to $4\,\mathrm{m\,s^{-1}}$ at 50 m height to obtain a representative wind speed for within the canopy layer. The fixed wind speed was $6.26\,\mathrm{m\,s^{-1}}$ at the top boundary for the precursor and main simulation.

The total simulation time of the main simulation was 4 h. The simulation achieved a steady state after the first 1.5 h. We used the results from the final 2.5 h for the analysis presented here (see Sect. 3).

Figure 2 shows the mean wind profile of the flow approaching the building area during the analysis time as well as the approaching flow of the wind-tunnel experiment. Note that we defined the street-level height at $z = 0\,\mathrm{m}$ and the lowermost height at water level, which is 5 m below street level (see Fig. 4). Hence, the approaching wind profile shown in Fig. 2 starts at $z = -5\,\mathrm{m}$.

2.3 Measurement stations

Within the wind-tunnel experiment, wind speed was measured at certain measurement stations within the building array. Figure 3 shows the locations of the measurement stations. To be able to mirror the measurements as best as possible, we used the virtual measurement module of PALM (Maronga et al., 2020a). This module defines several virtual measurement stations within the model domain via geographical coordinates. The model domain must be georeferenced in order to identify the grid points closest to the measurement location. PALM references the geographical

coordinates based on the coordinates of the lower left corner of the domain and the domain's orientation.

When mapping the measurement stations onto the PALM grid, there were two difficulties. First, there was not always a grid point available at the exact location of the measurement within the wind-tunnel experiment. Therefore, measurement positions can differ between the virtual and wind-tunnel measurements by a distance of less than 1 m. Second, the topography in the vicinity of a measurement point at the virtual stations may differ from the wind-tunnel stations due to the topography representation used in PALM (see Sect. 2.2). To overcome these two issues, we also recorded virtual measurements from the grid points neighbouring a measurement position. In post-processing, we analysed the area of each measurement station and selected the measurement from the grid point that best fit the wind-tunnel measurements. Each measurement station recorded vertical profiles with a sampling rate between 8.7 and 11.2 Hz (measurements recorded during each time step).

3 Results

3.1 PALM simulation

The PALM simulation required a spin-up time of 1.5 h, which is evident by the time series of the domain-averaged kinetic energy $E = 0.5\sqrt{u^2 + v^2 + w^2}$ and the friction velocity u_* (see Fig. 5). Both quantities stabilized after 1.5 h at approximately $E = 15.4\,\mathrm{m^2\,s^{-2}}$ and $u_* = 0.16\,\mathrm{m\,s^{-1}}$. Therefore, we only evaluated data from the last 2.5 h of the simulation.

Figure 6 shows the horizontally and time-averaged vertical profile of the stream-wise component of the vertical momentum flux wu. The vertical momentum flux wu is split into a resolved component and a sub-grid scale (SGS) component. An SGS model parameterizes the SGS component. The less the SGS model contributes to the flux the better resolved is the turbulence causing the flux. The ratio of the resolved and the total momentum flux is close to 1 revealing that the simulation domain properly resolved the turbulence (see Fig. 6).

Turbulent structures tend to become smaller the closer they get to the surface. Hence, at the surface, the constant grid spacing resolves less turbulence (Maronga et al., 2020b). However, the ratio between resolved and total wu exceeds 0.9 except for the lowest two grid levels where the ratio reduces to 0.78. The discontinuity at $z = 15\,\mathrm{m}$ is related to the roughness elements. Most of these elements extend to $z = 15\,\mathrm{m}$, causing the disturbance in the vertical wu profile at that height.

To visualize the turbulent structures, Fig. 7 shows a snapshot of the magnitude of the three-dimensional vorticity as a proxy for turbulence. Strong turbulence (yellow and red structures) occurs in the vicinity of buildings, while weak turbulence occurs above smooth surfaces. Roughness elements
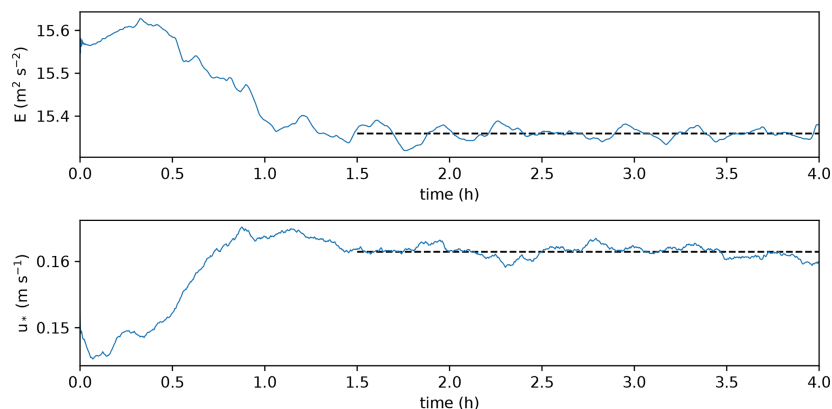
Figure 5. Time series of the total kinetic energy E and the friction velocity u_* of the PALM simulation.
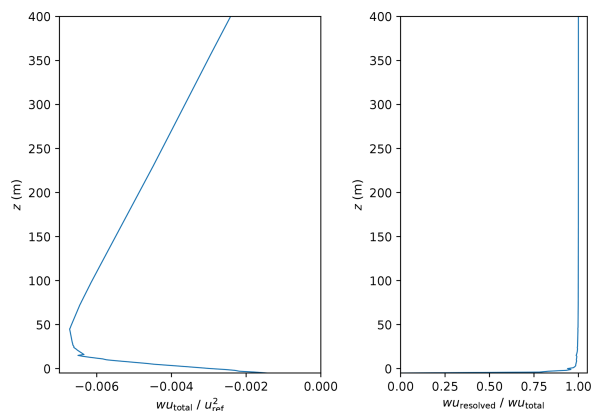

Figure 6. Mean profile of the vertical momentum flux and the ratio between resolved and total flux, averaged over the entire domain of the PALM simulation. Please note the two different horizontal scales for momentum flux (bottom scale) and flux ratio (top scale).

that are not visible within Fig. 7 cause the strong turbulence outside of the building array.

3.2 Comparison between wind tunnel and PALM

To compare the simulation and the wind-tunnel experiment, we must first normalize the results as the simulation and wind-tunnel experiment were conducted on different scales and mean wind speeds. The reference wind speed u_{ref} used for normalization corresponds to the wind speed of the approaching flow at a height of 50 m (full scale). Previously conducted laboratory experiments defined the reference height to be representative of the measured canopy flow. The reference height falls within the range expected to most accurately model a scaled neutrally stratified atmospheric boundary layer wind flow. We report our results at full scale unless otherwise stated.

Figure 8 shows the wind distribution for each measurement station at the lowest measurement height for (a) the wind-tunnel measurements ($z = 3$ m) and (b) the PALM simulation ($z = 2.5$ m). Due to the staggered grid used in PALM (see Sect. 2.2), the positions of the PALM measurements are 0.5 m below their corresponding wind-tunnel measurements. Note that measurement station 15 stands on top of a building where measurements were only available above 18 m height (see Fig. 3). At most measurement stations, the main wind direction in the PALM simulation is similar to the wind-tunnel data. Noticeable differences in the distribution of wind directions occur at stations 6, 7, 10, and 20, where the PALM simulation reports a larger variation in wind direction or a different mean wind direction. On average, the wind speed is 9 % less in the PALM simulation than in the wind-tunnel measurements.

At 10 m height (PALM: 9.5 m), the wind distributions are still very close between PALM and the wind tunnel at most stations (see Fig. 9). Stations 6, 10, and 20 still show noticeable differences. The difference in average wind speed reduces to 5 % between PALM and wind-tunnel results. At 40 m height and above, the difference reduces to less than 2.5 %.

Figure 10 shows scatter plots of wind-tunnel and PALM measurements at each station and height, which are 173 data pairs in total. Looking at the horizontal wind speed U_{hor} and the wind-speed components u and v, PALM underestimates the lower values while higher values compare well to the wind-tunnel measurements. Wind direction d differs by less than 4° on average with a maximum difference of less than 44°. It has to be noted, however, that wind-tunnel measurements might be located between grid points of the PALM grid creating a spatial offset between the measurements. Especially close to obstacles, this spatial offset can lead to differences between both experiments.

Three major reasons caused the general lower wind speeds in the PALM simulation: (i) a mismatch in measurement

Figure 7. View of the volume-rendered instantaneous turbulence structures above the building array. Turbulence is visualized using the magnitude of the three-dimensional vorticity. Green and red indicate low and high values, respectively. The image was rendered using VAPOR (Li et al., 2019, http://www.vapor.ucar.edu/, last access: 2 June 2021) and the background image was designed by freepic.diller/Freepik (http://www.freepik.com, last access: 16 May 2019).

height, (ii) a mismatch in z_0 between both experiments, and (iii) the stepwise building representation caused by PALM's rectilinear grid. The staggered Arakawa C-grid caused the PALM measurements to be located 0.5 m below the corresponding wind-tunnel measurements. PALM calculates u and v at half the height of each grid cell. With a grid size of $\Delta z = 1$ m, u and v are, hence, calculated at heights of 0.5, 1.5, 2.5 m, etc. We chose to not interpolate between the height levels in order to not alter the simulation results by adding additional uncertainty due to the chosen interpolation techniques. When comparing PALM results at 0.5 m above the wind-tunnel measurements, the underestimation of wind-speed reduces to 5 % at 3 m height. Because vertical gradients of the wind-speed decrease with height, differences in measurement heights are less severe at greater heights.

Second, a mismatch of z_0 between both experiments also affects results most significantly at the lowest height levels. This is supported by the fact that we observed the largest difference in mean wind speed (9 % lower wind speed) at the lowest measurement height. Hence, the surfaces in the wind-tunnel experiment might have been smoother than estimated and $z_0 = 0.01$ m might have been too large. In a different not yet published wind-tunnel experiment with similar wall materials of the building model, we observed roughness lengths between 0.002 and 0.01 m. This puts the chosen z_0 for the simulation at the upper end of the possible value range for the roughness within the wind-tunnel experiment.

The third reason, the stepwise building representation, affects results within the entire building canopy layer. Because PALM discretizes obstacles on a rectilinear grid as mentioned in Sect. 2.2, smooth building walls are represented by stepwise surfaces if not aligned with the grid layout. There-

fore, building walls become significantly rougher than they were in the wind-tunnel experiment. This causes higher turbulence and an overall reduced mean wind speed within the building canopy layer.

To better evaluate the deviations between both experiments, we calculated different validation metrics. COST Action 732 (Schatzmann et al., 2010) lists several validation metrics to help evaluate simulation models. The proposed metrics are the factor of two FAC2, the hit rate q, the fractional bias FB, the geometric mean bias MG, the normalized mean square error NMSE, and the geometric variance VG. Additionally, we calculated the correlation coefficient R. These metrics are defined as

$$\text{FAC2} = \frac{1}{N} \sum_i n_i,$$

$$\text{with } n_i = \begin{cases} 1 & \text{if } \frac{1}{2} \leq \frac{P_i}{O_i} \leq 2 \vee \left(|P_i| \leq \delta_a \wedge |O_i| \leq \delta_a\right), \\ 0 & \text{otherwise,} \end{cases}$$

(4)

$$q = \frac{1}{N} \sum_i n_i,$$

$$\text{with } n_i = \begin{cases} 1 & \text{if } \left|\frac{P_i - O_i}{O_i}\right| \leq \delta_r \vee |P_i - O_i| \leq \delta_a, \\ 0 & \text{otherwise,} \end{cases}$$

(5)

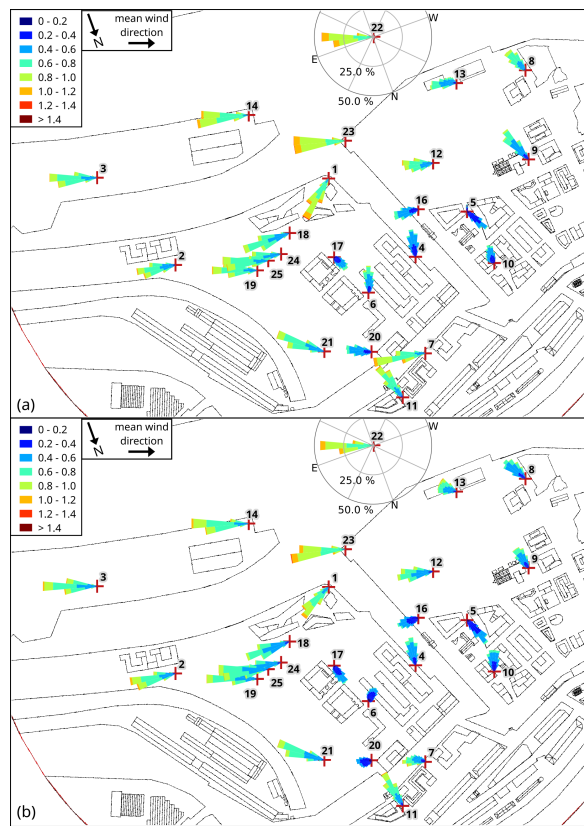**Figure 8.** Wind-speed distribution (wind rose plots) at all measurement stations for **(a)** wind-tunnel measurements and **(b)** the PALM simulation at about 3 m height above street level (wind tunnel: 3 m, PALM: 2.5 m). Axes are only shown for a single station for better overview, but all wind distributions are scaled equal. Numbers indicate the station number.
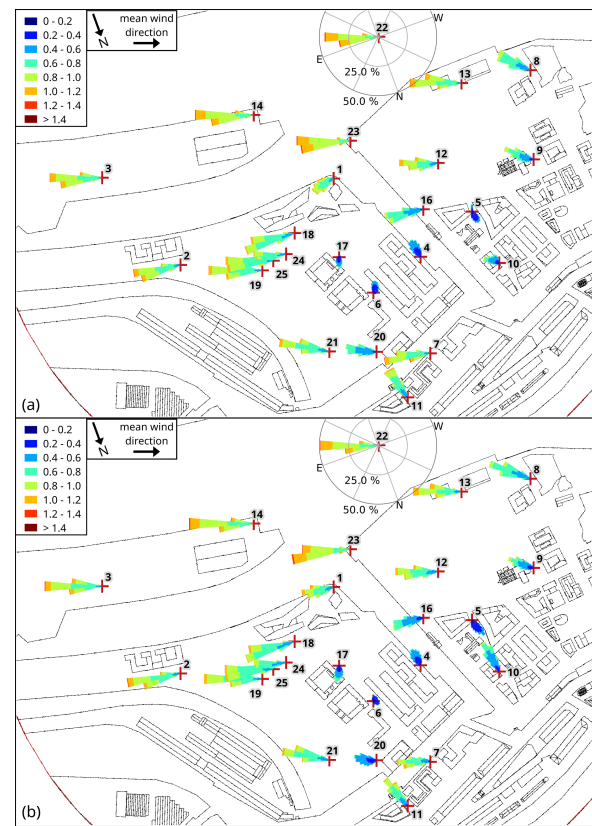

Figure 9. Wind-speed distribution (wind rose plots) at all measurement stations for **(a)** wind-tunnel measurements and **(b)** the PALM simulation at about 10 m height above street level (wind tunnel: 10 m, PALM: 9.5 m). Axes are only shown for a single station for better overview, but all wind distributions are scaled equal. Numbers indicate the station number.

$$R^2 = \left(\frac{1}{N} \frac{1}{\sigma_P \sigma_O} \sum_i (P_i - \overline{P})(O_i - \overline{O}) \right)^2, \quad (6)$$

$$\mathrm{FB} = 2\, \frac{\overline{O} - \overline{P}}{\overline{O} + \overline{P}}, \quad (7)$$

$$\mathrm{MG} = \exp\left(\overline{\ln(\widetilde{O_i})} - \overline{\ln(\widetilde{P_i})} \right) \quad \text{with} \quad \widetilde{\varphi} = \max(\varphi, \delta_\mathrm{a}), \quad (8)$$

$$\mathrm{NMSE} = \frac{1}{N} \sum_i \frac{(P_i - O_i)^2}{\overline{P}\,\overline{O}}, \quad (9)$$

$$\mathrm{VG} = \exp\left(\overline{\left(\ln(\widetilde{O_i}) - \ln(\widetilde{P_i}) \right)^2} \right) \quad \text{with} \quad \widetilde{\varphi} = \max(\varphi, \delta_\mathrm{a}), \quad (10)$$

with O_i being the observed (wind tunnel), P_i the predicted (PALM) measurements, δ_r the relative deviation threshold, δ_a the absolute deviation threshold, and N the total number of

measurements; the overline denotes an average over all measurements and σ_P and σ_O are the standard deviation of P and O, respectively. We set the deviation thresholds to $\delta_\mathrm{r} = 0.25$ for all variables as recommended by VDI (2005). Table 1 lists the δ_a used for all variables.

We calculated the validation metrics for the horizontal wind speed U_hor, the wind-velocity components u and v, their variance σ_u^2 and σ_v^2, as well as for the turbulence intensities I_u and I_v that are defined as the standard deviation divided by the mean horizontal wind speed (see Table 1). In general, all validation metrics are close to their ideal values indicating a high agreement between both experiments. The largest deviation between both experiments is apparent for v where both FAC2 and q give the lowest values. However, q is still within the acceptable range of $q \geq 0.66$, defined by VDI (2005). The metrics also reflect the abovementioned findings that PALM underestimates the mean wind speed. Both FB and MG indicate an underestimation of ap-

Table 1. Calculated validation metrics for different variables. The rightmost column gives the respective value of a perfect match between simulation and observation.

Metric	u/u_{ref}	v/u_{ref}	$U_{\mathrm{hor}}/u_{\mathrm{ref}}$	$\sigma_u^2/u_{\mathrm{ref}}^2$	$\sigma_v^2/u_{\mathrm{ref}}^2$	I_u	I_v	Ideal
FAC2	0.98	0.73	1	0.98	0.98	1	1	1
q	0.91	0.70	0.96	0.82	0.79	0.93	0.91	1
R^2	0.97	0.87	0.96	0.57	0.55	0.83	0.85	1
FB	–	–	0.03	-0.06	0.19	-0.08	0.03	0
MG	–	–	1.05	0.95	1.2	0.93	1.04	1
NMSE	–	–	0.01	0.07	0.21	0.05	0.07	0
VG	–	–	1.01	1.05	1.08	1.02	1.02	1
δ_{a}	0.025	0.025	0.025	0	0	0	0	
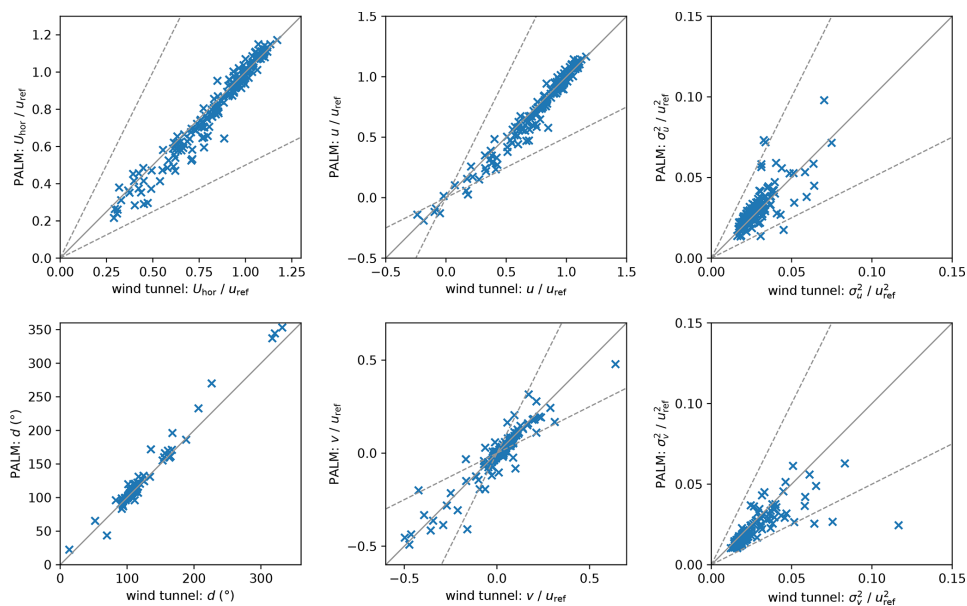
Figure 10. Scatter plots of wind tunnel and PALM measurements of horizontal wind speed U_{hor}, wind direction d, wind-velocity components u and v, and their variance σ_u^2 and σ_v^2 for all 25 measurement stations and all heights (173 data pairs in total). Solid lines indicate perfect agreement and dashed lines indicate the area between a deviation factor of 0.5 and 2.

proximately 5 % (MG = 1.05). The metrics also indicate an underestimation of σ_v of 20 % (MG = 1.2), which is visible in Fig. 10. However, all metrics lie well within the margins reported by Hanna et al. (2004) for an acceptable performing model. These margins are FAC2 > 0.5, |FB| < 0.3, 0.7 < MG < 1.3, NMSE < 4, and VG < 1.6.

Hertwig et al. (2017) recommend to evaluate the shape parameters of the wind speed distributions of u and v when comparing LES and wind-tunnel results. Figure 11 shows the skewness γ and the excess kurtosis β of u and v. Between both experiments, γ_u mostly agrees and shows either symmetrical distributions ($\gamma_u \approx 0$) or a positive skew. For v, distributions tend to have a lower skewness in PALM than in the wind-tunnel measurements. Also, β_v is smaller meaning that the distributions are less peaked. This is also related to

the higher roughness in the PALM simulation because this produces a wider spread of the distribution with a less pronounced peak, resulting in lower β and (in case of a positive average as is the case here) γ. Again, this is more pronounced in the span-wise wind component v.

The higher roughness and enhanced turbulence lead to a less correlated flow and reduced length scales. Figure 12 displays the comparison of length scales L_u and L_v of the u and v component, respectively. We calculated the length scales based on the integral timescale T:

$$L_\varphi = T_\varphi u_{\mathrm{ref}}, \tag{11}$$

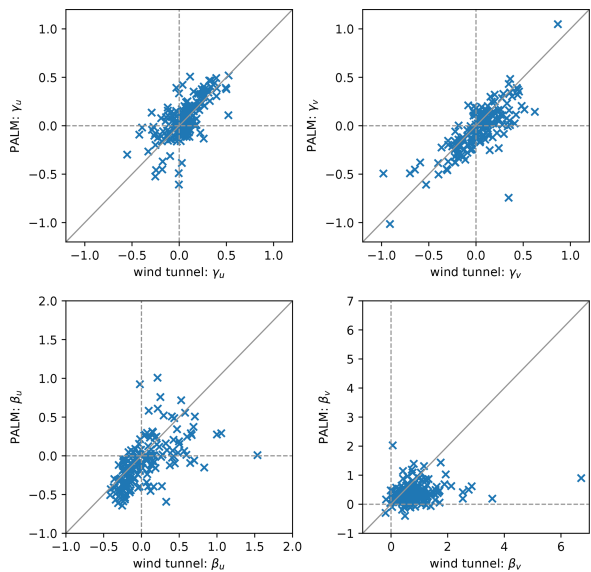where T is calculated using the auto-correlation function R_{a}:

Figure 11. Scatter plots of wind tunnel and PALM measurements of skewness γ and excess kurtosis β of the horizontal wind velocity components for all 25 measurement stations and all heights (173 data pairs in total). Solid lines indicate perfect agreement.

$$\int_0^{T_\varphi} R_{a,\varphi}(t_l)dt_l = e^{-1}$$

$$\text{with } R_{a,\varphi}(t_l) = \frac{1}{\sigma_\varphi^2}\overline{(\varphi(t) - \overline{\varphi}(t))\,(\varphi(t+t_l) - \overline{\varphi}(t+t_l))}$$

$$\text{for } \varphi \in \{u, v\}, \tag{12}$$

with t_l being the time lag.

Most striking are the considerably lower values of L_v within the PALM simulation. However, most data points still lie within the factor-of-two margins: $\text{FAC2}(L_v) = 0.8$. PALM tends to underestimate low L_u and overestimate low L_v.

In the following, we compare the vertical profiles recorded at the measurement stations. Because many vertical profiles showed nearly identical behaviour at different stations, we limit the discussion to three stations: 4, 11, and 7. We chose these stations as examples of a good, an average, and a relatively poor agreement, respectively, between the simulation and the wind-tunnel measurements.

Figure 13 shows vertical profiles of U_{hor}, d, u, and v, as well as turbulence intensity I, skewness γ, excess kurtosis β, and length scale L for u and v measured at station 7. Error bars show the standard deviation of u and v. The blue shaded area shows the range of values of the neighbouring grid points within PALM at the respective measurement station.
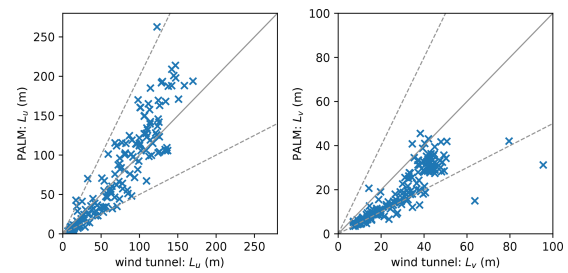
Figure 12. Scatter plots of wind tunnel and PALM measurements of the length scales L_u and L_v of the velocity components u and v, respectively, for all 25 measurement stations and all heights (173 data pairs in total). Solid lines indicate perfect agreement and dashed lines indicate the area between a deviation factor of 0.5 and 2.

Station 7 is situated at the opening of a street canyon within the lee of a building edge (see Fig. 3). Because the surrounding building walls were not aligned with the PALM grid, the building edge had a different shape within the simulation than in the wind-tunnel experiment. This shape difference created an enlarged corner vortex in the simulation. The vortex increased the turbulence and decreased the mean wind speed at station 7 compared to the wind-tunnel results, as shown in Fig. 13. Also, d is affected and deviates from the wind-tunnel results. The effect of rougher building walls by the stepwise representation is limited to the canopy layer. Therefore, d, I_u, and I_v agree significantly better with the wind-tunnel measurements above the rooftop height that is situated between 26 and 36 m in the vicinity of station 7. Due to higher turbulence below the rooftop level, β_v decreases, indicating a less peaked distribution, while the lower γ_u indicates larger tails towards low u values. The higher turbulence also causes L to be shorter within the canopy. Above the canopy layer, the mean wind speed and length scales are larger than in the wind-tunnel experiment because of a higher vertical momentum flux in the simulation caused by the higher roughness within the canopy layer. Similar behaviour can be found at station 20 (profiles not shown), which is located close to a windward building corner. In this case, the blocking effect of the building is increased because of the broader building edge, causing significant differences in wind-direction distribution and mean wind speed (see Figs. 8 and 9).

Profiles not affected by corner flows or the blocking effect tend to agree better between PALM and wind-tunnel measurements. Station 11, positioned at the centre of a street canyon (see Fig. 3), serves as an example of such a measurement location. Profiles tend to agree significantly better within the canopy layer than for station 7, as shown in Fig. 14. Higher deviations between the experiments appear close to the rooftop height (between 26 and 36 m). The roofs of the surrounding buildings have small structures that might not be sufficiently resolved. Hence, the details of the build-
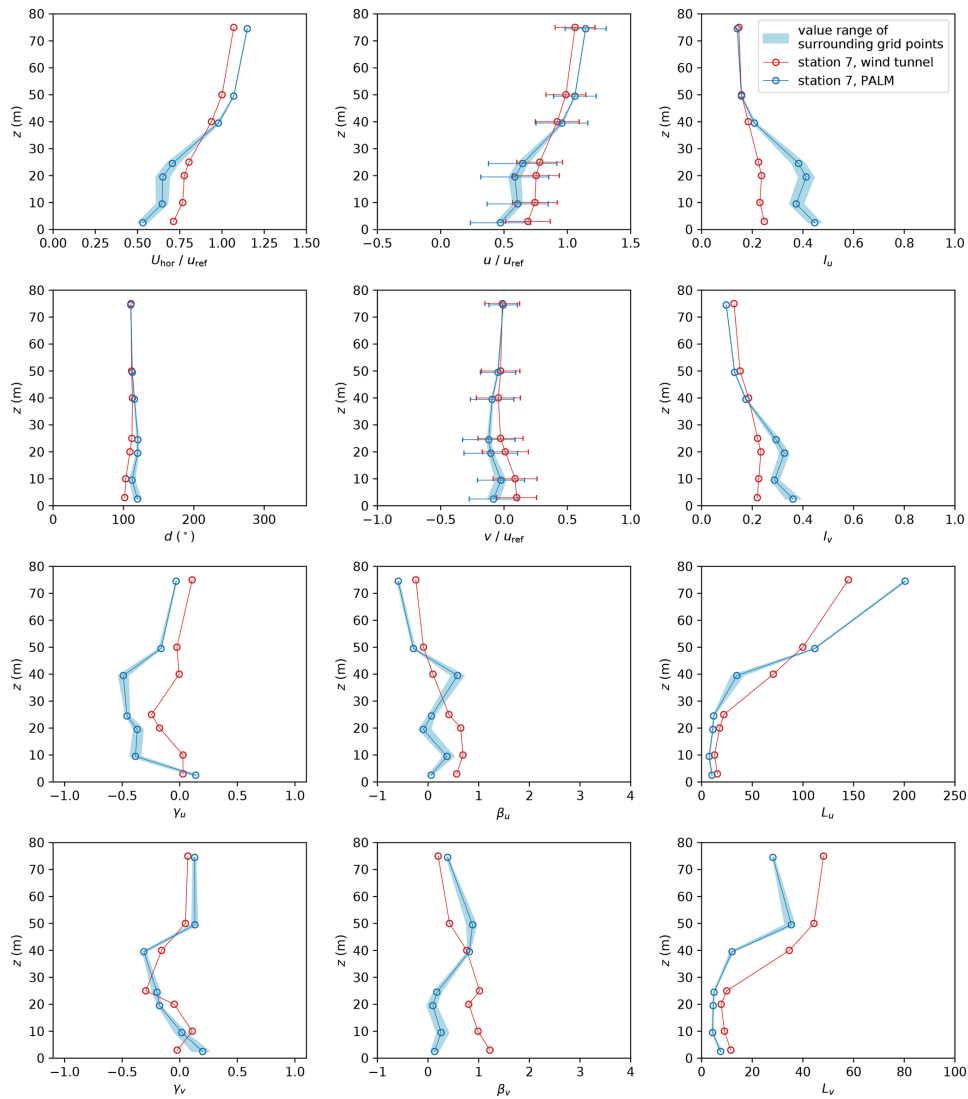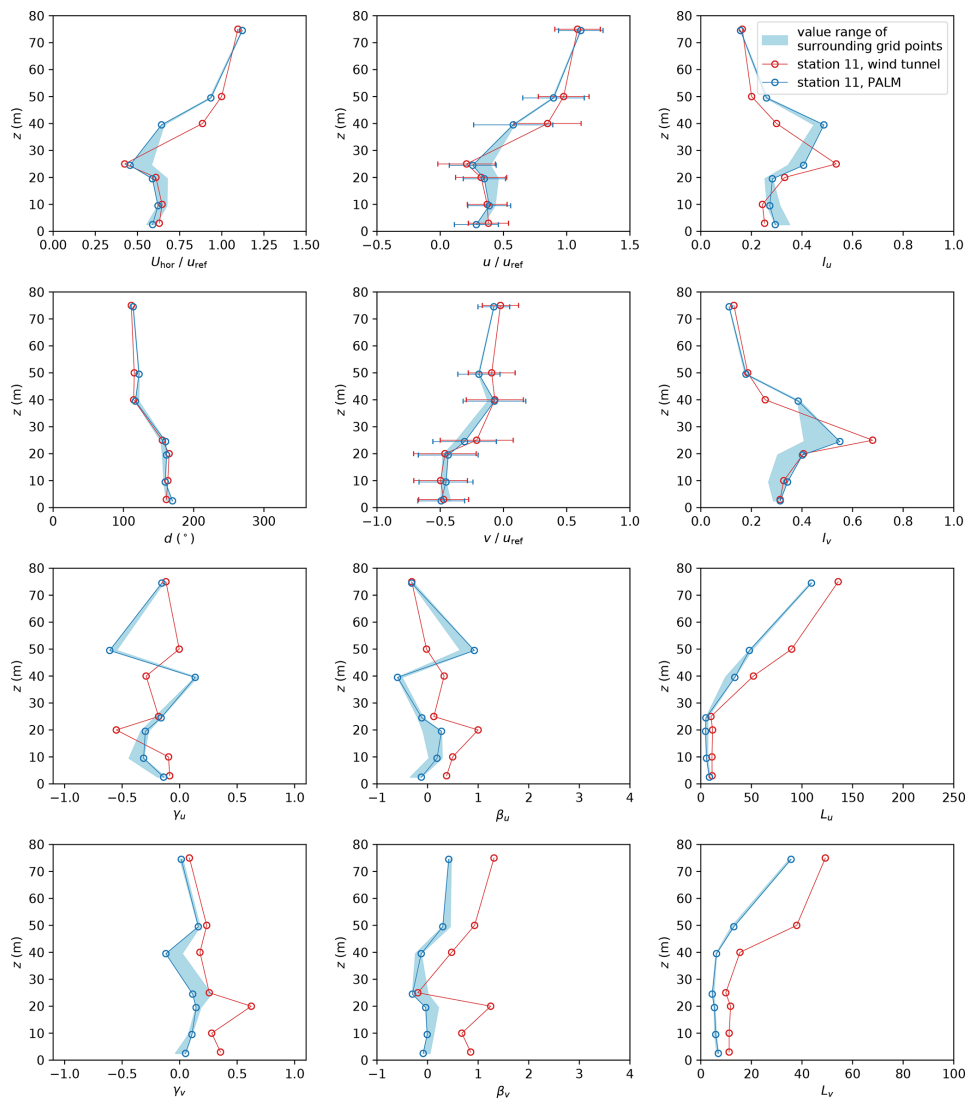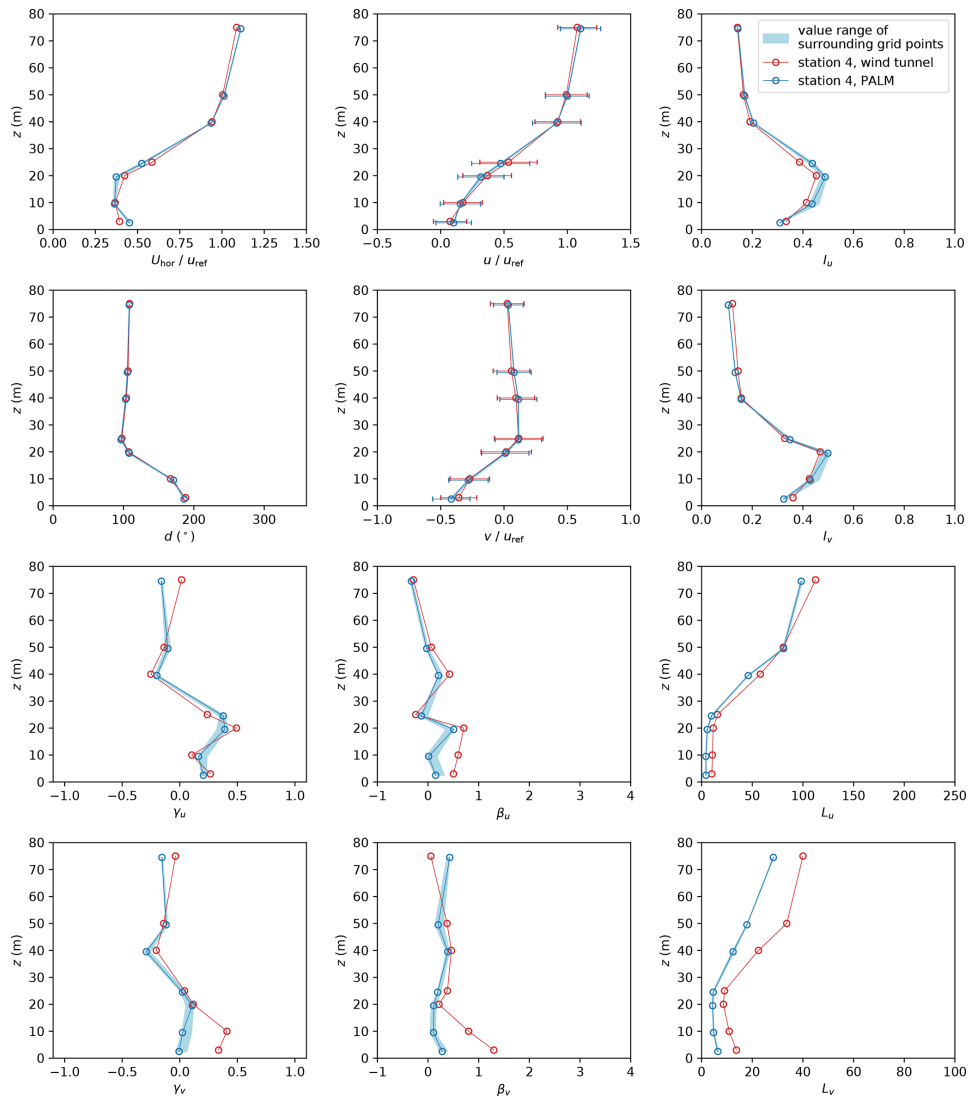
Figure 13. Profiles of mean horizontal wind speed U_{hor}, wind direction d, and wind components u and v as well as turbulence intensity I, skewness γ, excess kurtosis β, and length scale L of both wind velocity components u and v at measurement station 7. Error bars denote the standard deviation of the respective quantity. Note that $z = 0$ denotes street-level height.

ing layout differ between the simulation and the wind tunnel at station 11. Stations 5, 6, 10, and 17 show results similar to those of station 11. Figure 14 shows a large value range of the profiles as indicated by the blue-shaded areas. This large range shows that profiles vary significantly inside the street canyon depending on the distance to the building walls. Hence, it is very important to place the measurements correctly in the simulation if they are situated in close vicinity to buildings.

Station 4 is located at the leeward site of a flat-roofed building (see Fig. 3). Also, no building corners that could produce blocking effects or corner flows are within the proximity of station 4. Profiles at station 4, displayed in Fig. 15, show only small deviations between the two experiments. The rougher wall, generated by the building representation, produces larger turbulence and a less peaked distribution of u and v within the canopy layer. However, results agree significantly better at station 4 compared to station 7 and 11. Hence, PALM reproduces the wind field better if the building structures are less complex.

Figure 16 shows the spectral energy density S measured at station 4 (left panel) and station 11 (right panel) at the pro-

Figure 14. Profiles of mean horizontal wind speed U_{hor}, wind direction d, and wind components u and v as well as turbulence intensity I, skewness γ, excess kurtosis β, and length scale L of both wind velocity components u and v at measurement station 11. Error bars denote the standard deviation of the respective quantity. Note that $z = 0$ denotes street-level height.

file top, rooftop, and near the surface (top, centre, and bottom row, respectively). Spectra measured at station 7 are comparable to those of station 11 and are therefore not shown. The covered range of frequencies f differ between PALM and wind-tunnel measurements because the sampling rate of the measurements and the measured time interval vary between the PALM and the wind-tunnel experiment. However, results of both experiments overlap over a large range of frequencies.

The spectra of u and v coincide to a high degree between the simulation and the wind-tunnel measurements at

all heights. At both stations, the spectra show an exponential decrease between $\frac{fz}{U_{\mathrm{hor}}} = 2$ and 50 at 75 m height (above the canopy layer), indicating the inertial range (Fig. 16a and b). The normalized energy spectrum decays with roughly $f S \propto f^{-\frac{2}{3}}$ following Kolmogorov's theory. At high frequencies, spectra of the PALM measurements rapidly decay, which is related to numerical dissipation. This decay is a typical behaviour of LES models using high-order differencing schemes (e.g. Glendening and Haack, 2001; Kitamura and Nishizawa, 2019).

Figure 15. Profiles of mean horizontal wind speed U_{hor}, wind direction d, and wind components u and v as well as turbulence intensity I, skewness γ, excess kurtosis β, and length scale L of both wind velocity components u and v at measurement station 4. Error bars denote the standard deviation of the respective quantity. Note that $z = 0$ denotes street-level height.

At rooftop height (Fig. 16c and d), PALM's spectra are shifted towards higher frequencies compared to those of the wind tunnel at the same height. This shift indicates that PALM simulates smaller-scale turbulence at these heights. The shift can be related to higher roughness and further fosters the abovementioned findings from the profile analysis. The stepwise representation of the buildings introduces additional roughness causing smaller turbulence elements and, hence, a shift of the energy spectrum to higher frequencies. Station 4 shows a more pronounced shift than station 11,

which might, however, be related to the more distinct maximum and, hence, better visibility of a shift at station 4.

The spectra agree better between PALM and the wind-tunnel measurements close to the surface. However, the wind-tunnel measurements did not cover the inertial range at 3 m height because of the limitation of the measurement frequency and small turbulent structures near the surface. PALM does not resolve the inertial range at this height as well because the turbulence elements are smaller than the grid size of 1 m; hence, the small-scale turbulence cannot be directly simulated. Comparing the measured spectra to the
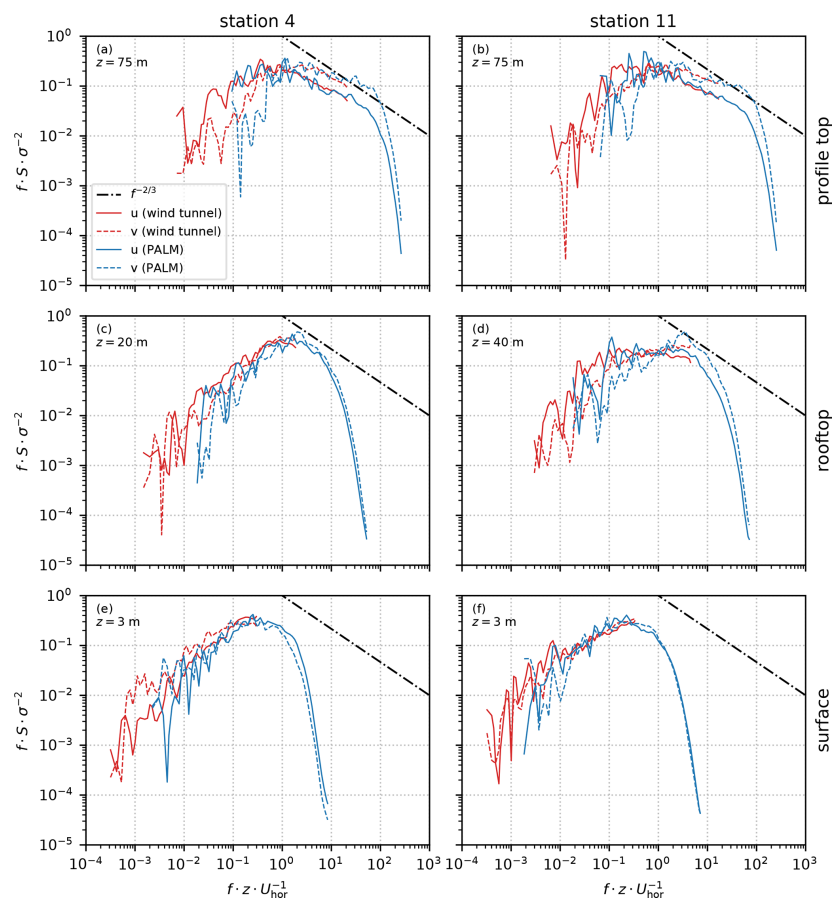
Figure 16. Spectral energy density S for u and v at station 4 **(a, c, e)** and station 11 **(b, d, f)** at profile top **(a, b)**, rooftop height **(c, d)**, and near the surface **(e, f)**. S is normalized by multiplying by the frequency f and dividing by the variance σ^2. For reference, the dash-dotted line shows a slope $f^{-\frac{2}{3}}$ indicating the slope of energy decay according to Kolmogorov's theory. Note that z is given relative to street-level height.

theoretical decay of $f^{-\frac{2}{3}}$, the inertial range is indeed hardly represented within the data.

4   Conclusions

In this study, we analysed PALM's capability to simulate a complex flow field within a realistic urban building array. We compared simulation results to measurements done at the EWTL facility at the University of Hamburg, Germany. The aim was to evaluate the dynamic core of the newest version of PALM, which underwent significant code changes in recent model development.

The comparison of PALM results with the wind-tunnel data demonstrated that PALM is capable of accurately simulating a neutrally stratified urban boundary layer produced by a realistic, complex building array. We compared measurements from the simulation to those of the wind-tunnel ex-

periment at several positions throughout the building array. These positions included non-obstructed locations, windward and leeward sides of buildings, street canyons, and roadway intersections. Overall, the PALM results displayed relatively good agreement with the corresponding wind-tunnel measurements in regards to wind speed and direction as well as turbulence intensity. Validation metrics proposed by Schatzmann et al. (2010) were all within the acceptable ranges.

However, PALM underestimates wind speed and overestimates turbulence close to the ground and building surfaces. Estimates differed most in the span-wise wind velocity component. Paas et al. (2020) recently reported such discrepancies when comparing PALM simulations to real-world measurements. These differences partly occur due to an overestimation of roughness mainly introduced by the stepwise representation of buildings onto PALM's rectilinear grid. This

representation causes building walls not aligned with the grid to appear significantly rougher, resulting in lower wind speed and higher turbulence close to walls, especially in the vicinity of building corners. Also, the used roughness length of $z_0 = 0.01$ m might be larger than the actual surface roughness in the wind-tunnel experiment, causing the highest difference of mean wind speed (9 %) at the lowest analysis height.

To a lesser degree, the mismatch in measurement height is responsible for a difference in mean wind speed. Due to PALM's staggered Arakawa C-grid, output was not available at the exact same position as in the wind-tunnel experiment but shifted half a grid spacing (0.5 m) downwards. This half-grid shift accounted for up to 3 % difference in wind speed at the lowest grid level.

If z_0 is unknown, this can certainly produce differences between PALM and reference data close to surfaces. More importantly, however, is a good representation of building structures. If the focus lies on flow features in close vicinity to buildings, the most important buildings should align with the simulation grid. Also, we recommend a high grid resolution to represent structures as close to the reference as possible. To achieve this, future validations could utilize PALM's nesting feature in order to cope with increasing computational demand of reduced grid size (Hellsten et al., 2020). A higher resolution also reduces the errors introduced by shifting locations of measurements of PALM when comparing against reference data. These errors can otherwise cause deviations close to buildings, where large gradients can cause significant differences in results (see, e.g. the profiles of station 11; Fig. 14). In a future release of PALM, an immersed boundary condition will be available (e.g. Mittal and Iaccarino, 2005). This new boundary condition will mitigate the increased roughness effect introduced by the stepwise representation of building walls not aligned with the rectilinear grid.

Lastly, we provide some general advice for the setup preparation. In the present study, we experienced that input data must always be checked very carefully, especially large building data sets. These building setups might contain errors and false building heights or missing and/or displaced buildings, which are more difficult to spot than in setups with a limited number of buildings. This is, of course, of utmost importance for the area of interest. However, the upwind region also requires proper verification because it directly affects the analysis area. Additionally, when comparing with other experiments, like real-world or wind-tunnel measurements, the positioning of the measurements must be thoroughly checked, as mentioned by Paas et al. (2020). This is true for positioning virtual measurements within the PALM domain as well. At positions with complex wind fields, it can make a large difference for the results if measurement positions are off by only a single grid point. This of course depends on the grid spacing and will be most relevant when using relatively coarse grids.

This study focused on only a single, but the most essential, component of PALM, the dynamic core. However, a full validation of the entire model requires additional studies focusing on the other model components like the radiation module, the chemistry module, or the land surface module. Some of these are already validated (Resler et al., 2017; Kurppa et al., 2019; Fröhlich and Matzarakis, 2020; Gehrke et al., 2020). Others will follow in future publications.

Author contributions. BL and KS created the wind-tunnel setup. KS conducted the wind-tunnel measurements and analysis with supervision of FH and BL. TG, SR, and BM created the simulation setup. TG carried out the simulations and precursor test simulations with the supervision of SR. All authors took part in data analysis of the comparison. TG compiled the manuscript with contributions by all coauthors.

3332   **T. Gronemeier et al.: PALM model evaluation – LES and wind-tunnel experiments**

References

Arakawa, A. and Lamb, V. R.: Computational Design of the Basic Dynamical Processes of the UCLA General Circulation Model, in: General Circulation Models of the Atmosphere, vol. 17, edited by: Chang, J., Methods in computational Physics, 173–265, 1977.

Basu, S. and Lacser, A.: A Cautionary Note on the Use of Monin–Obukhov Similarity Theory in Very High-Resolution Large-Eddy Simulations, Bound.-Lay. Meteorol., 163, 351–355, https://doi.org/10.1007/s10546-016-0225-y, 2017.

Blocken, B., Carmeliet, J., and Stathopoulos, T.: CFD Evaluation of Wind Speed Conditions in Passages between Parallel Buildings – Effect of Wall-Function Roughness Modifications for the Atmospheric Boundary Layer Flow, J. Wind Eng. Ind. Aerod., 95, 941–962, https://doi.org/10.1016/j.jweia.2007.01.013, 2007.

Briscolini, M. and Santangelo, P.: Development of the Mask Method for Incompressible Unsteady Flows, J. Comp. Phys., 84, 57–75, https://doi.org/10.1016/0021-9991(89)90181-2, 1989.

Fröhlich, D. and Matzarakis, A.: Calculating human thermal comfort and thermal stress in the PALM model system 6.0, Geosci. Model Dev., 13, 3055–3065, https://doi.org/10.5194/gmd-13-3055-2020, 2020.

Gehrke, K. F., Sühring, M., and Maronga, B.: Modeling of land-surface interactions in the PALM model system 6.0: Land surface model description, first evaluation, and sensitivity to model parameters, Geosci. Model Dev. Discuss. [preprint], https://doi.org/10.5194/gmd-2020-197, in review, 2020.

Glendening, J. W. and Haack, T.: Influence Of Advection Differencing Error Upon Large-Eddy Simulation Accuracy, Bound.-Lay. Meteorol., 98, 127–153, https://doi.org/10.1023/A:1018734205850, 2001.

Gronemeier, T. and Sühring, M.: On the Effects of Lateral Openings on Courtyard Ventilation and Pollution – A Large-Eddy Simulation Study, Atmosphere, 10, 63, https://doi.org/10.3390/atmos10020063, 2019.

Gronemeier, T., Surm, K., Harms, F., Leitl, B., Maronga, B., and Raasch, S.: Dataset: Evaluation of the Dynamic Core of the PALM Model System 6.0 in a Neutrally Stratified Urban Environment: Simulation Input Data and Measurement Data, Leibniz Universität Hannover, https://doi.org/10.25835/0015082, 2020a.

Gronemeier, T. et al.: Dataset: PALM 6.0 r3921, Leibniz Universität Hannover, https://doi.org/10.25835/0046914, 2020b.

Hanna, S. R., Hansen, O. R., and Dharmavaram, S.: FLACS CFD Air Quality Model Performance Evaluation with Kit Fox, MUST, Prairie Grass, and EMU Observations, Atmos. Environ., 38, 4675–4687, https://doi.org/10.1016/j.atmosenv.2004.05.041, 2004.

Harlow, F. H. and Welch, J. E.: Numerical Calculation of Time-Dependent Viscous Incompressible Flow of Fluid with Free Surface, Phys. Fluids, 8, 2182, https://doi.org/10.1063/1.1761178, 1965.

Hellsten, A., Ketelsen, K., Sühring, M., Auvinen, M., Maronga, B., Knigge, C., Barmpas, F., Tsegas, G., Moussiopoulos, N., and Raasch, S.: A Nested Multi-Scale System Implemented in the Large-Eddy Simulation Model PALM model system 6.0, Geosci. Model Dev. Discuss. [preprint], https://doi.org/10.5194/gmd-2020-222, in review, 2020.

Hertwig, D., Patnaik, G., and Leitl, B.: LES Validation of Urban Flow, Part I: Flow Statistics and Frequency Distributions, Environ. Fluid Mech., 17, 521–550, https://doi.org/10.1007/s10652-016-9507-7, 2017.

Kanda, M., Inagaki, A., Miyamoto, T., Gryschka, M., and Raasch, S.: A New Aerodynamic Parametrization for Real Urban Surfaces, Bound.-Lay. Meteorol., 148, 357–377, https://doi.org/10.1007/s10546-013-9818-x, 2013.

Kitamura, Y. and Nishizawa, S.: Estimation of Energy Dissipation Caused by Odd Order Difference Schemes for an Unstable Planetary Boundary Layer, Atmos. Sci. Lett., 20, e905, https://doi.org/10.1002/asl.905, 2019.

Kurppa, M., Hellsten, A., Auvinen, M., Raasch, S., Vesala, T., and Järvi, L.: Ventilation and Air Quality in City Blocks Using Large-Eddy Simulation – Urban Planning Perspective, Atmosphere, 9, 65, https://doi.org/10.3390/atmos9020065, 2018.

Kurppa, M., Hellsten, A., Roldin, P., Kokkola, H., Tonttila, J., Auvinen, M., Kent, C., Kumar, P., Maronga, B., and Järvi, L.: Implementation of the sectional aerosol module SALSA2.0 into the PALM model system 6.0: model development and first evaluation, Geosci. Model Dev., 12, 1403–1422, https://doi.org/10.5194/gmd-12-1403-2019, 2019.

Leitl, B. and Schatzmann, M.: Validation Data for Urban Flow and Dispersion Models – Are Wind Tunnel Data Qualified?, in: Fifth International Symposium on Computational Wind Engineering (CWE2010), Chapel Hill, North Carolina, USA, 23–27 May 2010, p. 8, 2010.

Letzel, M. O., Krane, M., and Raasch, S.: High Resolution Urban Large-Eddy Simulation Studies from Street Canyon to Neighbourhood Scale, Atmos. Environ., 42, 8770–8784, https://doi.org/10.1016/j.atmosenv.2008.08.001, 2008.

Letzel, M. O., Helmke, C., Ng, E., An, X., Lai, A., and Raasch, S.: LES Case Study on Pedestrian Level Ventilation in Two Neighbourhoods in Hong Kong, Meteorol. Z., 21, 575–589, https://doi.org/10.1127/0941-2948/2012/0356, 2012.

Li, S., Jaroszynski, S., Pearse, S., Orf, L., and Clyne, J.: VAPOR: A Visualization Package Tailored to Analyze Simulation Data in Earth System Science, Atmosphere, 10, 488, https://doi.org/10.3390/atmos10090488, 2019.

Maronga, B., Gryschka, M., Heinze, R., Hoffmann, F., Kanani-Sühring, F., Keck, M., Ketelsen, K., Letzel, M. O., Sühring, M., and Raasch, S.: The Parallelized Large-Eddy Simulation Model (PALM) version 4.0 for atmospheric and oceanic flows: model formulation, recent developments, and future perspectives, Geosci. Model Dev., 8, 2515–2551, https://doi.org/10.5194/gmd-8-2515-2015, 2015.

Maronga, B., Gross, G., Raasch, S., Banzhaf, S., Forkel, R., Heldens, W., Kanani-Sühring, F., Matzarakis, A., Mauder, M., Pavlik, D., Pfafferott, J., Schubert, S., Seckmeyer, G., Sieker, H., and Winderlich, K.: Development of a New Urban Climate Model Based on the Model PALM – Project Overview,

Planned Work, and First Achievements, Meteorol. Z., 28, 105–119, https://doi.org/10.1127/metz/2019/0909, 2019.

Maronga, B., Banzhaf, S., Burmeister, C., Esch, T., Forkel, R., Fröhlich, D., Fuka, V., Gehrke, K. F., Geletič, J., Giersch, S., Gronemeier, T., Groß, G., Heldens, W., Hellsten, A., Hoffmann, F., Inagaki, A., Kadasch, E., Kanani-Sühring, F., Ketelsen, K., Khan, B. A., Knigge, C., Knoop, H., Krč, P., Kurppa, M., Maamari, H., Matzarakis, A., Mauder, M., Pallasch, M., Pavlik, D., Pfafferott, J., Resler, J., Rissmann, S., Russo, E., Salim, M., Schrempf, M., Schwenkel, J., Seckmeyer, G., Schubert, S., Sühring, M., von Tils, R., Vollmer, L., Ward, S., Witha, B., Wurps, H., Zeidler, J., and Raasch, S.: Overview of the PALM model system 6.0, Geosci. Model Dev., 13, 1335–1372, https://doi.org/10.5194/gmd-13-1335-2020, 2020a.

Maronga, B., Knigge, C., and Raasch, S.: An Improved Surface Boundary Condition for Large-Eddy Simulations Based on Monin-Obukhov Similarity Theory: Evaluation and Consequences for Grid Convergence in Neutral and Stable Conditions, Bound.-Lay. Meteorol., 174, 297–325, https://doi.org/10.1007/s10546-019-00485-w, 2020b.

Mittal, R. and Iaccarino, G.: Immersed Boundary Methods, Annu. Rev. Fluid Mech., 37, 239–261, https://doi.org/10.1146/annurev.fluid.37.061903.175743, 2005.

Munters, W., Meneveau, C., and Meyers, J.: Shifted Periodic Boundary Conditions for Simulations of Wall-Bounded Turbulent Flows, Phys. Fluid., 28, 025112, https://doi.org/10.1063/1.4941912, 2016.

Paas, B., Zimmermann, T., and Klemm, O.: Analysis of a Turbulent Wind Field in a Street Canyon: Good Agreement between LES Model Results and Data from a Mobile Platform, Meteorol. Z., 30, 93256, https://doi.org/10.1127/metz/2020/1006, 2020.

Park, S.-B., Baik, J.-J., Raasch, S., and Letzel, M. O.: A Large-Eddy Simulation Study of Thermal Effects on Turbulent Flow and Dispersion in and above a Street Canyon, J. Appl. Meteor. Climatol., 51, 829–841, https://doi.org/10.1175/JAMC-D-11-0180.1, 2012.

Park, S.-B., Baik, J.-J., and Lee, S.-H.: Impacts of Mesoscale Wind on Turbulent Flow and Ventilation in a Densely Built-up Urban Area, J. Appl. Meteor. Climatol., 54, 811–824, https://doi.org/10.1175/JAMC-D-14-0044.1, 2015.

Razak, A. A., Hagishima, A., Ikegaya, N., and Tanimoto, J.: Analysis of Airflow over Building Arrays for Assessment of Urban Wind Environment, Build. Environ., 59, 56–65, https://doi.org/10.1016/j.buildenv.2012.08.007, 2013.

Resler, J., Krč, P., Belda, M., Juruš, P., Benešová, N., Lopata, J., Vlček, O., Damašková, D., Eben, K., Derbek, P., Maronga, B., and Kanani-Sühring, F.: PALM-USM v1.0: A new urban surface model integrated into the PALM large-eddy simulation model, Geosci. Model Dev., 10, 3635–3659, https://doi.org/10.5194/gmd-10-3635-2017, 2017.

Schatzmann, M., Olesen, H., and Franke, J. (Eds.): COST 732 Model Evaluation Case Studies: Approach and Results, University of Hamburg, Hamburg, Germany, 2010.

Scherer, D., Antretter, F., Bender, S., Cortekar, J., Emeis, S., Fehrenbach, U., Gross, G., Halbig, G., Hasse, J., Maronga, B., Raasch, S., and Scherber, K.: Urban Climate Under Change [UC]2 – A National Research Programme for Developing a Building-Resolving Atmospheric Model for Entire City Regions, Meteorol. Z., 28, 95–104, https://doi.org/10.1127/metz/2019/0913, 2019.

VDI: Environmental Meteorology – Prognostic Microscale Wind-field Models – Evaluation for Flow around Buildings and Obstacles, Tech. Rep. VDI 3783 Part 9, VDI/DIN-Kommission Reinhaltung der Luft (KRdL) – Normenausschuss, 2005.

Wang, W. and Ng, E.: Air Ventilation Assessment under Unstable Atmospheric Stratification – A Comparative Study for Hong Kong, Build. Environ., 130, 1–13, https://doi.org/10.1016/j.buildenv.2017.12.018, 2018.

Wicker, L. J. and Skamarock, W. C.: Time-Splitting Methods for Elastic Models Using Forward Time Schemes, Mon. Weather Rev., 130, 2088–2097, 2002.

Williamson, J.: Low-Storage Runge-Kutta Schemes, J. Comput. Phys., 35, 48–56, https://doi.org/10.1016/0021-9991(80)90033-9, 1980.

4 On the Effects of Lateral Openings on Courtyard Ventilation and Pollution – A Large-Eddy Simulation Study

4.1 Declaration of Contributions

T. Gronemeier and M. Sühring contributed equally to the conceptualization, methodology, software, formal analysis and visualization of the study as well as writing the manuscript. M. Sühring administrated the project and T. Gronemeier conducted the simulations. Comments of two anonymous referees helped to improve the final version of the manuscript.

4.2 Research Article

atmosphere

MDPI

On the Effects of Lateral Openings on Courtyard Ventilation and Pollution—A Large-Eddy Simulation Study

Tobias Gronemeier *,† and **Matthias Sühring** †

Institute of Meteorology and Climatology, Leibniz University Hannover, 30419 Hannover, Germany;
suehring@muk.uni-hannover.de

* Correspondence: gronemeier@muk.uni-hannover.de; Tel.: +49-511-762-3232

† These authors contributed equally to this work.

check for updates

Abstract: Courtyards are an omnipresent feature within the urban environment. Residents often use courtyards as recreation areas, which makes them crucial for the physical and psychological comfort of the urban population. However, considering that courtyards represent enclosed cavities, they are often poorly ventilated spaces and pollutants from neighboring traffic, once entrained, can pose a serious threat to human health. Here, we studied the effects of lateral openings on courtyard pollution and ventilation. Therefore, we performed a set of large-eddy simulations for idealized urban environments with different courtyard configurations. While pollutant concentration and ventilation are barely modified by lateral openings for wide courtyards, lateral openings have a significant effect on the mean concentration, the number of high-concentration events and the ventilation within narrower and deeper courtyards. The impacts of lateral openings on air quality within courtyards strongly depend on their orientation with respect to the flow direction, as well as on the upstream flow conditions and upstream building configuration. We show that lateral openings, in most cases, have a negative impact on air quality; nevertheless, we also present configurations where lateral openings positively impact the air quality within courtyards. These outcomes may certainly contribute to improve future urban planning in terms of health protection.

1. Introduction

Courtyards are an essential part of the urban environment. They serve as recreation areas for the local population and therefore play an important role for physical and psychological well-being in residential areas [1]. Courtyards are, however, often poorly ventilated spaces [2], where contaminants can pose a serious threat to human health once they are inside the courtyard cavity; with sources of contaminants could be external, such as from traffic on the nearby streets, or local, such as from domestic fuel [3] or from car parks within the courtyard. Beside the pollutant concentration also the time humans are exposed to the pollutants are critical factors that need to be considered in terms of human health protection [4,5]. For a street canyon, Lo and Ngan [6] showed that a significant amount of pollutants resides within the canyon for a longer time period (e.g., >10 min). Compared to street canyons, however, courtyards might be even worse ventilated since they have typically fewer exits. Hence, once pollutants are entrained into courtyards, they may reside within the courtyard for even longer compared to a street canyon. To design and improve urban planning in terms of health protection, it is, therefore, crucial to understand how contaminants are mixed into and out of the courtyards and for how long they reside within the courtyard cavities.

Although several studies have already described ventilation and pollutant removal from courtyards, e.g., [2,7–11], only a few address the influence of openings on courtyard ventilation. Courtyard ventilation itself largely depends on building configuration, e.g., aspect ratio and building height [2], wind speed [9], wind direction [10], stratification [2,8], as well as blocking obstacles within the courtyard itself [2]. Based on wind-tunnel experiments, Hall et al. [2] revealed that also tunnel-like lateral openings can significantly affect courtyard ventilation. They analyzed removal of pollutants released within the courtyards and showed that lateral openings can either increase or decrease the concentration compared to a closed courtyard, depending on the orientation of the opening with respect to the wind direction. They attributed this to the re-circulation within the courtyard cavity, which can be perturbed but also reinforced by cross flows induced by the opening, worsening or improving courtyard ventilation, respectively. However, in their experiments, Hall et al. [2] considered only undisturbed oncoming flow reaching the building block, which is largely different to a complex flow within an urban environment where neighboring buildings can significantly modify the flow field, e.g., [12,13]. Also, pollutants were only emitted within the courtyard cavity, leaving open the question of how much courtyard cavities are polluted from sources outside, e.g., from the adjacent street canyons?

Using large-eddy simulation (LES), Kurppa et al. [14] studied the effect of different city-block designs on pollutant dispersion. Although pollution within courtyards was only low compared to the adjacent street canyons, different concentrations were observed between the different building setups that partly included also gaps within the building blocks. By means of wind-tunnel experiments Ok et al. [7] showed that lateral openings can strongly affect the wind speed within the courtyards. The lowest wind speeds were observed within closed courtyards, while the highest were observed when multiple openings are aligned along the mean wind direction. Openings orientated perpendicularly to the main flow direction increased wind speeds less compared to other opening setups. Even though Ok et al. [7] did not investigate pollutant dispersion, their results indicate that lateral openings can significantly affect courtyard ventilation, which in turn might possibly also affect the air quality within courtyards.

The impact of pollutants on human health depends, among other aspects, largely on the concentration, e.g., [15]. Within busy street canyons, concentration levels can reach high values. In the absence of lateral building openings, significantly lower concentrations can be observed in the rear of the buildings [16] and adjacent backyards [8]. Before polluted air can reach these areas, it first needs to exit the street canyon via the roof level, where it is mixed with fresh air from above, leading to significantly lower pollutant concentrations. However, this might become different when lateral openings are present, where high pollutant concentrations can be directly mixed into the courtyards.

Here, motivated by the findings of previous studies, we ask:

- What is the effect of lateral openings on courtyard pollution and ventilation within an urban environment?
- How do lateral openings affect maximum concentrations and residence time scales within courtyards?

To answer these questions, we used LES datasets for idealized building arrays to investigate pollutant dispersion into courtyards. Pollutant sources are considered outside of the courtyard cavity resembling e.g., car exhausts from streets. We considered different building configurations, i.e., different aspect ratios, and different orientation of lateral tunnel-like openings with respect to the mean wind. Although observations already revealed that stratification also significantly influences pollutant dispersion in urban environments [8], we exclusively concentrate on neutral conditions within this first study.

Section 2 describes the LES model, the simulation setups as well as the applied analysis techniques followed by validation results of the LES model against wind-tunnel data. Section 3 gives a description of the mean flow field and concentration distribution and shows results on the net transport of scalar

through the openings as well as the analysis of high-concentration events and residence times. Finally, Section 4 gives a summary and closes with ideas for future studies.

2. Methods

2.1. LES Model and Numerical Experiments

For the numerical simulations in our study, we used the LES model PALM [17], revision 2705. PALM has been already successfully used to simulate the flow in urban environments in high detail, e.g., [14,18–22]. Also, PALM provides the possibility to represent three-dimensional building topologies and includes an embedded Lagrangian particle model, making it well-suited to study pollutant dispersion and ventilation in urban environments. PALM solves the non-hydrostatic incompressible Boussinesq equations. For the subgrid model, the kinetic energy scheme of Deardorff [23] was used. The advection terms were discretized by a fifth-order scheme [24], while near solid walls the order of the scheme was successively degraded. For the time discretization a third-order Runge-Kutta scheme by Williamson [25] was used.

The model domain consists of several building patches that are aligned and shifted in rows as depicted in Figure 1. A single patch consists of a building containing a courtyard and an adjacent street at its southern and western wall. To study effects of different building/courtyard geometries on courtyard ventilation, we performed three simulations with different courtyard aspect ratio (AR, ratio of building height, or courtyard depth, H, to courtyard width W), which are listed in Table 1. The case with $AR = 1$, where $H = W$, as well as the cases with high and low AR are hereafter referred to as "AR1", "AR3" and "AR03", respectively. The case AR1 was chosen to link to other studies as this is the most famous case throughout other research, e.g., [2,7,9,10]. The other two cases, AR03 and AR3, were chosen as they showed the most pronounced differences in scalar concentrations compared to the AR1 case within the study by Hall et al. [2]. The building within a patch has a single lateral opening either on its western, eastern, northern or southern wall, or has no opening at all, i.e., it is closed. These patches are labelled as "W", "E", "N", "S", and "C", respectively. The lateral opening has a size of 4 m by 4 m and is always located at the bottom center of the respective building wall to represent an entrance to the courtyard. The size of the opening is chosen according to our personal experience, assumed to be typical for mid-European city quarters, even though we note that openings vary in size in real cities, depending on the prevailing architecture. Also, different sized openings at other locations of a building wall might also appear within a real city. However, in this idealized study, we tried to keep the setup simple, to limit the number of effects and hence the complexity of the results.

Table 1. Courtyard aspect ratio (AR) and domain size of the three simulated cases. H indicates the building height (or courtyard depth) and W indicates the courtyard width.

Case	AR	H (m)	W (m)	Domain Size ($x \times y \times z$) (m)
AR1	1	20	20	$480 \times 400 \times 531$
AR3	3	60	20	$480 \times 400 \times 531$
AR03	0.3	20	60	$480 \times 600 \times 531$

A row of buildings is then formed by aligning five building patches, with each patch along the y-direction having a different courtyard/opening configuration (see Figure 1). The street width was set to 20 m for all streets and the building-wall thickness was set to 20 m for all buildings in all simulated cases.

For cases AR1 and AR3, the domain consists of six rows, while three neighboring rows are shifted along the y-direction, forming a front, center and back row with respect to the x-parallel flow from the West (see Figure 1b). For case AR03, the center rows are missing resulting in only four rows within the domain (see Figure 1c). This was done to keep the length of the x-parallel (wind-parallel) streets constant throughout the different cases (compare Figure 1b,c). This ensures that in all simulated setups

the flow can accelerate the same distance and has the same input of scalar (see details below) along the
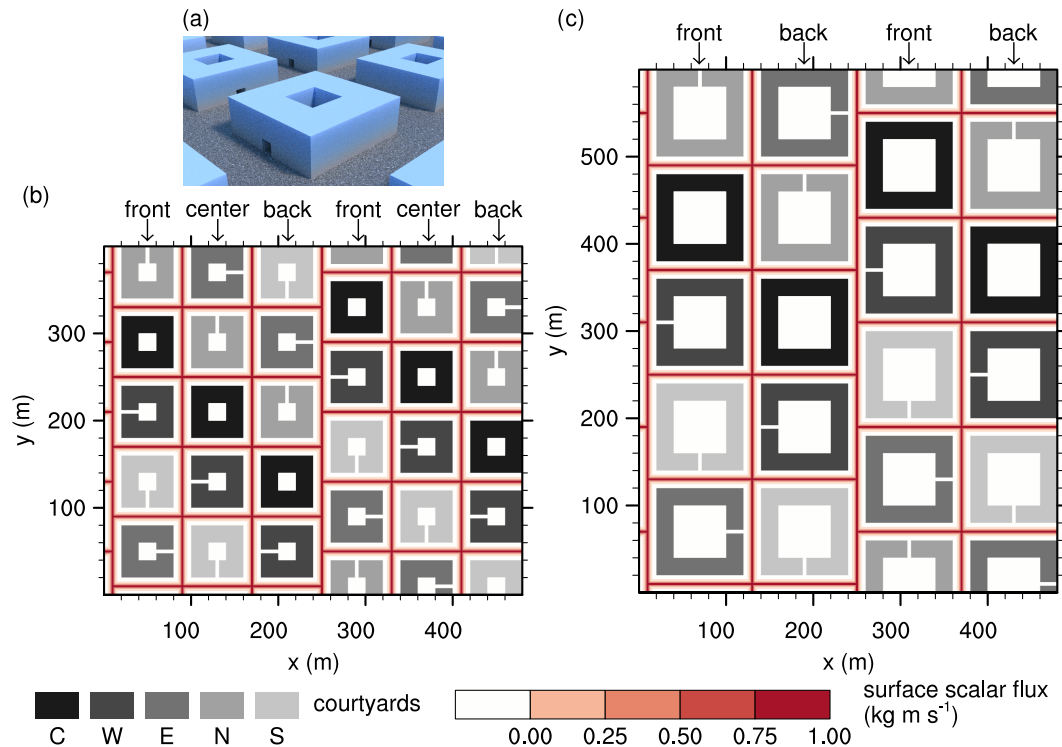*x*-parallel streets.

Figure 1. (**a**) 3D view of the building setup used in case AR1 and (**b**,**c**) horizontal cross-sections of
the simulation domains and building configuration: (**b**) case AR1 and AR3, (**c**) case AR03. Different
shades of *grey* indicate building patches with a different courtyard configuration, labelled according
to their lateral opening orientation. *Red* colors indicate locations and strength of the scalar sources.
The "front", "center" and "back" labelling indicates the front-, center-, and back-building row of the
staggered building patches.

We have chosen this staggered building setup to break-up the street canyons along the *x*-direction,
to prevent artificial jets that would develop along the infinite *x*-parallel street canyons, as we did
observe in preparatory test simulations. Hence, we optimized our setup to prevent such unrealistic
long streets. Furthermore, these setups allow study of different courtyard realizations within a single
simulation, which requires significantly less computational effort compared to study each courtyard
realization in a single simulation individually, which would not be possible without increasing the grid
spacing. To study different courtyard realizations in one simulation, however, requires that the flow
and scalar distribution within the different courtyard cavities are statistically independent from each
other. Indeed, an analysis of velocity and scalar variances within identical courtyards but different
upstream courtyards revealed no significant differences (not shown). Hence, we are confident that the
impact of a lateral opening is limited to the courtyard cavity itself and the part of the street directly
adjacent to the opening. This is only true as long as lateral openings do not directly face each other,
hence, we avoided this configuration in our building layout (see Figure 1).

At this point, we would like to note that the studied building configuration is highly idealized.
In reality, buildings would vary in height and orientation, and courtyard configurations and opening
sizes would be more heterogeneous. However, as we try to focus purely on effects of openings on
courtyard ventilation and pollution, we idealized the building setup to isolate those effects, while still
trying to mimic an urban environment with neighboring buildings.

In total, the domain size adds up to 480 m in the *x*-direction and 400 m (case AR03: 600 m) in the *y*-direction with a domain height of 531 m. A rectilinear grid with an isotropic grid spacing of 0.4 m within the lower 200 m of the domain was used. To save computational costs, the vertical grid spacing (along *z*-direction) above 200 m was stretched by a factor of 1.08 until it reached 4 m at a height of 247 m, from where on it was kept constant up to the domain top. Overall, the domain consisted of 1200 by 1000 by 602 grid cells (case AR03: 1200 by 1500 by 602) in *x*- *y*- and *z*-direction, respectively.

The simulations were initialized with a logarithmic wind profile reported by Hall et al. [2] and driven by a horizontal pressure gradient of -1×10^{-4} Pa m^{-1} along the *x*-direction, resulting in a mean wind speed of (1.9 ± 0.3) m s^{-1} at $z = 2H$ during the analysis period with flow parallel to the *x*-direction, while almost constant wind speed during the analysis period.

At the lateral boundaries, we used cyclic conditions at the spanwise boundaries and shifted cyclic conditions according to Munters et al. [26] at the streamwise boundaries. The shifted cyclic condition was used to prevent the generation of streamwise-elongated coherent structures that can appear if pure cyclic conditions are applied [26]. The shifting distance along the *y*-direction was set to the size of a single building patch, hence, to 80 m in case AR1 and AR3 and 120 m in case AR03. Free-slip boundary conditions were applied at the domain top. As surface boundary condition for the momentum equations (at Earth and building surfaces), Monin–Obukhov similarity theory (MOST) was applied locally between the surface and the first grid point normal to the respective surface orientation. This applies for all surfaces, i.e., at horizontal upward- and downward-facing surfaces (at the top of the lateral opening), as well as at vertical surfaces, following Park et al. [20] and Park et al. [27]. The boundary layer in our simulations is purely shear-driven, i.e., we solved no equation for the temperature or humidity.

To investigate dispersion of pollutants, e.g., from car exhausts, into the courtyards, we considered line sources of passive scalar within the street canyons, as indicated by the *red* lines in Figure 1. These sources emulate a time-constant, Gaussian-shaped surface scalar flux along the center line of the streets. This way, we simulated the pollutant release from traffic within the street canyons which allows us to investigate how such pollutants are transported into the courtyards. Surface fluxes were identical on all streets, i.e., we did not distinguish between main and side streets with different traffic density. Besides directly simulating pollutant sources, also other concepts exist which evaluate the ventilation of the urban environment such as the concept of air delay [28]. The air delay gives an estimate of how long a specific air parcel resides within the urban environment and this way concludes the ventilation. However, the main focus of this study is to evaluate how pollutants are advected from outer sources into the courtyard cavity while lateral openings are considered. Therefore, a direct simulation of scalar sources is superior to indirect measurements.

The total simulation time for all cases was 4 h. This includes 2 h spin-up time and 2 h analysis time.

Presented data were averaged over the analysis period (2 h) as well as over identical courtyards (in a simulation, there are two identical courtyard realizations). Before time-averaging, scalar concentration *s* was normalized by the time-dependent background concentration s_B, which is defined as the domain-averaged concentration at $z = H$. The normalization was done to account for any time dependencies in scalar concentration due to the time-constant scalar flux.

To investigate the relative occurrence of high concentrations within the courtyards and how these depend on the lateral openings, we calculated probability density functions (PDF) for the scalar concentration. Concentrations were sampled at the courtyard center at a height of 1.8 m at each time step during the analysis period. The sampled concentrations were then normalized by s_B.

Finally, in the following, we refer to courtyards with westward lateral opening in the front, center, and back row as "W front", "W center", and "W back", respectively (equivalent for the other opening orientations, see Figure 1).

The used model parameter lists for PALM for all described cases, as well as the additional code parts used for data analysis in this study are included in the Supplementary Materials.

2.2. Balance Term Analysis

To study courtyard pollution in more detail and distinguish between mixing of scalar into the courtyard through the top opening and the lateral opening, we examined the terms of the time-averaged scalar transport equation

$$\frac{\overline{\partial s}}{\partial t} = -\frac{\partial \overline{u_{1,2}\,s}}{\partial x_{1,2}} - \frac{\partial \overline{u_3\,s}}{\partial x_3} - \frac{\partial \overline{\tau_{1,2,s}}}{\partial x_{1,2}} - \frac{\partial \overline{\tau_{3,s}}}{\partial x_3}, \tag{1}$$

where the left-hand side describes the local temporal change of passive scalar s. The first and the second terms on the right-hand side describe the resolved-scale transport of s in horizontal as well as in vertical direction, respectively, with $u_{1,2}$ being the horizontal velocity components and u_3 being the vertical component. The third and fourth terms on the right-hand side are the parametrized turbulent transport on the subgrid scale in horizontal ($\tau_{1,2,s}$) and vertical direction ($\tau_{1,s}$), respectively. The overbar indicates the time-averaging. To be consistent with the numerical discretization, we directly used the flux divergence provided by the advection scheme and the subgrid-scale parametrization. As no sources or sinks of passive scalar exist within the courtyard volume, the entire passive scalar is entrained into the courtyard via the openings, so that we can make use of Gauss's theorem to calculate the net transport. Thus, integrating Equation (1) over the entire courtyard volume leads to the mean net transport of scalar along the respective spatial direction,

$$\int_V \frac{\overline{\partial s}}{\partial t}\,\partial V = \int_V \left(-\frac{\partial \overline{u_{1,2}\,s}}{\partial x_{1,2}} - \frac{\partial \overline{\tau_{1,2,s}}}{\partial x_{1,2}} \right) \partial V + \int_V \left(-\frac{\partial \overline{u_3\,s}}{\partial x_3} - \frac{\partial \overline{\tau_{3,s}}}{\partial x_3} \right) \partial V, \tag{2}$$

with V indicating the entire courtyard volume up to $z = H$. The left-hand side describes the temporal mean accumulation of scalar within the courtyard volume, which is, however, relatively small compared to the terms on the right-hand side. The first term on the right-hand side of Equation (2) gives the net transport of scalar via the lateral opening (T_l), while the second term gives the vertical net transport of scalar via the top opening (T_v). A positive value indicates an increase of passive scalar, while a negative value indicates a decrease of passive scalar. For closed courtyards, the T_l vanishes so that scalar accumulation is only due to the vertical transport.

2.3. Evaluation of Pollutant Residence Times

The impact of pollutants on human health depends, among other factors, on the time humans are exposed to these pollutants [4,5], or, in other words, how long pollutants reside within the courtyard cavity. To estimate the residence times of pollutants within courtyards, we followed Lo and Ngan [6] and used a Lagrangian particle model embedded into the LES model, where the residence time is defined as the time elapsed between the entry of a particle into the region of interest and its exit [29]. Although the Lagrangian particle model requires higher computational resources, it allows us to directly measure the residence time and therefore gives more reliable results than indirect measurements retrieved from scalar concentration values as, e.g., when analyzing the air delay.

The embedded Lagrangian particle model is based on Weil et al. [30], to separate the particle speed into a deterministic and a stochastic contribution, which corresponds to dividing the turbulent flow field into a resolved-scale and a subgrid-scale (SGS) portion, respectively, following the LES philosophy. The resolved-scale velocity is provided by the LES at each time step, while the SGS velocity is predicted by integrating a stochastic differential equation according to Weil et al. [30], who strictly adopted the Thomson [31] model to the subgrid scale by assuming isotropic and Gaussian-distributed turbulence. To parametrize the stochastic particle dispersion on the subgrid scale, the LES provides local values of the SGS turbulent kinetic energy and the dissipation rate at each time step.

According to Steinfeld et al. [32], the LES data are interpolated bi-linearly on the actual particle position in the horizontal. In the vertical, a linear interpolation is used, except for the particles located between the surface and the first grid level, where a logarithmic interpolation according to local MOST

for the resolved-scale horizontal velocity components is applied. At the solid boundaries, i.e., upward-and downward-facing as well as vertical building surfaces, we used a reflection boundary condition for the particles, and cyclic conditions at the lateral boundaries. A more detailed description of the particle model embedded into the LES model is given by Steinfeld et al. [32] and Maronga et al. [17].

Following Lo and Ngan [6], we calculated the residence time of a particle by summing-up the total time the particle spent within the courtyard volume. Once a particle exits the courtyard volume by the lateral or the top opening, the particle age is stored and the particle itself is immediately removed from the simulation. Particles were released within the courtyard each LES time step at a height of 1.8 m. This particle-source height should be representative for human exposure. Setting the particle sources within the courtyard only, has the advantage that fewer particles need to be modelled to obtain sufficient statistics, compared to the case where particle sources are along the street canyons and only a small portion of the particles would be mixed into the courtyards.

Physically, larger residence times indicate less turbulent mixing and ventilation of the courtyard. This in turn indicates larger impact of pollutants on human health in case of high concentrations, compared to smaller residence times [6]. Please note that we focus on residence times only, which is a pure ventilation measure. Following Lo and Ngan [6], however, the exposure time is a more direct measure to relate the impact of pollutants on human health as it also considers re-entrainment of particles into the region of interest, which the residence time does not. However, Lo and Ngan [6] showed that the number of re-entrainment events is relatively small, so that we decided to focus on the residence times, for the sake of simplicity and computational effort.

At this point, we want to note that Lo and Ngan [6] did observe particle accumulation near solid walls in their study (also using PALM) and excluded these regions from their analysis. In preparatory studies, we could observe similar particle accumulation near solid walls. This accumulation could be traced back to an erroneous treatment of SGS particle velocities near solid walls, which was fixed in PALM revision 2418. In the following, we could not observe particle accumulation near solid walls any more.

2.4. Validation and Grid Sensitivity

To prove PALM's capability to correctly represent the flow within a courtyard cavity, we first compare simulation results against data from wind-tunnel experiments by Hall et al. [2] and Reynolds-averaged simulations by Ryu and Baik [9]. The validation setup consists of a single building with a closed courtyard (no lateral opening) and an undisturbed incoming flow according to the wind-tunnel experiments shown by Hall et al. [2]. The building setup (height, width) is similar to a single building of case AR1 with its center placed at $(x, y) = (370\,\text{m}, 144\,\text{m})$. The domain size for this case is 620 m by 288 m by 240 m in the *x*-, *y*-, and *z*-direction, respectively, with an isotropic grid spacing of 0.4 m. The simulation time was 4 h. The complete parameter list of this simulation is included in the Supplementary Materials.

Figure 2 shows profiles of the normalized and time-averaged *u*-component of the wind speed and its standard deviation. Within the courtyard cavity, *u* agrees well with the data from Ryu and Baik [9] and Hall et al. [2], except for the lower half of the courtyard where Hall et al. [2] reported a higher negative *u*-component, indicating a stronger re-circulation within the courtyard cavity. Above the cavity, the simulated *u*-profile agrees fairly well with the observed wind-tunnel data. The variation u' can only be compared with the wind-tunnel measurement of Hall et al. [2] as it was not reported by Ryu and Baik [9]. The simulated u'/u_0 is about 0.1 within the courtyard cavity, while Hall et al. [2] reported larger values of around 0.2 within the cavity. However, other courtyard setups with larger and smaller ARs reported by Hall et al. [2] showed significantly lower values which are in better agreement with our validation case. Since the mean wind profile is in good agreement with the data reported by Hall et al. [2] and Ryu and Baik [9] and u' shows qualitatively good agreement with profiles of Hall et al. [2], we are confident that PALM is capable of correctly simulating the flow inside the courtyard cavity.
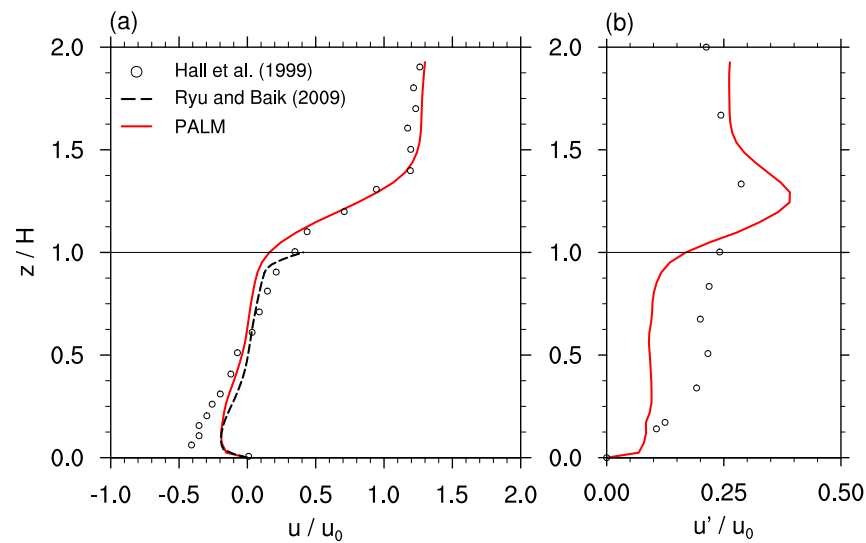
Figure 2. Vertical profiles of normalized (**a**) *u*-component of the wind and (**b**) its standard deviation u' at the center of the courtyard. The red curve shows the profiles simulated by PALM, the black curve the simulated data by Ryu and Baik [9], and the dots data from the wind-tunnel experiments by Hall et al. [2]. u_0 represents the mean oncoming wind speed at $z = H$ (height marked by horizontal line). The PALM profiles are time-averaged over 3 h.

The scalar dispersion simulated by PALM was previously validated by Park et al. [20] via wind-tunnel data for a street-canyon case and is therefore not validated again in the current study.

By definition, the results of an LES with implicit filtering, as used in PALM, depend on the grid spacing [33,34]. In practice, the question is whether the analyzed statistical moments converge towards finer grid spacing. Hence, we performed a grid sensitivity study where we conducted a simulation of a single building patch as described above (domain size: 80 m × 80 m), including a courtyard with an opening in wind direction. Three different grid sizes (1 m, 0.4 m and 0.2 m) were considered and the simulation time was 10 h. Other simulation parameters were identical to the main simulations (a detailed parameter list is included in the Supplementary Materials).

Figure 3a,c show the mean wind speed within the courtyard cavity and along the center line of the opening, respectively. The mean wind speed differs most between the simulation with 1 m and 0.4 m grid spacing, while the differences between 0.4 m and 0.2 m grid spacing are only small. A similar behavior can be observed for the standard deviation u' (Figure 3b,d), even though there are still small differences between 0.4 m and 0.2 m grid spacing. Hence, as a grid spacing of 0.2 m does not yield to significantly different results compared to a grid spacing of 0.4 m but would significantly increase the computational demands, we chose a grid spacing of 0.4 m for all following simulations.
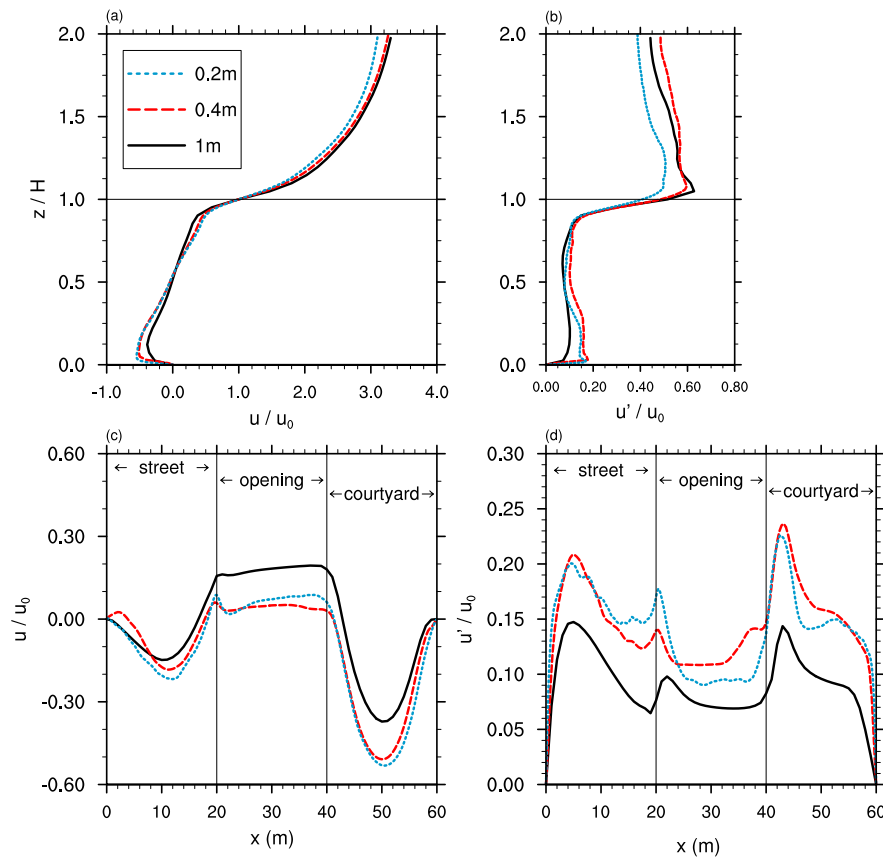
Figure 3. Vertical profiles of normalized (**a**) u-component of the wind and (**b**) its standard deviation u' at the center of the courtyard, as well as horizontal profiles of (**c**) u and (**d**) u' along the center line of the courtyard opening for different grid sizes. u_0 represents the mean oncoming wind speed at $z = H$ (height marked by horizontal line). Profiles are time-averaged over 3 h.

3. Results

3.1. Mean Flow and Scalar Distribution

3.1.1. Case AR1

Figures 4a–c and 5a–c show vertical and horizontal cross-sections, respectively, of the time-averaged flow field and scalar concentration for the closed courtyards in case AR1 (ref. Figure 1 and Table 1 for better orientation). Within the courtyard cavities, well-defined re-circulations are present which extend throughout the entire cavity (Figure 4a–c). Similar well-defined re-circulations can be observed within the street canyons between the buildings (Figure 4b) as well as downstream of the back-building row (Figure 4c), where the strongest re-circulations with the largest horizontal extent into downstream direction can be observed. Furthermore, upstream of "C front" we can observe a small eddy close to the surface, attributed to the non-blocked oncoming flow through the x-parallel street canyon (Figure 4a). All these mentioned flow patterns were already focused on in previous studies and are well documented, e.g., [12,13,35,36]. Furthermore, we refer also to the work of Hall et al. [2] and Ryu and Baik [9], where the flow pattern within closed-courtyard cavities is already well described.

The highest scalar concentrations can be observed within the street canyons (Figure 4). The largest values occur near the surface and the leeward walls of the canyon, according to the observed pattern in previous studies [12,37], as it becomes most obvious downstream of "C back" (Figure 4c), where the re-circulation can catch up more scalar along the x-parallel street canyon compared to the re-circulations

downstream of "C front" or "C center" (compare Figures 4a,b and 6a). Within the closed-courtyard cavities, the concentrations are significantly lower compared to those within the street canyons, with values slightly lower than s_B, while no significant differences can be observed among the front-, center-, and back-row courtyards.
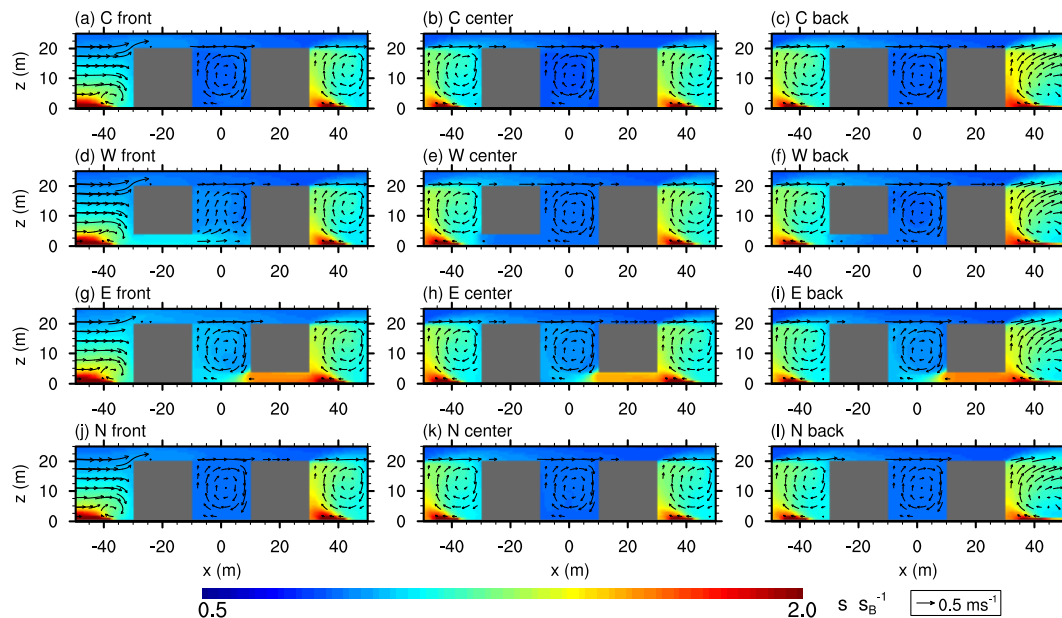

Figure 4. Xz-cross-section of the mean flow field (vector arrows) and mean scalar concentration (contours) at the courtyard center for case AR1. Scalar concentration is normalized with the background concentration s_B at $z = H$. Please note, due to symmetry, courtyards with southern openings show similar scalar distribution and wind field than those with northern openings and are hence not shown.

If lateral openings are present, the flow and concentration patterns within the courtyards change, depending on the flow pattern within the adjacent relevant street canyon. For courtyard "W front", the opening faces the incoming flow from the upstream x-parallel street canyon. It can thus directly enter the courtyard, which leads to a significant input of scalar (see Figure 5d) with highest concentrations near the surface and the lateral opening. Within the "W front" courtyard, the re-circulation is still present but shifted upwards as well as towards the windward building wall (see Figure 4a,d) compared to that in the closed case, while in the lower part of the courtyard also a horizontal re-circulation forms (see Figure 5d). This perturbation of the re-circulation agrees with the findings of Hall et al. [2], who identified a perturbation of the re-circulation within the courtyard due to lateral openings.

For courtyards "W center" and "W back", similar re-circulation patterns can be observed within the street canyon and the courtyard cavity, with low concentrations inside the courtyards. This is attributed to the re-circulation within the street canyon (courtyard) which points away (towards) the opening (see Figure 4e,f) and so prevents entrainment of scalar into the courtyard cavity through the lateral opening.

In contrast, courtyards with an opening on their eastward side ("E front", "E center", and "E back") show a significantly higher scalar concentration (Figure 5g–i). In these cases, the circulation within the street canyons transports the polluted air towards the courtyard cavity (cf. Figure 4g–i), which might be further supported by the circulation inside the courtyard that further distributes the entrained scalar throughout the cavity.
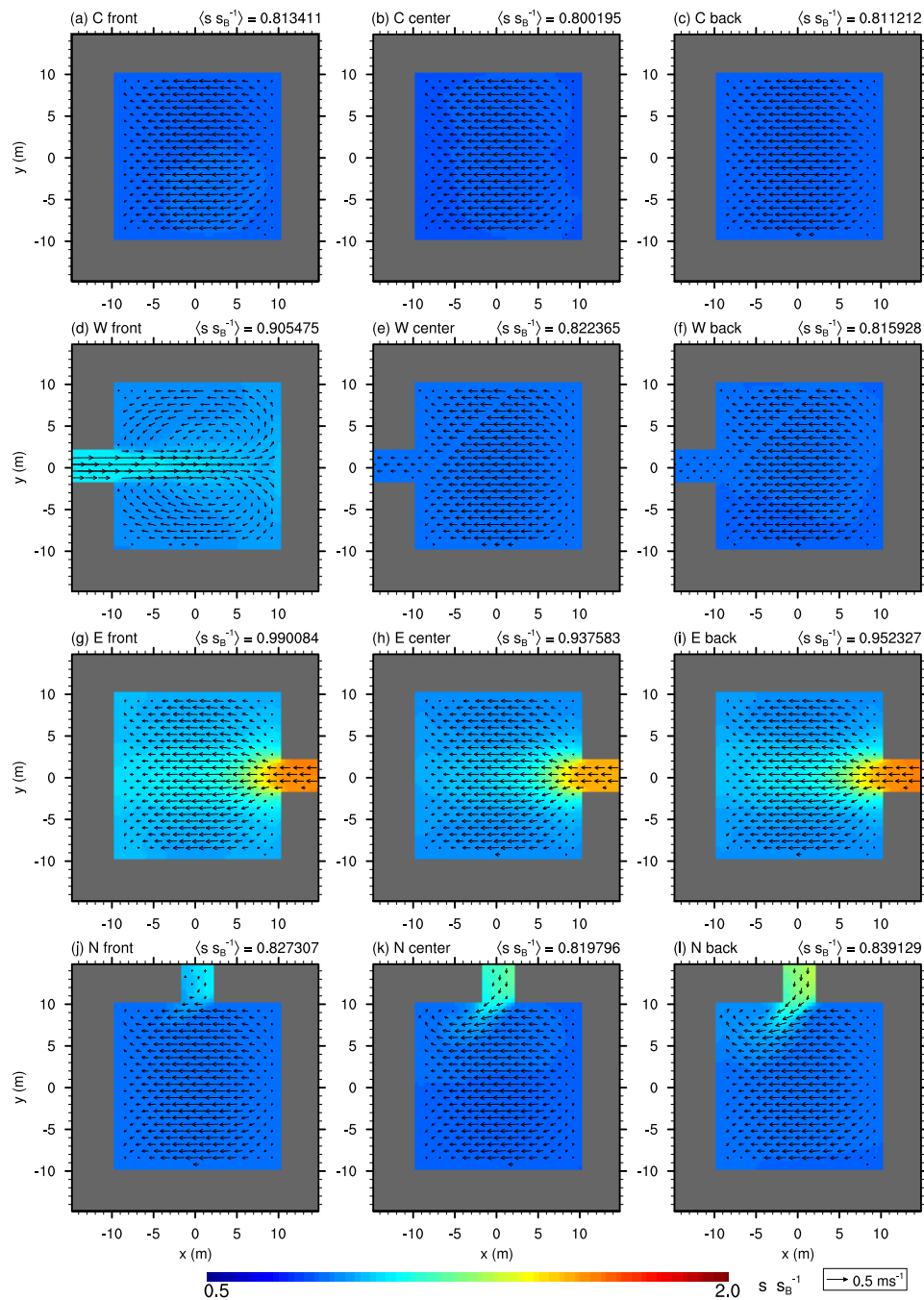
Figure 5. *Xy*-cross-section of the mean flow field (vector arrows) and scalar concentration (contours) within courtyards at $z = 1.8\,\mathrm{m}$ for case AR1. Scalar concentration is normalized with the background concentration s_B at $z = H$. Please note, due to symmetry, courtyards with southern openings show similar scalar distribution and wind field than those with northern openings and are hence not shown.

If the opening is located at the northern wall, the *x*-parallel street-canyon flow slightly pushes polluted air into the courtyard (cf. Figure 5j–l). The strength of this mean inflow as well as the scalar concentration within and near the lateral opening increases from the front row to the back row. However, it does not significantly affect the mean flow pattern within the rest of the courtyard and

the re-circulation is quite similar to that of a closed courtyard (cf. Figure 4j–l). The concentration is about the same or slightly higher within these courtyards compared to the closed ones as well as "W center" and "W back", but it is well below the levels of courtyard "W front" and those with openings at the eastward wall. Please note, due to symmetry, results for courtyards with openings located at the northern wall are similar to those with openings at the southern wall.
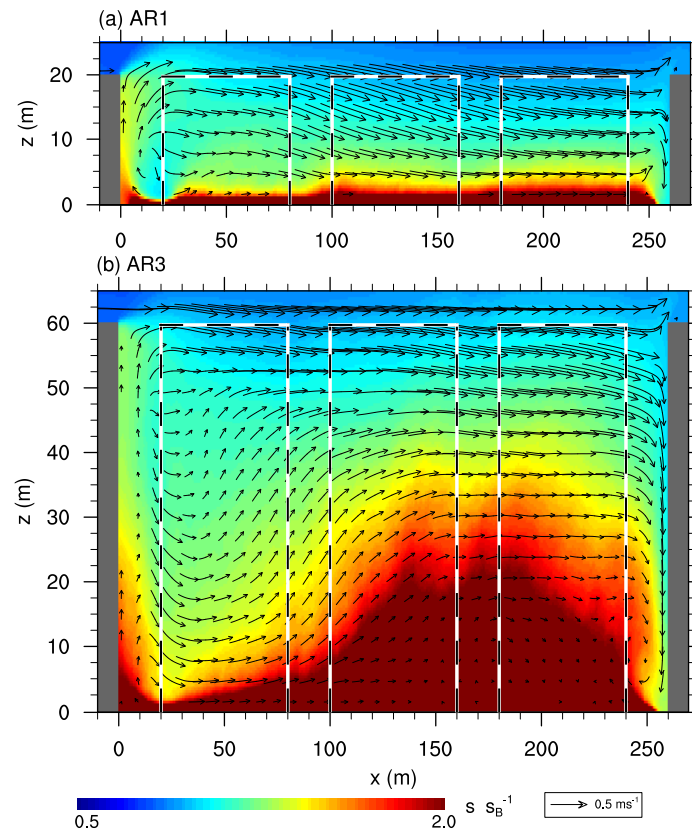

Figure 6. *Xz*-cross-section of the mean flow field (vector arrows) and scalar concentration (contours) along the center of an *x*-parallel street for case (**a**) AR1 and (**b**) AR3. Scalar concentration is normalized with the background concentration s_B at $z = H$. The black-and-white lines indicate the positions of the buildings along the street.

3.1.2. Case AR3

Figure 7 shows vertical cross-sections for the high aspect ratio case AR3, where courtyards as well as the street canyons are three times deeper compared to AR1 (ref. Table 1). The re-circulation within the courtyard cavities does not extent throughout the entire cavity but occurs only within the upper part. Close to the surface, a weak secondary counter-rotating circulation is present, similar to the findings described in, e.g., Hall et al. [2] and Assimakopoulos et al. [12] (see Figure 7a–c). Similar to case AR1, the non-blocked oncoming flow along the *x*-parallel street canyon upstream of the front row causes a small eddy close to the surface at the windward building wall, where also air from the upper part of the street canyon is transported downwards (see Figure 7a). Likewise, downstream of the back row, a re-circulation downstream of the building can be observed. The street-canyon flow between the center and back row shows a comparable pattern as within the courtyard cavity. Between the front- and center-row building (see Figure 7b), it strikes that the street-canyon flow exhibits a vertical component which extends down to the surface, which might be linked to the flow along the *x*-parallel street canyon.
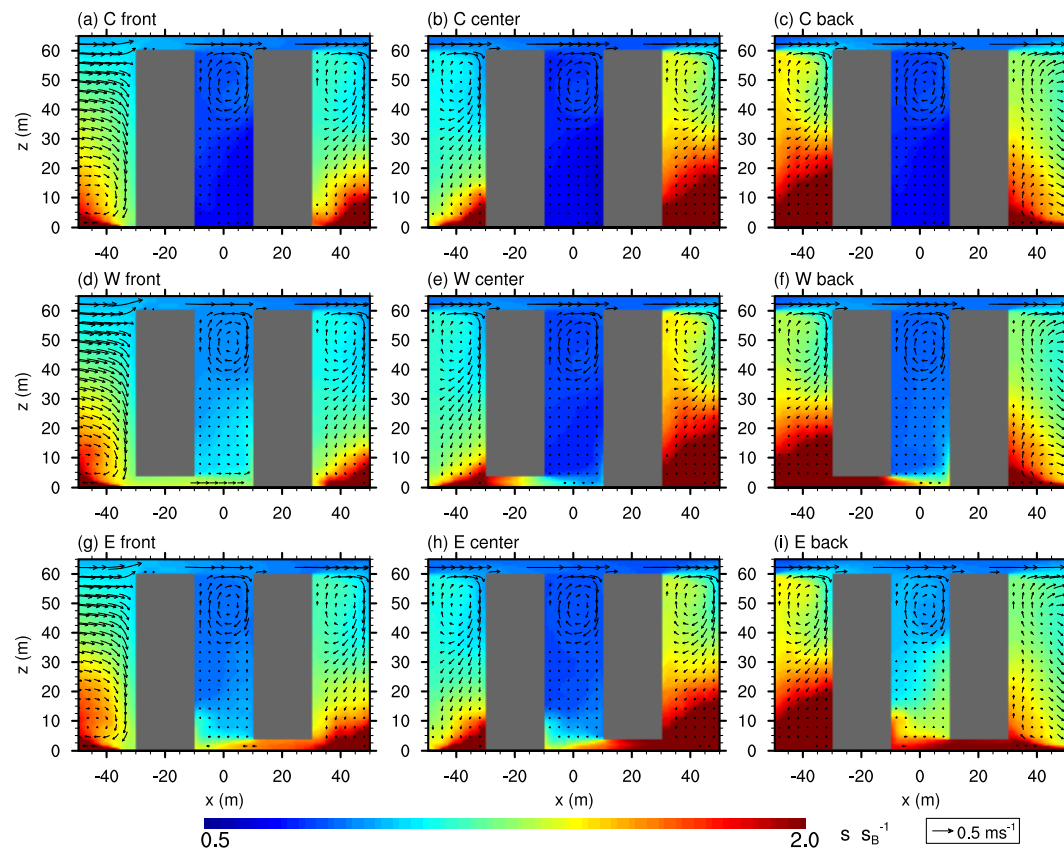
Figure 7. *Xz*-cross-section of the mean flow field (vector arrows) and mean scalar concentration (contours) at the courtyard center for case AR3. Please note, for reasons of space, not all realizations are shown.

The scalar concentration within the closed-courtyard cavities is lowest near the surface with values significantly lower than the background concentration; and highest in the upper part where scalar is vertically mixed into the cavity but not effectively transported downwards. Within the street canyons, the concentration shows significantly higher values compared to the courtyard cavity, while the scalar distribution is quite different for the different canyons. Upstream of the front-row building, the largest values can be observed in the lower part of the canyon further upstream of the street, while directly at the windward building wall, relatively lower concentrations can be observed which correlates with the downward transport of less-polluted air from above near the wall (see Figure 7a,d,g).

Between the front and the center row (Figure 7b) the highest concentrations occur near the surface at the windward building wall, which might be due to the downward component which is strongest near the leeward building wall where it transports fresh air downward (this, however, needs further investigation as it is beyond the scope of this study). Between the center- and back-row, scalar concentration is highest compared to the other street canyons along *y*-direction (see, e.g., Figure 7b,c), which is related to the flow and scalar concentration along the *x*-parallel street as depicted in Figure 6b. Similar to case AR1, the highest concentrations behind the back-row building can be observed at the leeward wall, attributed to the re-circulation (compare, e.g., Figures 4c and 7c).

The differences in the flow field and scalar concentration between the *y*-parallel streets, as indicated by Figure 7, might be also linked to the flow and scalar distribution along the *x*-parallel streets, which is depicted in Figure 6b. Compared to case AR1, the extent of the re-circulation downstream of the back-row building is significantly larger in case AR3, reaching approximately up

to the second y-parallel side street. This also affects the scalar distribution along the x-parallel street canyon, which is more heterogeneous compared to case AR1 (see Figure 6a).

All opened courtyards show an inflow through their lateral opening and hence a higher scalar concentration compared to the closed courtyards, as indicated by Figures 7 and 8. In contrast to the closed courtyards, the highest concentrations can be observed within the lower poorly ventilated parts of the cavities, whereas the better-ventilated upper parts of the cavities exhibit lower concentrations. For "W front", the oncoming flow along the x-parallel street enters the courtyard causing a significant increase of scalar concentration near the courtyard surface (see Figure 8a), similar to case AR1. Caused by the weak street-canyon circulation, "W center" and "W back" show a mean inflow into the courtyard cavity, with lower scalar concentration in case of "W center" attributed to the downward-mixing of less-polluted air from upper parts of the street canyon (Figure 7e).
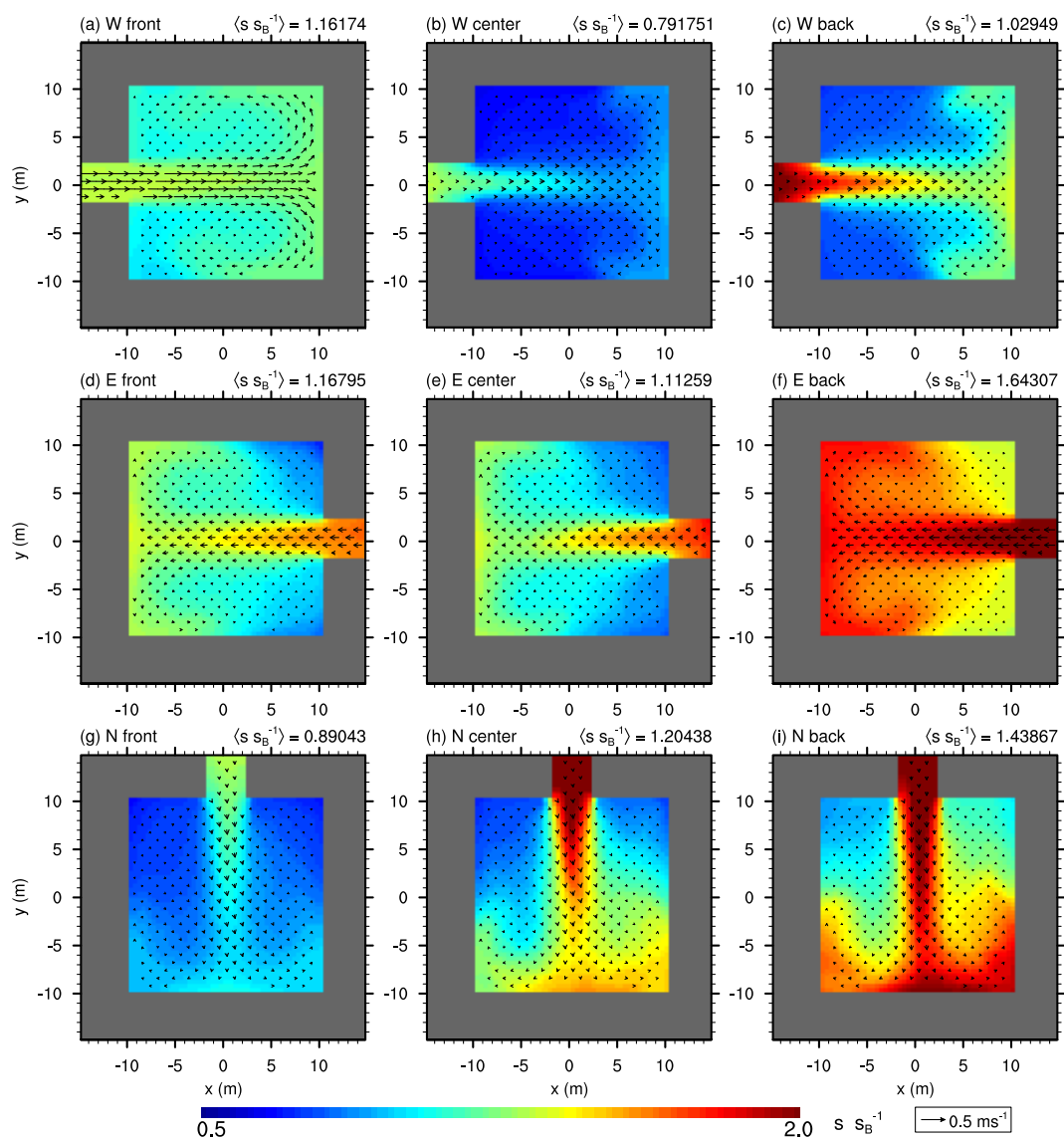

Figure 8. Xy-cross-section of the mean flow field (vector arrows) and mean scalar concentration (contours) within courtyards at $z = 1.8$ m for case AR3. Scalar concentration is normalized with the background concentration s_B at $z = H$. Please note, for reasons of space, not all realizations are shown.

Courtyards with an eastward opening indicate an even stronger mean inflow (see Figure 8d–f), which comes together with high mean concentrations near the courtyard surface. The highest mean concentrations can be observed for courtyard "E back", which can be attributed to the near-surface re-circulation downstream of the building that entrains scalar through the opening into the courtyard.

The north/southward-opened courtyards also show a mean inflow into the courtyard, which is also accompanied by higher scalar concentrations. The scalar concentration within the courtyard increases from the front- towards the back-row courtyard (Figure 8g–i), which can be attributed to the increasing scalar concentration along the *x*-parallel street canyon, as indicated by Figure 6.

3.1.3. Case AR03

Figures 9 and 10 show vertical and horizontal cross-sections of the mean flow and scalar concentration for the wide courtyard setup AR03, respectively. As expected, the flow pattern and scalar distribution within the street canyons is comparable to case AR1. Within the closed courtyards, however, the re-circulation is shifted towards the windward building wall and covers only about two thirds of the cavity along the *x*-direction, while mean scalar concentrations are comparable to those in case AR1. Furthermore, in Figure 10a it strikes that near the leeward corners of the courtyard a pair of horizontally re-circulating eddies can be observed.
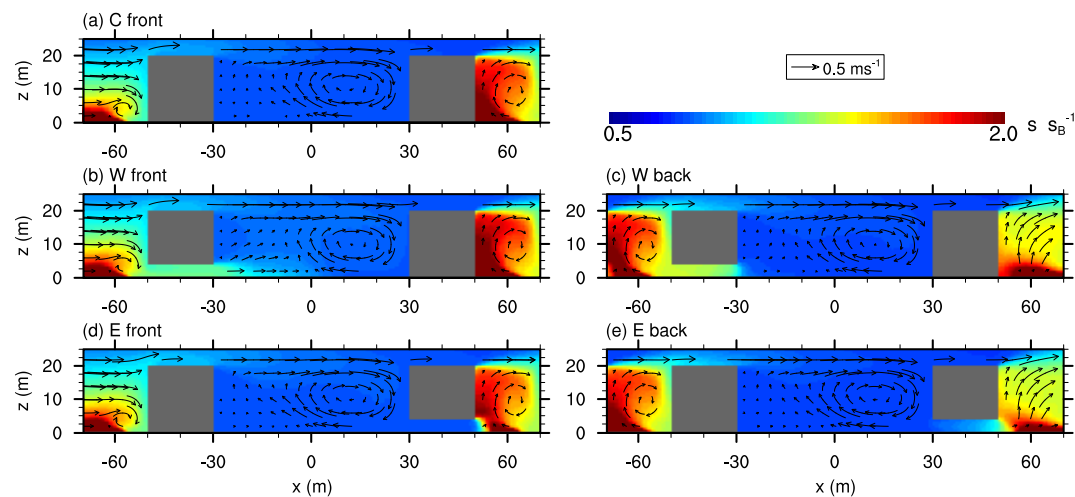

Figure 9. *Xz*-cross-section of the mean flow field (vector arrows) and scalar concentration (contours) at the courtyard center for case AR03. Please note, for reasons of space, not all realizations are shown.

Similar to the other aspect-ratio cases, "W front" shows a mean inflow through its opening, strengthening the pair of horizontal eddies near the surface and reaching into the courtyard about half its width (Figure 10b). The re-circulation (Figure 9b) within the courtyard, however, is less affected compared to case AR1 as it is already shifted towards the windward building wall. The mean scalar concentration shows higher values about half way into the courtyard near the surface, before it is transported upwards by the re-circulation and further mixed.

"W back" exhibits high scalar concentration along the tunnel-like opening. This actually contradicts with the re-circulation in the upwind street canyon that counteracts an inflow through the opening (similar to case AR1). However, the pair of horizontal eddies within the courtyard might promote the weak inflow of polluted air into the cavity (see Figure 10c).

Furthermore, it surprises that courtyards with an eastward opening do not show high concentrations, which is in contrast to case AR1 and AR3 (compare Figure 10d and, e.g., Figure 5g), even though the re-circulation pattern within the relevant street canyons are similar in shape and

strength compared to case AR1. Even a weak outflow through the eastward opening can be observed in Figure 10d (also present but weaker for "E back").

Results for courtyards with northward and southward openings (not shown) are similar to those of case AR1, except for the mean scalar concentration which is lower due to the larger courtyard volume compared to case AR1.
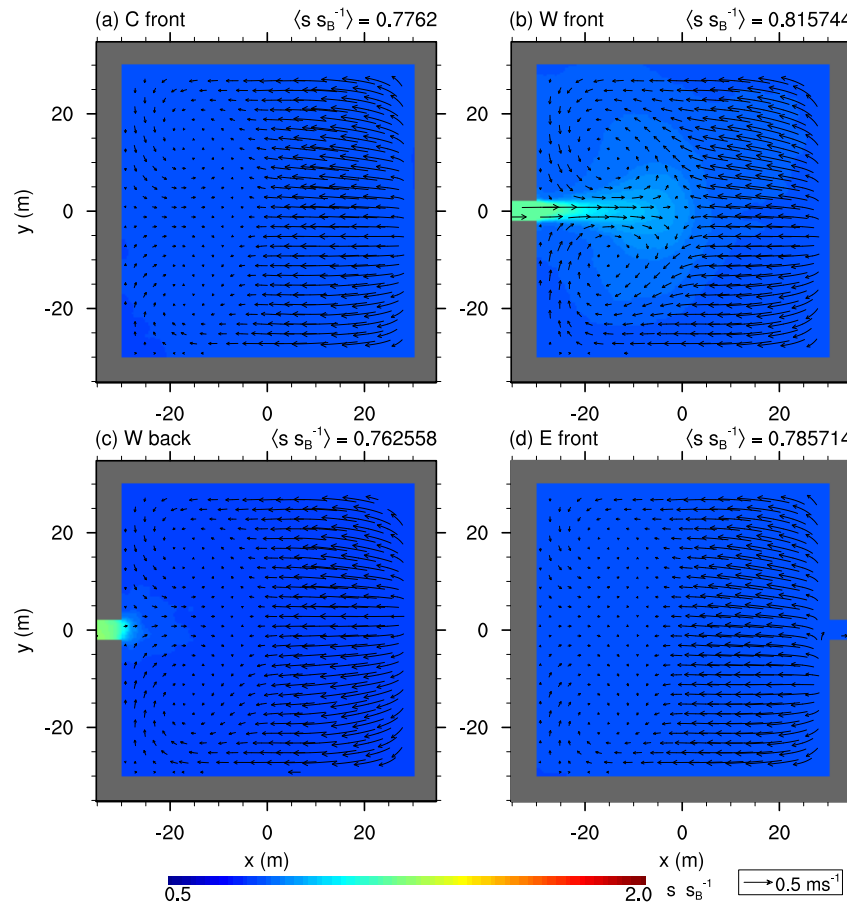

Figure 10. Xy-cross-section of the mean flow field (vector arrows) and scalar concentration (contours) within courtyards at $z = 1.8\,\mathrm{m}$ for case AR03. Scalar concentration is normalized with the background concentration s_B at $z = H$. Please note, for reasons of space, not all realizations are shown.

3.2. Quantification of Net Scalar Transport

In Section 3.1, we showed that the mean scalar concentration within the courtyards can be quite different among the different courtyard realizations, depending on the orientation of the opening, the incoming flow, as well as the strength and shape of the street-canyon circulation. The mean concentration, however, depends not only on the amount of entrained scalar into the courtyard but also on how long the scalar resides within the courtyard volume. Hence, to quantify how much scalar is transported through the lateral openings and thus estimate their significance on courtyard pollution, we calculated the net transport of scalar through the vertical and lateral openings as described in Section 2.2.

Figure 11 shows the time-averaged net transport of scalar into the courtyard volume by the lateral and the vertical opening for the different courtyard realizations. Positive values indicate increasing scalar concentrations within the courtyard and vice versa. As expected, the closed courtyards (black symbols) show slightly positive net transport through the top opening, which indicates slightly

increasing concentration within the courtyard cavity during the analysis period. For all ARs, the highest net transport by the lateral opening can be observed for the "W front" courtyards (blue circle, Figure 11), attributed to the non-blocked incoming flow. At this point, we want to emphasize that a high net transport into the courtyard does not necessarily correlate with high scalar concentrations. This becomes obvious for "W front" and "E back" in case AR3 (blue circle and green square, Figure 11a), where "W front" exhibits higher net transport than "E back" but shows lower mean concentration (see also Figure 8a,f). This is because the high net transport through the lateral opening for "W front" is relatively quickly compensated by the vertical transport across the top opening, while for "E back", the entrained scalar resides for a longer time within the courtyard leading to higher mean concentrations.
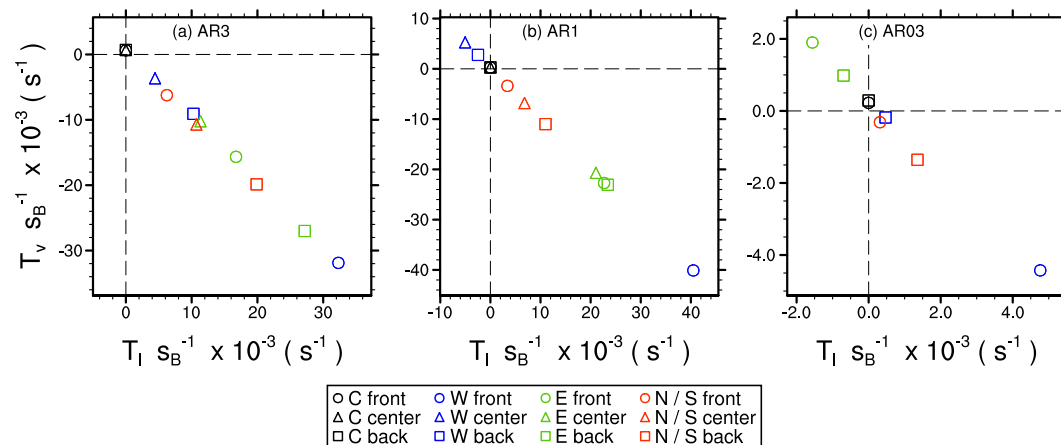

Figure 11. Net transport of scalar into the courtyard volume through the lateral (abscissa) and the top opening (ordinate), for (**a**) case AR $= 3$, (**b**) AR $= 1$, and (**c**) case AR $= 0.3$, averaged over 2 h of simulation time. Net transport is normalized with the background concentration. Positive (negative) values of net transport indicate increasing (decreasing) scalar concentration within the courtyard cavity. The dashed horizontal and vertical lines indicate zero values.

For the "W center" and "W back" courtyards (blue triangle and square, Figure 11) the situation is different among the different ARs. In case AR3 and AR03 (Figure 11a,c), scalar is entrained through the lateral opening and detrained through the top opening, while in case AR1 (Figure 11b), these courtyards show a net detrainment of scalar through the lateral opening and a net entrainment of scalar through the top opening, according to the mean concentration level shown in Figure 4.

For cases AR3 and AR1, the courtyards with eastward openings (green symbols, Figure 11a,b) show positive net transport through the lateral opening. In contrast, for case AR03 (Figure 11c), the eastward-opened courtyards show a negative net transport of scalar through the lateral opening. As we already mentioned in Section 3.1, this is in contradiction to the shape of the circulation patterns within the courtyard and the adjacent street canyon, which both points towards the courtyard center and thus should promote the transport of scalar-rich air into the courtyard (see Figure 9d,e). This gives rise to the question of how important theses circulations are for the transport of scalar through the lateral opening. Here, we must note that investigating this question is beyond the scope of this study. Hence, we postpone a more detailed analysis of this contradiction, as well as a quantitative analysis of the relevant transport mechanisms (re-circulation or random turbulent mixing) responsible for the lateral mixing of scalar into the courtyard to a follow-up study.

The north/southward-opened courtyards (red symbols) indicate a net transport through the lateral opening for all ARs, which is in accordance to the high mean concentrations within the tunnel-like opening (see, e.g., Figure 8). It strikes that the net transport through the lateral opening is lowest for the front-row courtyard and highest for the back-row courtyard. This is related to

the increasing scalar concentration along the *x*-parallel street canyon, with the largest gradient in concentration between street canyon and courtyard in the back row.

3.3. High Scalar Concentration Events

The previous analysis revealed that mean scalar concentrations within the courtyard cavities are lower compared to the adjacent street canyons. To estimate the impact on human health, however, the exposure to high concentrations and their relative occurrence are also relevant. To investigate whether lateral openings promote the occurrence of high concentrations within courtyards, we calculated PDFs from the sampled scalar concentrations at the courtyard center at a height of 1.8 m (representative for human exposure). Figure 12 shows the PDFs for the different ARs and courtyard setups. Among the different ARs, the closed courtyards (black curves) show similar PDFs with quite narrow Gaussian-shaped distributions and median values below the background concentration, indicating that almost no high concentrations are mixed from the top into the courtyard. For case AR03 (Figure 12c), almost all courtyard geometries show PDFs which are quite similar to the closed-courtyard PDFs. Only the "W front" courtyard (solid blue curve) shows a slightly skewed PDF where scalar concentrations reach values up to 1.5 times the background concentration, which is due to the direct inflow of scalar-rich air from the street canyon through the lateral opening. Similarly skewed PDFs can be observed for the "W front" courtyards in case AR3 and AR1 (Figure 12a,b).
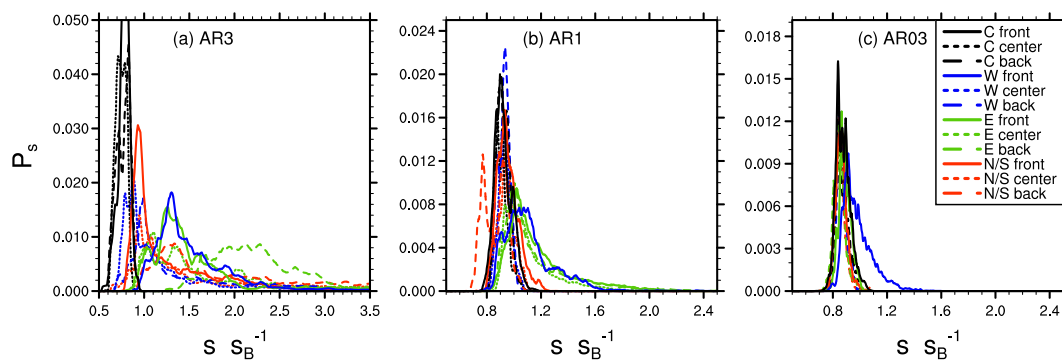

Figure 12. Probability density function of scalar concentration at courtyard center at $z = 1.8$ m for (**a**) case AR = 3, (**b**) AR = 1, and (**c**) case AR = 0.3. The scalar concentration is normalized with the background concentration s_B, which is the domain-averaged concentration at $z = H$.

In case AR1 (Figure 12b), also the eastward-opened courtyards (green curves) exhibit PDFs that are skewed towards higher concentrations, which is in accordance with the increased lateral mixing of scalar into the courtyard via the lateral opening (see Figures 5 and 11). In the high aspect ratio case AR3 (Figure 12a), all open-courtyard setups show skewed PDFs that tend towards higher concentrations, with maximum values multiple times the background concentration. Especially "E back" (green dashed curve) as well as the north/southward-opened courtyards (red curves) show a significant number of high-concentration events, according to the high lateral net transport of scalar into the courtyard (see Figure 11a).

3.4. Residence Time of Pollutants

To estimate for how long scalar resides within the courtyards, we applied a Lagrangian particle model embedded into the LES and evaluated of how long particles reside within the courtyard cavity. Figure 13 shows the PDFs of particle residence times for the different courtyard realizations. In case AR03 (Figure 13c), as expected, no significant differences between the different courtyard setups can be observed, indicating that the overall impact of lateral openings onto courtyard ventilation is negligible in this case as all courtyards are already well ventilated by the large top opening. The PDFs

are skewed towards larger residence times, with a small number of particles that reside up to 2000 s within the courtyard; we could trace this back to particles that were trapped mainly near the corners of the courtyard within the pair of horizontal eddies which are most pronounced for "W front" (see Figure 10). Most particles, however, reside only for a few hundreds of seconds within the courtyard, with peak positions at about 100 s (see Figure 13c).
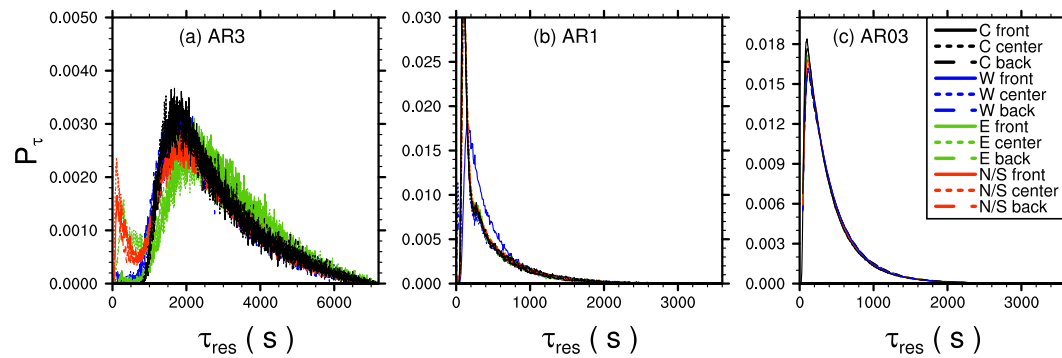

Figure 13. Probability density functions of particle residence times within the courtyard volume, for (**a**) case AR3, (**b**) AR1, and (**c**) case AR03.

Similar PDFs can be observed for case AR1 (Figure 13b), with no significant differences among the courtyard setups, except for the "W front" courtyard (solid blue curve) with slightly higher residence times. There, the re-circulation within the courtyard cavity is disturbed by the lateral inflow and does not reach down to the surface so that vertical particle transport in the lower part of the cavity is less effective. Taking particle residence times as a direct measure of ventilation, this means that "W front" openings even slightly decrease courtyard ventilation in case AR1, which agrees with the findings of Hall et al. [2] who also observed less ventilated courtyards if the flow can directly enter the courtyard through the opening.

For the high aspect ratio case AR3 (Figure 13a), the peak positions are shifted towards longer times of about 1800 s to 2300 s, meaning that particles reside for a significantly longer time period within the courtyard compared to the lower aspect-ratio cases.

This is not surprising for two reasons: first, the vertical distance between the particle source and the particle sink at the top opening is larger compared to AR1 and AR03; and second, the flow near the surface is detached from the upper part within the courtyard as shown in Figure 7, which reduces turbulent mixing within the lower part of the courtyard. For AR3 (Figure 13a), it strikes that "E center" (dotted green curve) as well as the north/southward-opened courtyards (red curves), exhibit a secondary peak at about 100 s, with a significant number of particles reside only for a short period of time within the courtyard cavity, while the bulk of particles reside for longer period of time. This secondary peak indicates intermittent mixing events where particles are quickly mixed out of the courtyard at some point in time; in fact, we could observe intermittent events in the scalar timeseries sampled at the courtyard center for these courtyards (not shown). At this point, however, we note that the physical mechanisms that promote this behavior for these building setups are not clear, drawing the need to investigate this in more detail in follow-up studies.

Furthermore, we note that the larger residence times observed in case AR3 come together with the increased number of high-concentration events as discussed in Section 3.3. This, in turn, suggests that scalar that is once mixed into the courtyards remains there for a longer time, increasing the human exposure to pollutants in such courtyard geometries.

4. Conclusions

We performed a set of LESs for idealized building-courtyard setups where we altered the height-to-width ratio of the courtyard cavities. Based on this, we studied the effect of tunnel-like

lateral openings onto courtyard ventilation and pollution. We considered different orientations of lateral openings with respect to the mean flow direction, as well as different arrangements of the building blocks, with non-blocked and blocked oncoming flow in the front- and center/back-building row, respectively.

To estimate courtyard ventilation, we calculated residence times using a Lagrangian particle model embedded into the LES. Courtyards with an AR of one (courtyard width equals courtyard depth) and wide courtyards show similar residence times with mean values of a few hundreds of seconds, indicating that both geometries are similarly ventilated. In contrast, deep courtyard geometries show significantly larger residence times with mean values of more than half an hour. We showed that lateral openings can affect courtyard ventilation in different ways, ranging from increasing to decreasing the ventilation. Wide courtyards show almost no impact of lateral openings on ventilation as these are already well ventilated via the top opening. Also, courtyards with an AR of one show no significant effect of lateral openings onto the ventilation, except for windward lateral openings in the front row. There, courtyard ventilation is slightly decreased since the re-circulation within the courtyard cavity is partly disturbed by the direct lateral inflow, so that the vertical exchange within the lower half of the cavity is less effective, which is in accordance to the results shown by Hall et al. [2].

In terms of ventilation, the deep courtyards indicate a more complex behavior. Courtyards with windward openings as well as leeward openings in the front and center row show similar residence times than closed courtyards. This is different for lateral openings with orientation perpendicular to the mean flow as well as leeward-orientated openings in the back row. There, the residence times indicate the occurrence of two alternating regimes, one similar to that in the closed-courtyard case with large residence times indicating poorly ventilated courtyard cavities, and a second one with low residence times indicating well-ventilated cavities. However, within this study we did not analyze this in more detail, nor did we figure out what are the responsible mechanism that promote such intermittent mixing events. This must be part of future research.

To study the effect of lateral openings onto courtyard pollution, we emitted a passive scalar along the center of the street canyons, emulating pollution by traffic. For the deep courtyards, on average, scalar is entrained through the lateral opening and detrained through the top opening for all considered courtyard realizations. The largest entrainment can be observed through the windward openings in the front row, where the flow can enter the courtyard unhinderedly. Courtyards with leeward openings in the back row show also large entrainment of scalar through the lateral opening, as the re-circulation downstream of the building transports high scalar concentrations towards the opening. Likewise, deep courtyards with openings oriented perpendicularly to the mean flow are strongly polluted as a mean inflow develops from the street canyon into the courtyard.

The large entrainment also causes deep courtyards with lateral openings to show a significant increase of mean scalar concentration as well as an increased number of high-concentration events compared to closed courtyards. This, in turn, reveals the negative impact of lateral openings on the air quality in deep courtyards. In addition, this comes together with large particle residence times in deep courtyards, indicating that once high scalar concentration is mixed into the courtyard cavity, it stays therein for a while. However, to estimate the impact on human health issues, future studies need to draw a clear connection between high scalar concentrations and large particle residence times, where this study was not designed for. For example, suppose high concentrations are recurrently entrained into the courtyard but mixed out relatively quickly, while low concentrations remain in the courtyard cavity for a longer time. Now, suppose a situation where high concentrations are only entrained into the courtyard occasionally but mixed out very slowly. Both situations could lead to similar particle residence times, high-concentration events, and mean concentrations but may have a significantly different impact on human health, e.g., [4,5,15].

For courtyards with an AR of one, scalar is entrained through the lateral opening and detrained through the top opening for most of the courtyard realizations. Largest entrainment could be observed through the windward openings in the front row and through the leeward openings, where also the

highest mean concentrations as well as the highest number of high-concentration events could be observed. For windward lateral openings in the center and back row, however, the situation becomes different and, on average, scalar is detrained through the lateral opening and entrained through the top opening. This is mainly attributed to the re-circulation within the crosswind-aligned street canyon and the courtyard circulation which cause a mean outflow through the opening.

For wide courtyards, again, the largest net entrainment through the lateral opening can be observed for windward openings in the front row, while detrainment through the lateral opening can be observed for the leeward openings.

To summarize, the effects of lateral openings on courtyard pollution and ventilation are diverse. In general, it can be said that the influence of lateral openings weakens for decreasing AR (courtyards become wider). For courtyards with low AR, the ventilation and pollutant de- and entrainment through the top dominates, so that laterally opened courtyards exhibit very similar flow patterns and scalar distributions as closed courtyards. In contrast, for high ARs, lateral openings strongly alter the ventilation and air quality within courtyards, as the bottom part of the courtyard cavity is poorly ventilated from the top opening.

We note that our idealized study only covers a small part of possible courtyard configurations and air pollution scenarios. For example, different opening sizes or opening locations that are not centered may also affect the entrainment of scalar into the courtyards, as well as the flow within the courtyard and thus its ventilation. Hall et al. [2] had shown that also solid obstacles at the courtyard surface decrease the ventilation and increase concentrations near the surface. We expect the same for plant canopy located within courtyards, which would perturb the courtyard circulation and suppresses turbulent mixing. This case, even wide courtyard geometries may become poorly ventilated by the top opening, so that the impact of lateral openings on air pollution gains further relevance.

In this study, we considered only scalar sources on the streets. However, inner-courtyard sources (courtyards are also often used as car parks) or domestic fuel may also be important with respect to the air quality within courtyards. Hence, lateral openings may possibly become even important for scalar removal from courtyards.

Also, buildings and roof shapes, e.g., [13], as well as variable building heights, e.g., [12,14] may alter courtyard ventilation, to name only a few of possible parameters.

Another aspect we neglected in our study are buoyancy effects. Thermodynamic effects can significantly alter ventilation patterns in street canyons [20] or even in entire cities [38]. We expect this will account for courtyards as well. Especially in warmer climates, where courtyards are often used to control indoor ventilation and cooling, different studies, e.g., [39] already revealed that courtyards of different depth can increase or decreased thermal ventilation.

References

1. Reynolds, J.S. *Courtyards: Aesthetic, Social, and Thermal Delight*; John Wiley & Sons, Inc.: New York, NY, USA, 2002.

2. Hall, D.; Walker, S.; Spanton, A. Dispersion from courtyards and other enclosed spaces. *Atmos. Environ.* **1999**, *33*, 1187–1203. [CrossRef]

3. Swietlicki, E.; Puri, S.; Hansson, H.C.; Edner, H. Urban air pollution source apportionment using a combination of aerosol and gas monitoring techniques. *Atmos. Environ.* **1996**, *30*, 2795–2809. [CrossRef]

4. Beelen, R.; Raaschou-Nielsen, O.; Stafoggia, M.; Andersen, Z.J.; Weinmayr, G.; Hoffmann, B.; Wolf, K.; Samoli, E.; Fischer, P.; Nieuwenhuijsen, M.; et al. Effects of long-term exposure to air pollution on natural-cause mortality: An analysis of 22 European cohorts within the multicentre ESCAPE project. *Lancet* **2014**, *383*, 785–795. [CrossRef]

5. Shah, A.S.V.; Lee, K.K.; McAllister, D.A.; Hunter, A.; Nair, H.; Whiteley, W.; Langrish, J.P.; Newby, D.E.; Mills, N.L. Short term exposure to air pollution and stroke: Systematic review and meta-analysis. *BMJ* **2015**, *350*, h1295. [CrossRef] [PubMed]

6. Lo, K.W.; Ngan, K. Characterizing Ventilation and Exposure in Street Canyons Using Lagrangian Particles. *J. Appl. Meteorol. Climatol.* **2017**, *56*, 1177–1194. [CrossRef]

7. Ok, V.; Yasa, E.; Özgunler, M. An Experimental Study of the Effects of Surface Openings on Air Flow Caused by Wind in Courtyard Buildings. *Arch. Sci. Rev.* **2008**, *51*, 263–268. [CrossRef]

8. Weber, S.; Weber, K. Coupling of urban street canyon and backyard particle concentrations. *Meteorol. Z.* **2008**, *17*, 251–261. [CrossRef]

9. Ryu, Y.H.; Baik, J.J. Flow and dispersion in an urban cubical cavity. *Atmos. Environ.* **2009**, *43*, 1721–1729. [CrossRef]

10. Moonen, P.; Dorer, V.; Carmeliet, J. Evaluation of the ventilation potential of courtyards and urban street canyons using RANS and LES. *J. Wind Eng. Ind. Aerodyn.* **2011**, *99*, 414–423. [CrossRef]

11. Moonen, P.; Dorer, V.; Carmeliet, J. Effect of flow unsteadiness on the mean wind flow pattern in an idealized urban environment. *J. Wind Eng. Ind. Aerodyn.* **2012**, *104*, 389–396. [CrossRef]

12. Assimakopoulos, V.D.; ApSimon, H.M.; Moussiopoulos, N. A numerical study of atmospheric pollutant dispersion in different two-dimensional street canyon configurations. *Atmos. Environ.* **2003**, *37*, 4037–4049. [CrossRef]

13. Xie, X.; Huang, Z.; Wang, J.S. Impact of building configuration on air quality in street canyon. *Atmos. Environ.* **2005**, *39*, 4519–4530. [CrossRef]

14. Kurppa, M.; Hellsten, A.; Auvinen, M.; Raasch, S.; Vesala, T.; Järvi, L. Ventilation and Air Quality in City Blocks Using Large-Eddy Simulation—Urban Planning Perspective. *Atmosphere* **2018**, *9*, 65. [CrossRef]

15. Kampa, M.; Castanas, E. Human health effects of air pollution. *Environ. Pollut.* **2008**, *151*, 362–367. [CrossRef] [PubMed]

16. Zauli Sajani, S.; Trentini, A.; Rovelli, S.; Ricciardelli, I.; Marchesi, S.; Maccone, C.; Bacco, D.; Ferrari, S.; Scotto, F.; Zigola, C.; et al. Is particulate air pollution at the front door a good proxy of residential exposure? *Environ. Pollut.* **2016**, *213*, 347–358. [CrossRef] [PubMed]

17. Maronga, B.; Gryschka, M.; Heinze, R.; Hoffmann, F.; Kanani-Sühring, F.; Keck, M.; Ketelsen, K.; Letzel, M.O.; Sühring, M.; Raasch, S. The Parallelized Large-Eddy Simulation Model (PALM) version 4.0 for atmospheric and oceanic flows: Model formulation, recent developments, and future perspectives. *Geosci. Model Dev.* **2015**, *8*, 2515–2551. [CrossRef]

18. Letzel, M.O.; Krane, M.; Raasch, S. High resolution urban large-eddy simulation studies from street canyon to neighbourhood scale. *Atmos. Environ.* **2008**, *42*, 8770–8784. [CrossRef]

19. Letzel, M.O.; Helmke, C.; Ng, E.; An, X.; Lai, A.; Raasch, S. LES case study on pedestrian level ventilation in two neighbourhoods in Hong Kong. *Meteorol. Z.* **2012**, *21*, 575–589. [CrossRef]

20. Park, S.B.; Baik, J.J.; Raasch, S.; Letzel, M.O. A Large-Eddy Simulation Study of Thermal Effects on Turbulent Flow and Dispersion in and above a Street Canyon. *J. Appl. Meteorol. Climatol.* **2012**, *51*, 829–841. [CrossRef]

21. Hellsten, A.; Luukkonen, S.M.; Steinfeld, G.; Kanani-Sühring, F.; Markkanen, T.; Järvi, L.; Lento, J.; Vesala, T.; Raasch, S. Footprint Evaluation for Flux and Concentration Measurements for an Urban-Like Canopy with Coupled Lagrangian Stochastic and Large-Eddy Simulation Models. *Bound.-Lay. Meteorol.* **2015**, *157*, 191–217. [CrossRef]

22. Lo, K.W.; Ngan, K. Characterising the pollutant ventilation characteristics of street canyons using the tracer age and age spectrum. *Atmos. Environ.* **2015**, *122*, 611–621. [CrossRef]

23. Deardorff, J.W. Stratocumulus-capped mixed layers derived from a three-dimensional model. *Bound.-Lay. Meteorol.* **1980**, *18*, 495–527. [CrossRef]

24. Wicker, L.J.; Skamarock, W.C. Time-Splitting Methods for Elastic Models Using Forward Time Schemes. *Mon. Weather Rev.* **2002**, *130*, 2088–2097. [CrossRef]

25. Williamson, J.H. Low-storage Runge-Kutta schemes. *J. Comput. Phys.* **1980**, *35*, 48–56. [CrossRef]

26. Munters, W.; Meneveau, C.; Meyers, J. Shifted periodic boundary conditions for simulations of wall-bounded turbulent flows. *Phys. Fluids* **2016**, *28*, 025112. [CrossRef]

27. Park, S.B.; Baik, J.J.; Han, B.S. Large-eddy simulation of turbulent flow in a densely built-up urban area. *Environ. Fluid Mech.* **2015**, *15*, 235–250. [CrossRef]

28. Antoniou, N.; Montazeri, H.; Wigo, H.; Neophytou, M.K.A.; Blocken, B.; Sandberg, M. CFD and wind-tunnel analysis of outdoor ventilation in a real compact heterogeneous urban area: Evaluation using "air delay". *Build. Environ.* **2017**, *126*, 355–372. [CrossRef]

29. Holzer, M.; Hall, T.M. Transit-Time and Tracer-Age Distributions in Geophysical Flows. *J. Atmos. Sci.* **2000**, *57*, 3539–3558. [CrossRef]

30. Weil, J.C.; Sullivan, P.P.; Moeng, C.H. The Use of Large-Eddy Simulations in Lagrangian Particle Dispersion Models. *J. Atmos. Sci.* **2004**, *61*, 2877–2887. [CrossRef]

31. Thomson, D.J. Criteria for the selection of stochastic models of particle trajectories in turbulent flows. *J. Fluid Mech.* **1987**, *180*, 529–556. [CrossRef]

32. Steinfeld, G.; Raasch, S.; Markkanen, T. Footprints in Homogeneously and Heterogeneously Driven Boundary Layers Derived from a Lagrangian Stochastic Particle Model Embedded into Large-Eddy Simulation. *Bound.-Layer Meteorol.* **2008**, *129*, 225–248. [CrossRef]

33. Pope, S.B. Ten questions concerning the large-eddy simulation of turbulent flows. *New J. Phys.* **2004**, *6*, 35. [CrossRef]

34. Freitag, M.; Klein, M. An improved method to assess the quality of large eddy simulations in the context of implicit filtering. *J. Turbul.* **2006**, *7*, N40. [CrossRef]

35. Kim, J.J.; Baik, J.J. A numerical study of the effects of ambient wind direction on flow and dispersion in urban street canyons using the RNG k-e turbulence model. *Atmos. Environ.* **2004**, *38*, 3039–3048. [CrossRef]

36. Lim, H.C.; Thomas, T.; Castro, I.P. Flow around a cube in a turbulent boundary layer: LES and experiment. *J. Wind Eng. Ind. Aerodyn.* **2009**, *97*, 96–109. [CrossRef]

37. Xie, Z.T.; Castro, I.P. Large-eddy simulation for flow and dispersion in urban streets. *Atmos. Environ.* **2009**, *43*, 2174–2185. [CrossRef]

38. Gronemeier, T.; Raasch, S.; Ng, E. Effects of Unstable Stratification on Ventilation in Hong Kong. *Atmosphere* **2017**, *8*, 1–15. [CrossRef]

39. Rojas, J.M.; Galán-Marín, C.; Fernández-Nieto, E.D. Parametric Study of Thermodynamics in the Mediterranean Courtyard as a Tool for the Design of Eco-Efficient Buildings. *Energies* **2012**, *5*, 2381–2403. [CrossRef]

5 Effects of Unstable Stratification on Ventilation in Hong Kong

5.1 Declaration of Contributions

T. Gronemeier, S. Raasch and E. Ng designed the simulations. T. Gronemeier carried out all simulations and test simulations with supervision of S. Raasch. T. Gronemeier and S. Raasch conducted the data analysis. T. Gronemeier wrote the manuscript with support from S. Raasch. Comments of two anonymous referees helped to improve the final version of the manuscript.

5.2 Research Article

atmosphere

MDPI

Article

Effects of Unstable Stratification on Ventilation in Hong Kong

Tobias Gronemeier [1],* , Siegfried Raasch [1] and Edward Ng [2,3,4]

[1]   Insitute of Meteorology and Climatology, Leibniz Universität Hannover, 30419 Hannover, Germany;
      raasch@muk.uni-hannover.de
[2]   School of Architecture, The Chinese University of Hong Kong, Hong Kong, China; edwardng@cuhk.edu.hk
[3]   Institute of Future City (IOFC), The Chinese University of Hong Kong, Hong Kong, China
[4]   Institute of Energy, Environment and Sustainability (IEES), The Chinese University of Hong Kong,
      Hong Kong, China
*   Correspondence: gronemeier@muk.uni-hannover.de; Tel.: +49-511-762-3232

Abstract: Ventilation in cities is crucial for the well being of their inhabitants. Therefore, local governments require air ventilation assessments (AVAs) prior to the construction of new buildings. In a standard AVA, however, only neutral stratification is considered, although diabatic and particularly unstable conditions may be observed more frequently in nature. The results presented here indicate significant changes in ventilation within most of the area of Kowloon City, Hong Kong, included in the study. A new definition for calculating ventilation was introduced, and used to compare the influence of buildings on ventilation under conditions of neutral and unstable stratification. The overall ventilation increased due to enhanced vertical mixing. In the vicinity of exposed buildings, however, ventilation was weaker for unstable stratification than for neutral stratification. The influence on ventilation by building parameters, such as the plan area index, was altered when unstable stratification was considered. Consequently, differences in stratification were shown to have marked effects on ventilation estimates, which should be taken into consideration in future AVAs.

Keywords: convective boundary layer; LES (large-eddy simulations); street-level ventilation

1. Introduction

Air ventilation is a crucial factor of city climate and has a major impact on the well being of the urban population. The wind field within a city, and hence ventilation, is markedly influenced by the actual building setup (e.g., [1–3]). Accordingly, local governments, particularly those of larger cities, have started to regulate the construction of new buildings to maintain or improve ventilation. As a consequence, an air ventilation assessment (AVA) is usually required to obtain approval for large building projects [2]. These AVAs typically only require wind tunnel experiments. However, wind tunnel experiments have the disadvantage of usually only being capable of reproducing neutrally stratified atmospheric conditions, and the effects of diabatic stratification on ventilation are neglected. This is often justified when focusing on high wind speeds, where mechanically induced turbulence has a greater influence on ventilation than turbulence generated by buoyancy, which is only present if diabatic stratification is considered.

However, the most crucial situations for city ventilation are those where only a low wind speed is present, which drastically reduces ventilation. For such situations, the building setup must be well organized to ensure sufficient ventilation of the whole city area. However, the assumption that buoyancy-driven turbulence only has a minor influence on ventilation is not true in such low-wind situations. Particularly for regions with regularly occurring low wind speeds, an AVA that solely

focuses on neutral conditions may not include the actual ventilation effects of planned buildings within the study area. Therefore, the validity of such an AVA would be limited.

This study was performed to identify the limitations if only neutral conditions are considered when analyzing air ventilation under weak-wind conditions. We computed and compared the ventilation under neutral and unstable atmospheric conditions. Ventilation analyses were performed for Kowloon City, Hong Kong, by large-eddy simulations (LES).

The LES technique predicts the wind field within a building array more accurately than a Reynolds-averaged Navier-Stokes (RANS) simulation [4]. LES resolves the large energy-containing turbulence elements (eddies) and only parameterizes the small (sub-grid)-scale turbulence, while the RANS technique parameterizes the whole turbulence spectrum. This also has the advantage that the convective up- and downdrafts are directly simulated within the LES instead of being parameterized, which tends to give more realistic results.

Although there have been many studies regarding ventilation within large cities, particularly Hong Kong (e.g., [5–9]), there have been few high-resolution LES studies dealing with large real urban areas. Letzel et al. [10] investigated the ventilation in two areas within Kowloon City for neutral conditions using LES. They concluded that the urban morphology has a marked impact on ventilation. The ventilation of a single city quarter can be affected by its surroundings, which implies that neglecting the surrounding city area may lead to inaccuracies in ventilation analysis. Ref. Park et al. [11] utilized an LES model to study the ventilation in a region of roughly 7 km^2 within the densely built-up metropolitan area of Seoul, South Korea. Their results showed good ventilation of wide streets and at intersections, while poor ventilation was observed in densely built-up areas.

However, the above studies only analyzed neutral conditions excluding thermal buoyancy effects. Park and Baik [12] included thermal effects by surface heating, and found that the spanwise flow is stronger within an idealized building array compared to the non-heated case. Yang and Li [13] focused on the influence of stratification on ventilation considering a very simplified building array with a maximum of 21 blocks to simulate Hong Kong city. Turbulence was fully parameterized by the RANS model used in their study. Generally, higher ventilation was reported for unstable stratification in the case of weak background wind compared to neutral stratification. However, the simplifications (building setup and fully parameterized turbulence) allowed only a general evaluation of ventilation.

In this study, LES was used to analyze and compare ventilation in a large real metropolitan area (Kowloon City) for neutral and unstable stratification, whereas previous studies only focused on idealized building setups (e.g., [13]). There are a number of additional challenges for unstable stratification, including that a large model domain is required to catch all relevant turbulent structures, which are considerably larger than for neutral stratification, while the grid size must be kept small to sufficiently resolve the street-canyon flows (e.g., [10]). This substantially increases the computational expense of the simulations. Special attention must also be given to the choice of lateral boundary conditions such that they do not alter the ventilation results within the analyzed area. The comparison of ventilation for neutral and unstable stratification purely focused on the differences in how buildings influence ventilation under different stratification conditions. Ventilation effects due to differential heating between the city and the surroundings (e.g., sea-breeze effects) have not been studied and model setups have been chosen in a way that they are explicitly excluded. To the best of our knowledge, this is the first LES study to encompass a large realistic city domain with high (2 m) resolution and to compare ventilation results for different stratification.

The local government of Hong Kong initiated its AVA program focusing on summer weak-wind conditions [2]. These are the most hazardous conditions, as the weak wind in summer leads to a rapid increase in heat stress on the population and pollutants accumulate quickly in the streets because of reduced ventilation. This study therefore focused on these conditions.

The following text is divided into three parts. First, Section 2 presents a description of the simulation setup and the methods used; and Section 3 discusses the simulation results and compares two cases with different stratification. Finally, the conclusions are given in Section 4.

2. Model and Case Description

2.1. LES Model

The LES model PALM [14,15], version 4.0 revision 1746 (developed at the Insitute of Meteorology and Climatology of Leibniz Universität Hannover, Hannover, Germany), was used to perform the simulations in this study. It has been previously used to simulate the atmospheric boundary layer in densely built-up areas (e.g., [10,11,16]), and was successfully validated against wind-tunnel measurements within urban-like building arrays using neutrally and unstable stratified conditions [12,16,17]. PALM solves the non-hydrostatic incompressible Boussinesq equations.

2.2. Simulation Setup

Two cases were simulated with different types of atmospheric stratification. The first case featured neutral stratification, while the second had unstable stratification.

The simulation domains for the neutral and unstable cases are shown in Figure 1a,b, respectively. The simulated city area is detailed in Figure 1c and included an area of about 3.9 km × 4.7 km of Kowloon City. The same city area was used for both cases. Orographic features within the city area and the surroundings were neglected in order to limit ventilation effects purely to buildings and atmospheric stratification. The city was oriented south-north along the x (streamwise) direction and east-west along the y (spanwise) direction due to model constraints.
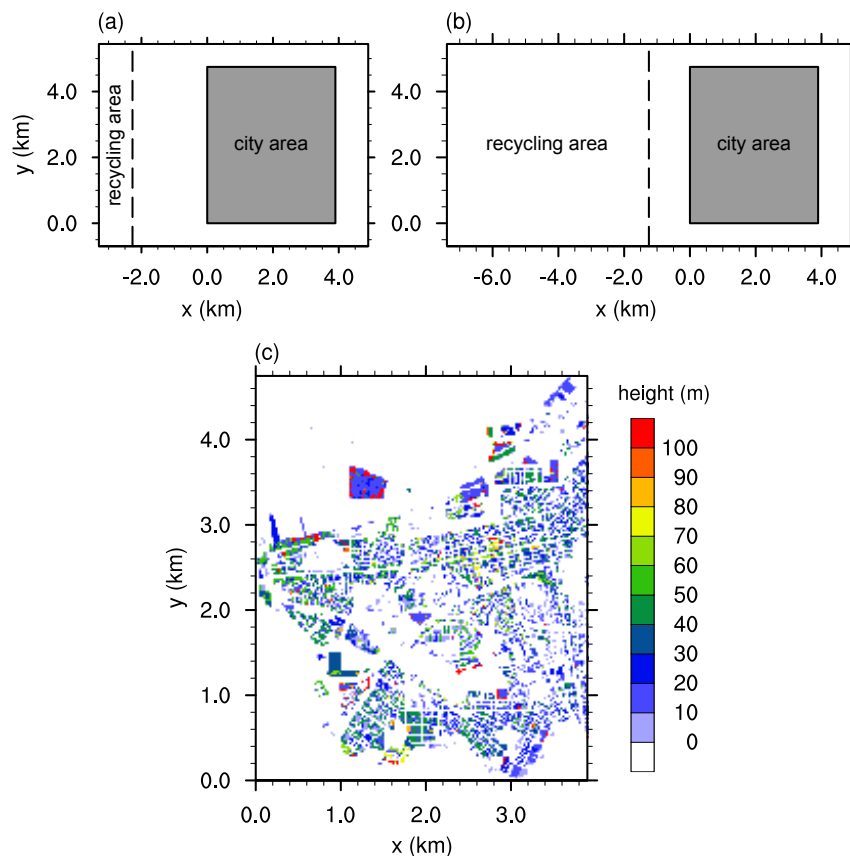

Figure 1. Domain setup for the (**a**) neutral case and (**b**) unstable case; building height information is depicted in (**c**). The dashed line marks the recycling area. The gray rectangle marks the city area shown in detail in (**c**).

A buffer region around the city ensured that the city area was not influenced by the domain boundaries. The buffer region had a width of 500 m at both sides (spanwise direction) and a length of 1000 m at the windward and leeward sides of the city. In the neutral case, the buffer region in front of the city had to be enlarged to 2000 m. The reduced mixing in the neutral case caused the blocking effects of the buildings to reach further upstream than in the unstable case, which required a larger windward buffer region.

To ensure a realistic turbulent inflow, a turbulence recycling method was used at the upstream boundary, which is described in more detail in Section 2.3. This method required an additional recycling domain at the inflow boundary with its length depending on the sizes of the turbulent structures. In the neutral case, a length of 1 km was sufficient for the recycling domain, while a length of 6 km was required in the unstable case. Upstream topographic features like Hong Kong Island were not considered. The outflow boundary condition used at the downstream boundary is described in Section 2.4. Cyclic boundary conditions were used in the spanwise direction.

The total domain sizes summed to 8 km (neutral case) and 12 km (unstable case) in the streamwise direction, 6 km in the spanwise direction, and 2.6 km in the vertical direction. Due to restrictions of the model grid, the exact domain size was 8192 m $\times$ 6144 m $\times$ 2653 m in the neutral case and 12.288 m $\times$ 6144 m $\times$ 2653 m in the unstable case.

The grid size was set to 2 m in each direction according to the results of a grid sensitivity study (see Appendix A). Starting at a height of 1100 m, the vertical grid size increased by 4% at each height level up to a maximum grid size of 40 m to reduce the computational time.

A Dirichlet boundary condition was applied at the top boundary and the Monin–Obukhov similarity theory was used at the bottom boundary as well as at the building walls. The roughness length was set to 0.1 m at each surface to account for roughness elements in the streets such as billboards, cars, and so forth. At the top boundary, Rayleigh damping was used to prevent the reflection of gravity waves.

In the unstable case, a constant near-surface heat flux of $0.165 \, \text{K m s}^{-1}$ (approximately $200 \, \text{W m}^{-2}$) was applied at every horizontal surface while a heat flux of 0 was set at all vertical building walls. This setup was comparable to the situation at noon in the summer with the sun situated in the zenith heating only horizontally oriented surfaces. Any additional heat release from buildings, for example, by air conditioning systems, was neglected. In addition, no distinction was made for different land use or land covers like water bodies or roads (i.e., no difference in surface heat flux). This simplification prevented the development of secondary circulations like sea-breeze, which would otherwise affect city ventilation [18].

The geostrophic wind was set to $1.5 \, \text{m s}^{-1}$ with a southerly wind direction (along a positive x direction), and the potential temperature θ was set to a constant value of 308 K within the boundary layer. This corresponded to daytime summer weak-wind conditions. To initialize the unstable case, a capping inversion layer was set above a height of 700 m where θ increased with a vertical gradient of $0.01 \, \text{K m}^{-1}$. A large-scale subsidence velocity was used to limit the growth of the boundary layer during the simulation. This prevented drifts in average wind speed and turbulence characteristics within the boundary layer. The large-scale subsidence velocity was set to zero at the surface and decreased linearly until it reached $-0.025 \, \text{m s}^{-1}$ at a height of 700 m from which it remained constant. After a spin-up time of 2 h, the boundary layer reached a height of 900 m and increased by only 60 m during the analysis period. The Coriolis force was taken into consideration.

Each simulation was initialized with turbulent three-dimensional velocity and temperature fields received from a precursor simulation with cyclic boundaries and a flat surface, and otherwise used the same setup as the main simulations.

Both cases were integrated over 6 h. Within the first 2 h, the turbulent fields adjusted to the urban surface and the simulations reached a quasi-stationary state. After this spin-up time, both cases were simulated for an additional 4 h to gain stable average values for the analysis. Simulations were performed using the Cray-XC40 supercomputer of the North-German Supercomputing Alliance

(HLRN) in Hannover, Germany. Due to the large domains and high spatial resolution, more than 7×10^9 and 12×10^9 grid points had to be used for the neutral and unstable case, respectively. The simulations required between 20 h and 60 h of computing time using more than 12,000 cores.

2.3. Inflow Boundary Conditions

To impose realistic inflow conditions on the LES, a turbulence recycling method was used at the inflow boundary following the method proposed by Lund et al. [19] and Kataoka and Mizuno [20]. A subdomain, named "recycling area" in Figure 1, was included in the simulation domain at the inflow boundary. Within this recycling area, the turbulence information Ψ' was recycled. Ψ' is defined as

$$\Psi' = \Psi - \langle \Psi \rangle_y, \tag{1}$$

where $\langle \dots \rangle_y$ denotes the spatial average along the spanwise or y direction, and is calculated at the downwind boundary of the recycling area. At the inflow boundary, Ψ' was added to a fixed mean inflow profile. Ψ was one of u, v, w or e, which were the wind velocity components in streamwise (x), spanwise (y), and vertical (z) directions, and subgrid-scale turbulent kinetic energy, respectively.

In the case of potential temperature θ, the method was altered such that, instead of the turbulent signal, the instantaneous value θ was copied from the downwind boundary of the recycling area and pasted to the inflow boundary. This ensured that the temperature level at the inflow boundary was equal to that in the simulation domain. Using the standard recycling method instead would cause a horizontal temperature gradient because the vertical temperature profile at the inlet would be fixed, while θ increased due to surface heating in the model domain. Then, this gradient would trigger a secondary circulation and hence alter the ventilation within the whole simulation domain. Although such a secondary circulation does occur in reality due to different surface heat-fluxes between Kowloon City and the surrounding bay, this effect on ventilation was omitted as it was not within the aim of the study.

The size of the recycling area was bound to the size of the turbulent structures present in the atmosphere. To ensure that the turbulent structures are not restricted by the size of the recycling area, its size must be large enough to enable the development of several turbulent structures of the largest occurring size but at least double the boundary layer height. In the neutral case, the boundary layer reached a height of 500 m. Hence, the size of the recycling area was set to 1 km in the streamwise direction, which proved to be sufficient. In the unstable case, the diameter of the convective cells, which was about 2 km, defined the size of the recycling area. To ensure that the convective cells could develop freely without being restricted by the boundaries of the recycling area, its size was set to three times the convective cell diameter, which was 6 km. Due to technical restrictions of the model grid, the actual size of the recycling domain was set to 1024 m and 6144 m in the neutral and unstable cases, respectively.

2.4. Outflow Boundary Condition

In PALM, a radiation boundary condition [21,22] was set as the standard outflow condition in the non-cyclic boundary case. However, this could not be used in the current study. The radiation boundary condition required a positive outflow (i.e., $u > 0$, at all times). This is not a problem if a sufficient background wind is considered like Park et al. [11] or Gryschka et al. [23] did. In this study, however, the weak background wind did not ensure that no negative u values occurred at the outflow boundary, particularly in the unstable case where strong turbulent motions were present. Once negative velocities occurred at the outflow, they were artificially strengthened by the radiation condition. This led to strong inward-directed artificial winds at the outflow boundary, which persisted in time.

To prevent these strong artificial winds, a new technique was introduced to handle the outflow. The instantaneous values of u, v, w, θ, and e were copied from a vertical plane (source plane), positioned

500 m in front of the outflow boundary, and then pasted to the outflow boundary. As the values were taken from within the simulation domain, they changed according to the flow field around the source plane and negative values were not artificially strengthened. This way, negative values were possible at the outflow boundary. It should be noted that this method was a technical workaround and did not represent the actual physics. However, the modification to the flow field was limited to the area close to the outflow boundary. A buffer zone of 1 km width ensured that the analysis area was unaffected by the boundary condition.

3. Results

The following analysis showed the differences in ventilation in varying atmospheric conditions. The analysis focused on the pedestrian height level 2 m above ground. All of the data are presented as averages during the last 4 h of each simulation unless otherwise stated.

First, to verify that the above-mentioned boundary conditions produced reasonable results, particularly from a meteorological viewpoint, Figure 2 shows the non-averaged vertical velocity component w and potential temperature θ for the unstable case at a height of 100 m at the last time step of the simulation. At this time point, the boundary layer reached a height of 960 m. The hexagonal structures visible in these figures had a size of about 2 km, which is within the typical range of 2–3 times the boundary layer height for a convective boundary layer [24]. Consequently, the size of the recycling area chosen was large enough to enable the development of several convective structures. Furthermore, no general horizontal temperature gradient was visible within the streamwise direction. This is because the temperature profile at the inflow boundary was constantly updated to the temperature level within the model domain as described in Section 2.3. Finally, none of the fields depicted in Figure 2 showed any visual effects due to the newly introduced outflow boundary condition, but retained their characteristics throughout the whole simulated domain.

Figure 3a,b depicts the magnitude of the time-averaged three-dimensional wind vector at 2 m height

$$V_{2\mathrm{m}} = \left. \overline{\sqrt{u^2 + v^2 + w^2}} \right|_{z=2\mathrm{m}} \tag{2}$$

for the neutral and unstable cases, respectively. It is obvious that $V_{2\mathrm{m}}$ was significantly higher throughout the whole city area and its surroundings in the unstable case compared to the neutral case. The average of $V_{2\mathrm{m}}$ in the unstable case was about 0.68 m s^{-1} or 1.9 times higher than that in the neutral case. The higher wind velocity in the unstable case was related to the greater downward vertical transport of momentum from above the city due to buoyancy-induced turbulence. It reflected the typical increase in near-surface winds during daytime (unstable stratification) compared to nighttime (neutral or stable stratification).

Figure 4 shows the vertical profile of the time and horizontally averaged horizontal wind vector $\left| \overline{\overline{v}_h} \right| = \sqrt{\overline{u}^2 + \overline{v}^2}$ for both cases within the recycling area (i.e., without building effects). The strong vertical mixing led to a higher velocity near the surface in the unstable case than in the neutral case. As a result, the unstable case gave better ventilation than the neutral case with regard to ventilation solely at local near-surface wind speed. This was not related to any building effect and only reflected the change due to differences in stratification.

Usually, ventilation within the city is quantified using the velocity ratio

$$V_r = \frac{V_{2\mathrm{m}}}{V_{\mathrm{ref}}}, \tag{3}$$

where V_{ref} denotes a reference velocity often defined as $\left| \overline{\overline{v}_h} \right|$ at a height well above the city area [2,10]. However, this definition of V_{ref} resulted in a higher V_r in the unstable case than in the neutral case according to general differences in the vertical distribution of horizontal wind speed (higher wind speed near the surface, lower wind speed within the boundary layer in the unstable case than in

the neutral case, cf. Figure 4). This effect made it extremely difficult to detect and analyze the separate effects of the buildings on V_r for the different stratifications. To eliminate this trivial, purely stratification-related difference between the two cases, V_{ref} was redefined as $V_{2\mathrm{m}}$ calculated over the flat surface in front of the city area.

This adapted definition of V_r excluded the differences in vertical profiles between both cases, as now $V_{2\mathrm{m}}$ and V_{ref} are both calculated at the same height level within and outside the city region. Consequently, only differences in ventilation caused by the buildings under different stratification were emphasized. A $V_r < 1$ indicated reduced wind speed (low ventilation), while $V_r > 1$ was related to a higher wind speed (high ventilation) compared to that outside the city.
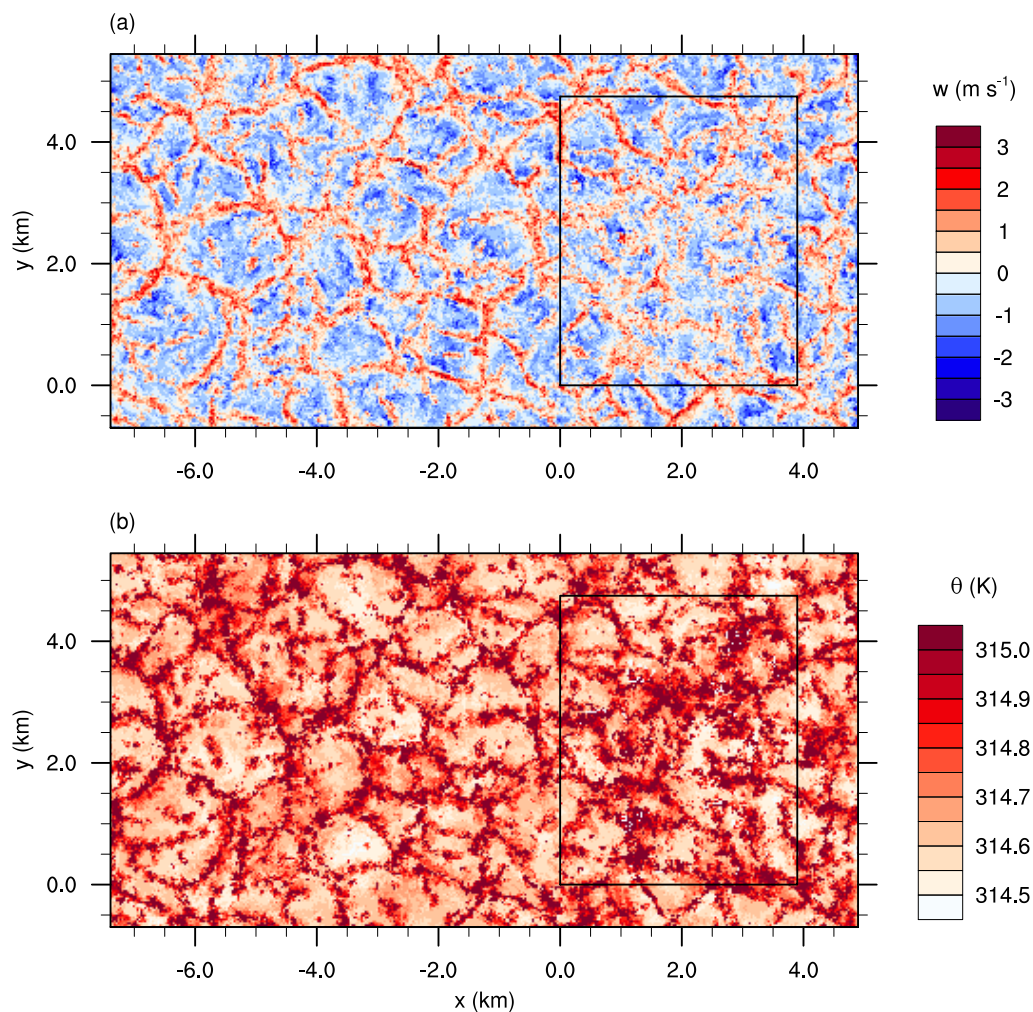

Figure 2. Instantaneous vertical wind velocity (**a**) and potential temperature (**b**) for the unstable case after a simulation time of 6 h at a height of 100 m. The solid inner rectangle marks the city area.
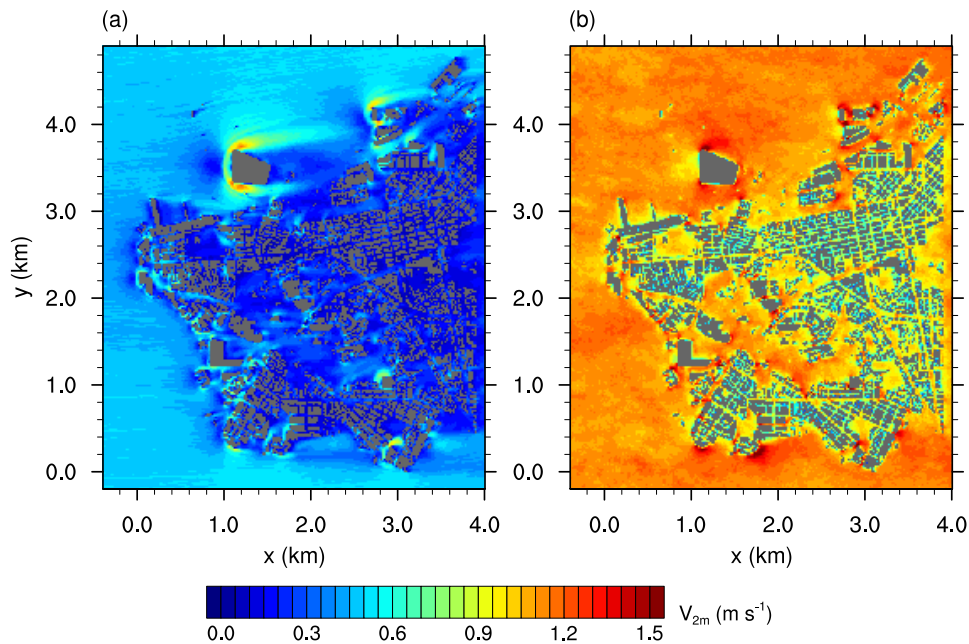
Figure 3. Averaged three-dimensional wind velocity at 2 m height for the (**a**) neutral case and (**b**) unstable case. Buildings are shown in gray.
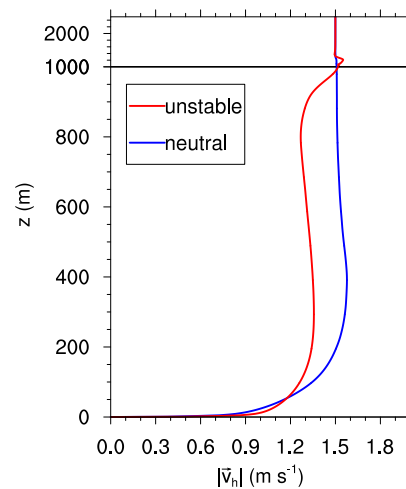

Figure 4. Vertical profile of the wind speed of the mean horizontal wind vector $|\vec{v}_h|$ within the recycling area.

Figure 5a,b shows the newly defined V_r for the neutral and unstable cases, respectively. In the neutral case, V_r was significantly less than 1 within the city area. The low V_r, which was related to a decrease in V_{2m} between the surroundings and the city, resulted from the buildings that were blocking the airflow within the city area. However, at the corners of exposed buildings, V_r increased as the air was forced to move around the buildings, which was consistent with well-known flow patterns around bluff bodies (e.g., [25]). In the unstable case (Figure 5b), such local influences of the buildings on V_r were significantly reduced in general, resulting in a more uniform distribution of V_r throughout the domain analyzed. Areas of high V_r in the neutral case still showed $V_r > 1$ in the unstable case, but the magnitude of the increase in V_r was significantly lower (e.g., at the edges of the large building complex at position $(x, y) = (1.2 \text{ km}^2, 3.6 \text{ km}^2)$).
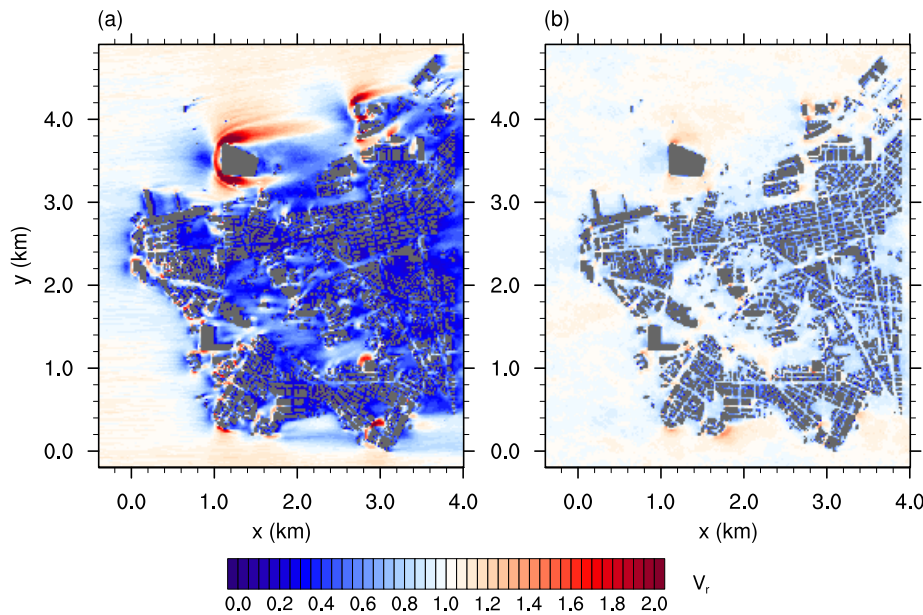
Figure 5. Velocity ratio V_r for the (**a**) neutral case and (**b**) unstable case.

A better view of the differences in V_r is shown in Figure 6, which shows the normalized velocity ratio

$$V_{r,\text{norm}} = \frac{V_r(\text{unstable})}{V_r(\text{neutral})}. \tag{4}$$

Within the city, V_r was up to four times higher in the unstable case than in the neutral case. However, at the edges of the exposed buildings and at the windward edge of the city, V_r was only about 0.6 times its value in the neutral case. In the neutral case, the buildings blocked the airflow and forced the air to circulate around them horizontally. For reasons of continuity, the air was accelerated at the edges and decelerated at the leeward side of the buildings. In the unstable case, however, stratification made it much easier for the blocked air to flow over the buildings. This significantly reduced the air volume that was forced around the buildings, thereby preventing a strong increase in V_r around the exposed buildings. Furthermore, the enhanced vertical exchange in momentum due to convection led to higher V_r at the leeward side of these buildings and was also responsible for the strong increase in V_r within the city. The average V_r was about twice as high in the unstable case than in the neutral case.

The increase in V_r within the city area for the unstable case compared to the neutral case was also found by Yang and Li [13], who reported that flow rates through street canyons were higher in an unstable stratified atmosphere compared to those under conditions of neutral stratification. However, the reduction of V_r in the vicinity of exposed buildings was not reported, which was because Yang and Li [13] only used a very simplified building setup that did not include exposed buildings.

Further effects of a change in stratification on the ventilation could be derived from correlations of V_r with different building parameters. Figure 7a,b shows the scatter plot for V_r and the average building height H_{avg} and for V_r and the plan area index λ_p (building area divided by total area), respectively. For this, the city was divided into non-overlapping $100\,\text{m} \times 100\,\text{m}$ patches. The data points represent the average values within each of the patches. Data for the neutral and unstable cases are depicted by blue dots and red crosses, respectively.

Figure 7 shows that $V_r(\text{unstable}) > V_r(\text{neutral})$ as most data points for the neutral case lay within 0.1 and 0.7, while, for the unstable case, the majority of data points were within 0.5 and 1.1. However, no significant correlation was found between H_{avg} and V_r (Figure 7a). For both stratifications,

the coefficient of determination is $R^2 < 0.1$. This means that H_{avg} had almost no influence on V_r in the neutral or unstable case. By contrast, Hang et al. [26] observed higher wind speed in a tall idealized building array compared to a shallower building array considering neutral stratification. The dependency found by Hang et al. [26] was related to perfectly aligned buildings channeling the flow within the idealized building arrays. In this case, higher buildings improved the channeling effect as a larger air volume was blocked at the front of the building array and forced into the streets. This effect was not observed in the simulations in this study, in which streets were randomly aligned to the wind direction.
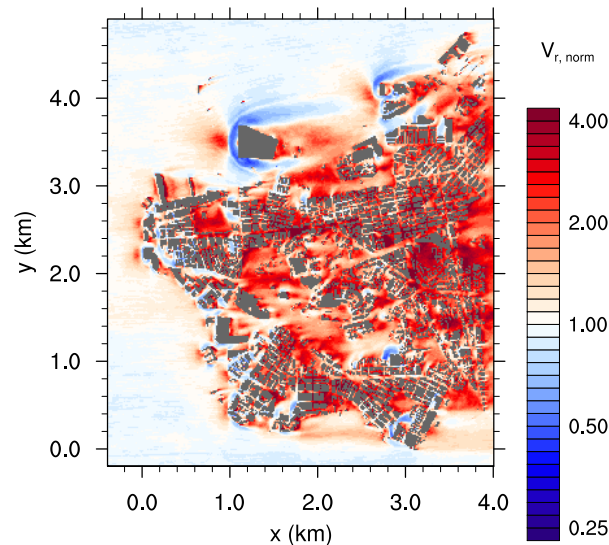

Figure 6. Normalized velocity ratio $V_{r,\text{norm}}$. Values above 1 indicate higher V_r in the unstable case, while values below 1 indicate higher V_r in the neutral case.

Figure 7b shows the scatter plot for V_r and λ_p. In the neutral and unstable cases, V_r and λ_p show a negative correlation. This was also reported by Hang et al. [26] for the neutral case. An area with high λ_p described a dense built-up area with narrow streets where the wind velocity was significantly reduced resulting in a low V_r. By contrast, a mostly open-space area, where λ_p was low, had less influence on the wind field and therefore V_r was high in such areas.

However, determination of the correlation varied between the neutral case and the unstable case. In the neutral case, the correlation was weak as V_r showed a high level of variation for a specific λ_p. This resulted in a low R^2 of 0.104. In the unstable case, the impact of λ_p on ventilation was significantly higher than in the neutral case as R^2 was 0.511, which resulted from less variation in V_r for a given λ_p.

This difference in correlation between the two cases can be explained when considering the influence of the wind direction. In the neutral case, the ventilation was highly dependent on the orientation of the wind direction with regard to the orientation of the streets [27]. The wind direction changed only slightly at a given point in the neutral case. Figure 8 shows representative measurements of wind direction for both cases at position $(x, y) = (2713 \, \text{m}, 2671 \, \text{m})$, which is the center of a street crossing within the city center. The wind direction varied between 54° and 188° for the neutral case, while the wind came from all directions in the unstable case. At the same time, the orientation of the streets within Kowloon was heterogeneous, with many patches existing with the same λ_p but different street orientations. Therefore, in the neutral case, some patches experienced good ventilation as their streets were oriented favorably for the given wind direction, while other patches constantly experienced unfavorable winds and therefore were poorly ventilated. Therefore, V_r varied markedly in the neutral case for a given λ_p. As stated above, in the unstable case, ventilation was dominated

by vertical mixing. Due to the strong convective motions and low background wind speed, the wind direction changed frequently (Figure 8). Therefore, the actual orientation of streets according to the wind direction was less important in the unstable case than in the neutral case. The main parameter determining the ventilation for the unstable case was therefore the amount of void space where convective motions could develop. This was related to λ_p, as it gave the ratio of occupied area to the total area. As $R^2 > 0.5$, λ_p was the key parameter determining the ventilation for the unstable case.
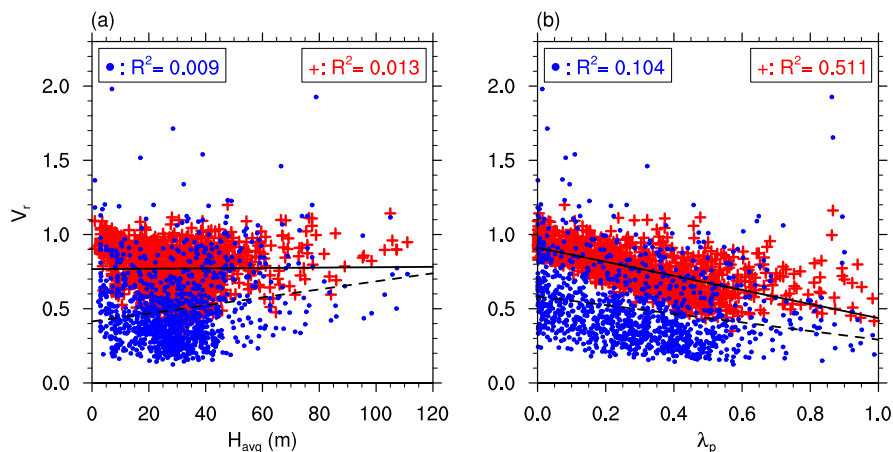

Figure 7. Scatter plot for V_r and (**a**) the average building height H_{avg} and (**b**) the plan area index λ_p. Each point represents an average value inside a $100\,\text{m} \times 100\,\text{m}$ area within the city. Blue dots represent the neutral case and red crosses represent the unstable case.
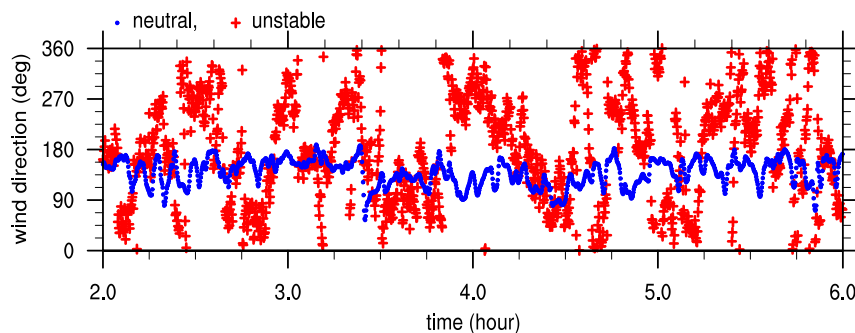

Figure 8. Time series of wind direction at position $(x, y) = (2713\,\text{m}, 2671\,\text{m})$ in the city center. Blue dots represent the neutral case and red crosses represent the unstable case.

4. Conclusions

This study compared ventilation in Kowloon City, Hong Kong, under conditions of neutral and unstable atmospheric stratification. For the comparison, a summer weak-wind situation with a geostrophic wind of $1.5\,\text{m}\,\text{s}^{-1}$ was chosen, as this condition was also the primary target of AVAs for Kowloon City.

An alternative definition of ventilation via the velocity ratio V_r was presented. The standard definition considers the vertical distribution of wind velocity, and therefore depends on the stratification. The new definition neglected this vertical distribution and purely focused on the impact of obstacles under conditions of varying stratification, as it was directly calculated from the reduction of the wind velocity due to blockage of airflow by buildings. This enabled a better comparison of the influence of building on ventilation under different stratification conditions.

The averaged ventilation in the unstable case was about double that in the neutral case. This was due to the large convective eddies in the unstable case, which created a high degree of variation in wind direction and strong up- and downdrafts. The strong vertical motions reduced the decelerating impact of buildings on the flow field, as it was easier for the air to flow over them. However, this also reduced acceleration effects at the side edges of exposed buildings, which appeared in the neutral case. In these areas, V_r was reduced to 0.6 times its value in the neutral case. Consequently, considering only neutral stratification when analyzing the ventilation of a city area was insufficient, as the ventilation appeared to be significantly changed, positively and negatively, under conditions of unstable stratification.

A linkage between the plan area index λ_p and V_r was found similar to other studies for neutral stratification where low V_r corresponds to high λ_p. However, the correlation between both variables was stronger in the unstable case than in the neutral case. In the neutral case, the correlation was reduced because, apart from λ_p, the orientation of the buildings in relation to the wind direction also influenced ventilation. In the unstable case, no distinct wind direction was present as it changed frequently due to the convective motions. This led to a smaller influence of the building orientation and a greater influence of λ_p on ventilation. Therefore, for cities where convective low-wind conditions are often present, such as Hong Kong, city planning should focus more on reducing λ_p to improve city ventilation than on the orientation of buildings and streets.

In contrast to other studies, no correlation was found between the average building height H_{avg} and V_r. As these other studies only focused on idealized homogeneous block arrays, it is possible that the idealized cases overestimated the channeling induced by these idealized building arrays.

The results of this study indicated that AVAs should not focus purely on neutral stratification but should also consider unstable stratification, particularly when these conditions in combination with low wind speed are observed frequently, as in Hong Kong. When focusing on summer weak-wind conditions, a complete view on the ventilation of a city area can only be obtained if both neutral and unstable stratification are included in the analysis. For strong-wind conditions, the influence of mechanically induced turbulence may become stronger than that of thermally induced turbulence, which was already found by Yang and Li [13] for a very simplified city case.

The impact of stable stratification was not covered in this study but should be examined in future analyses. The first inspection of the impact of stable stratification on ventilation was made by Yang and Li [13] for a simplified city case. However, these results should be tested with a more realistic setup. The results of this study revealed differences between a simple building case and a more realistic setup for unstable stratification. Therefore, it is possible that results would also differ for a stable case with a more sophisticated building setup.

Surface elevation and land cover were neglected in this study to extract the pure influence of buildings on ventilation under different stratification conditions. Recent studies by Wolf-Grosse et al. [28] and Ronda et al. [18], however, showed the importance of topographic effects and consideration of water bodies at city scale. Therefore, these effects will be considered in a follow-up study, focusing on their combined influence on ventilation. In particular, the difference in land cover with resulting heterogeneous surface heat flux may have a large impact on ventilation as this leads to small-scale secondary circulations, such as sea breeze. A further step towards reality will also be to use an urban surface model available in PALM [29,30], which allows to accurately calculate surface temperatures based on a building-energy-balance model.

Appendix A

A grid sensitivity study was conducted to determine an appropriate grid width for the main simulations. Four simulations with grid sizes Δ of 1 m, 2 m, 4 m, and 8 m were compared. The domain used in the sensitivity study included 1 km^2 of Kowloon City. Cyclic boundary conditions and neutral stratification were used. As turbulent structures are generally larger in the unstable case than in the neutral case, the latter defined the minimum grid size to be used.

Figure A1 depicts the cumulative distribution function of the 1 h averaged 3-dimensional wind velocity $V = \sqrt{u^2 + v^2 + w^2}$ at a height of 4 m for each simulation. Due to differences in grid level height between the simulations, data were linearly interpolated to $z = 4$ m. Significant differences in the distribution of V could be observed between 2 m, 4 m and 8 m grid sizes. The distribution of low V decreased if a smaller grid size was used. The test statistic $A(a, b)$ of Kuiper's test [31], where $A(a, b)$ compares the distribution function of case a to that of case b, yields $A(8, 4) = 0.11$, $A(4, 2) = 0.10$, and $A(2, 1) = 0.06$. Thus, the distribution of V changed significantly less if the grid size was reduced from 2 m to 1 m compared to a reduction from 8 m to 4 m or from 4 m to 2 m. Consequently, a reduction of grid size from 2 m to 1 m only slightly improved the quality of the representation of the wind field within the city. As a reduction of the grid size by a factor of 2 increased the computational load by a factor of 16 (double the grid points in each dimension multiplied by 2 for double the amount of time steps needed), a grid size of 2 m was selected for the main simulations as a compromise between accuracy and computational cost.
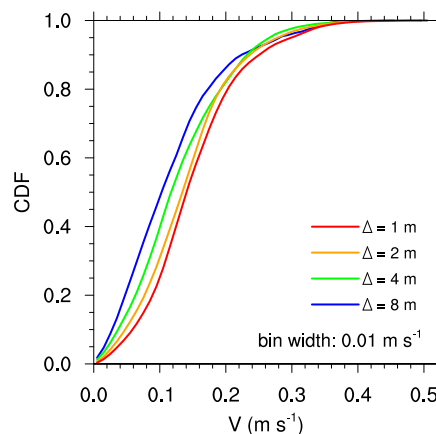
Figure A1. Cumulative distribution function of three-dimensional wind velocity V at 4 m height. Data are averaged over 1 h.

References

1. Xie, X.; Huang, Z.; Wang, J.S. Impact of building configuration on air quality in street canyon. *Atmos. Environ.* **2005**, *39*, 4519–4530.
2. Ng, E. Policies and technical guidelines for urban planning of high-density cities—Air ventilation assessment (AVA) of Hong Kong. *Build. Environ.* **2009**, *44*, 1478–1488.

3.   Ng, E.; Yuan, C.; Chen, L.; Ren, C.; Fung, J.C.H. Improving the wind environment in high-density cities by understanding urban morphology and surface roughness: A study in Hong Kong. *Landsc. Urban Plan.* **2011**, *101*, 59–74.

4.   Cheng, Y.; Lien, F.; Yee, E.; Sinclair, R. A comparison of large Eddy simulations with a standard k–ϵ Reynolds-averaged Navier–Stokes model for the prediction of a fully developed turbulent flow over a matrix of cubes. *J. Wind Eng. Ind. Aerodyn.* **2003**, *91*, 1301–1328.

5.   Ashie, Y.; Kono, T. Urban-scale CFD analysis in support of a climate-sensitive design for the Tokyo Bay area. *Int. J. Climatol.* **2011**, *31*, 174–188.

6.   Tominaga, Y. Visualization of city breathability based on CFD technique: Case study for urban blocks in Niigata City. *J. Vis.* **2012**, *15*, 269–276.

7.   Yang, L.; Li, Y. City ventilation of Hong Kong at no-wind conditions. *Atmos. Environ.* **2009**, *43*, 3111–3121.

8.   Yim, S.H.L.; Fung, J.C.H.; Lau, A.K.H.; Kot, S.C. Air ventilation impacts of the "wall effect" resulting from the alignment of high-rise buildings. *Atmos. Environ.* **2009**, *43*, 4982–4994.

9.   Yuan, C.; Ng, E.; Norford, L.K. Improving air quality in high-density cities by understanding the relationship between air pollutant dispersion and urban morphologies. *Build. Environ.* **2014**, *71*, 245–258.

10.   Letzel, M.O.; Helmke, C.; Ng, E.; An, X.; Lai, A.; Raasch, S. LES case study on pedestrian level ventilation in two neighbourhoods in Hong Kong. *Meteorol. Z.* **2012**, *21*, 575–589.

11.   Park, S.B.; Baik, J.J.; Lee, S.H. Impacts of mesoscale wind on turbulent flow and ventilation in a densely built-up urban area. *J. Appl. Meteorol. Climatol.* **2015**, *54*, 811–824.

12.   Park, S.B.; Baik, J.J. A Large-Eddy Simulation Study of Thermal Effects on Turbulence Coherent Structures in and above a Building Array. *J. Appl. Meteorol. Climatol.* **2013**, *52*, 1348–1365.

13.   Yang, L.; Li, Y. Thermal conditions and ventilation in an ideal city model of Hong Kong. *Energy Build.* **2011**, *43*, 1139–1148.

14.   Raasch, S.; Schröter, M. PALM-A large-eddy simulation model performing on massively parallel computers. *Meteorol. Z.* **2001**, *10*, 363–372.

15.   Maronga, B.; Gryschka, M.; Heinze, R.; Hoffmann, F.; Kanani-Sühring, F.; Keck, M.; Ketelsen, K.; Letzel, M.O.; Sühring, M.; Raasch, S. The Parallelized Large-Eddy Simulation Model (PALM) version 4.0 for atmospheric and oceanic flows: Model formulation, recent developments, and future perspectives. *Geosci. Model Dev.* **2015**, *8*, 2515–2551.

16.   Lo, K.W.; Ngan, K. Characterising the pollutant ventilation characteristics of street canyons using the tracer age and age spectrum. *Atmos. Environ.* **2015**, *122*, 611–621.

17.   Park, S.B.; Baik, J.J.; Ryu, Y.H. A Large-Eddy Simulation Study of Bottom-Heating Effects on Scalar Dispersion in and above a Cubical Building Array. *J. Appl. Meteorol. Climatol.* **2013**, *52*, 1738–1752.

18.   Ronda, R.; Steeneveld, G.; Heusinkveld, B.; Attema, J.; Holtslag, B. Urban fine-scale forecasting reveals weather conditions with unprecedented detail. *Bull. Am. Meteorol. Soc.* **2017**, doi:10.1175/BAMS-D-16-0297.1.

19.   Lund, T.S.; Wu, X.; Squires, K.D. Generation of Turbulent Inflow Data for Spatially-Developing Boundary Layer Simulations. *J. Comput. Phys.* **1998**, *140*, 233–258.

20.   Kataoka, H.; Mizuno, M. Numerical flow computation around aeroelastic 3D square cylinder using inflow turbulence. *Wind Struct.* **2002**, *5*, 379–392.

21.   Orlanski, I. A simple boundary condition for unbounded hyperbolic flows. *J. Comput. Phys.* **1976**, *21*, 251–269.

22.   Miller, M.J.; Thorpe, A.J. Radiation conditions for the lateral boundaries of limited-area numerical models. *Q. J. R. Meteorol. Soc.* **1981**, *107*, 615–628.

23.   Gryschka, M.; Fricke, J.; Raasch, S. On the impact of forced roll convection on vertical turbulent transport in cold air outbreaks. *J. Geophys. Res. Atmos.* **2014**, *119*, 12513–12532.

24.   Atkinson, B.W.; Wu Zhang, J. Mesoscale shallow convection in the atmosphere. *Rev. Geophys.* **1996**, *34*, 403–431.

25.   Larousse, A.; Martinuzzi, R.; Tropea, C. Flow Around Surface-Mounted, Three-Dimensional Obstacles. In Proceedings of the Turbulent Shear Flows 8: Selected Papers from the Eighth International Symposium on Turbulent Shear Flows, Munich, Germany, 9–11 September 1991; Durst, F., Friedrich, R., Launder, B.E., Schmidt, F.W., Schumann, U., Whitelaw, J.H., Eds.; Springer: Berlin/Heidelberg, Germany, 1993; pp. 127–139.

26.   Hang, J.; Li, Y.; Sandberg, M. Experimental and numerical studies of flows through and within high-rise building arrays and their link to ventilation strategy. *J. Wind Eng. Ind. Aerodyn.* **2011**, *99*, 1036–1055.

27.   Kim, J.J.; Baik, J.J. A numerical study of the effects of ambient wind direction on flow and dispersion in urban street canyons using the RNG k-e turbulence model. *Atmos. Environ.* **2004**, *38*, 3039–3048.

28. Wolf-Grosse, T.; Esau, I.; Reuder, J. Sensitivity of local air quality to the interplay between small- and large-scale circulations: A large-eddy simulation study. *Atmos. Chem. Phys.* **2017**, *17*, 7261–7276.

29. Resler, J.; Krč, P.; Belda, M.; Juruš, P.; Benešová, N.; Lopata, J.; Vlček, O.; Damašková, D.; Eben, K.; Derbek, P.; et al. A new urban surface model integrated in the large-eddy simulation model PALM. *Geosci. Model Dev. Discuss.* **2017**, *2017*, 1–26.

30. Yaghoobian, N.; Kleissl, J.; Paw, U.K.T. An Improved Three-Dimensional Simulation of the Diurnally Varying Street-Canyon Flow. *Bound.-Layer Meteorol.* **2014**, *153*, 251–276.

31. Kuiper, N.H. Tests concerning random points on a circle. *Indag. Math.* **1960**, *63*, 38–47.

6 Concluding Remarks

6.1 Summary

The aim of this thesis was to improve the quality of urban ventilation assessments (UVAs). UVAs are a key instrument to evaluate urban ventilation and to identify poorly ventilated city areas. Well ventilated cities are a crucial part to ensure a high health quality of city dwellers by reducing the exposure to potentially health-threatening pollution. If used during the planning phase of new constructions, poorly ventilated areas can be avoided before being created.

Due to the high complexity of the urban canopy layer, UVAs are incapable to consider every detail, and are, hence, forced to simplify the reality. However, some details can prove to be crucial for the urban ventilation and should not be neglected. Within this thesis, urban ventilation on two different scales were investigated: the building scale and the neighbourhood scale. On the building scale, the influence of lateral courtyard openings on the courtyard ventilation was investigated. The aim was to analyse the change in maximum concentration and in residence time scales of pollutants within courtyards if lateral openings are considered. On the neighbourhood scale, the focus was the influence of atmospheric stratification on the correlation between city ventilation and the mean properties of the building array. Particularly, it was investigated if the impact of mean building height on the ventilation varies between a neutral strong-wind case and a weak-wind unstably stratified scenario. Also, the correlation between building density (plan area index) and ventilation under neutral and unstable stratification was analysed.

All studies applied large-eddy simulations (LES) using the LES model PALM. LES has the advantage over real-world measurements and wind-tunnel experiments, that data can be monitored at every grid point of the simulation. The LES technique was chosen over other computational-fluid dynamics (CDF) methods, because LES allows to directly simulate the effect of large-scale turbulence while also covering the entire atmospheric boundary layer.

At first, a model evaluation was conducted to confirm that PALM is capable to represent the complex flow field within a built-up urban area. In the evaluation study, the flow through a built-up urban area was simulated and compared against wind-tunnel measurements conducted in the Environmental Wind Tunnel Laboratory (EWTL) facility 'Wotan' at the University of Hamburg. The built-up area represented a real-case building array of the HafenCity in Hamburg, Germany. Because a realistic building setup was simulated, a variety of different flow regimes could be tested in a single simulation including street canyons of different orientation and width, crossings, as well as fairly isolated buildings. A neutral stratification was considered. Non-neutral stratification is still difficult to obtain within wind-tunnel studies and was therefore not covered by the evaluation study. Measurements were conducted at different positions throughout the building array and the measured statistics were compared between both, the wind-tunnel experiment and the PALM simulation. Besides mean wind speed and direction, also higher order statistics including variants, skewness and excess kurtosis were compared as well as turbulence intensities, length scales and the spectral energy-density distribution. The comparison showed an overall very good agreement between the PALM results and the wind-tunnel measurements. This was verified using different validation metrics following the recommendations of Schatzmann et al. (2010). All considered metrics were well within the acceptable margins. On closer investi-

gation, however, it was found that PALM tends to overestimate the turbulence close to the surface and obstacles. This led to an underestimation of mean wind speed in the vicinity of solid surfaces. Two main reasons were identified causing these differences. The first was a discrepancy between the measurement heights between both experiments. Due to the grid layout of the PALM simulation, no grid points were available at the exact same heights as in the wind-tunnel experiment. PALM measurements were situated $0.5\,\mathrm{m}$ below those of the wind-tunnel experiment. This height difference is of higher importance the closer the measurements are to the surface due to the high vertical mean gradients. The height difference could be accounted for up to $3\,\%$ wind-speed deficit within the lowest evaluation level that was at $3\,\mathrm{m}$ height. The second reason for the lower wind speed was an overestimation of the surface roughness caused by the chosen roughness length z_0 and the building representation. Because the exact value of z_0 of the surfaces in the wind-tunnel experiment was unknown, it was estimated that $z_0 = 0.01\,\mathrm{m}$. Other wind-tunnel experiments conducted at the EWTL, using comparable obstacle materials and model scale, reported roughness lengths between $0.002\,\mathrm{m}$ and $0.01\,\mathrm{m}$ (B. Leitl, personal communication, March 12, 2021). Hence, the chosen z_0 is still within a reasonable range, but might be at the upper end of the scale. Also, the building representation on PALM's computational grid introduced additional roughness. If buildings are not aligned with the grid, smooth walls are transformed into a rougher step-wise representation in the simulation which is a disadvantage of the pure rectilinear grid used by PALM. The combined effect of the larger roughness and high z_0 resulted in a mean wind-speed deficit of $9\,\%$ at the lowest analysis height. Despite the difference between the wind-tunnel experiment and the PALM simulation, PALM still performed well within the acceptable margins and was found to be suitable to correctly reproduce all relevant flow features inside a complex urban environment.

For urban ventilation assessments focusing on building-scale ventilation and pollutant dispersion, even small-scale building features may be of high importance. Lateral openings of courtyards are only a few metres wide. However, they can significantly alter ventilation patterns inside courtyard cavities. Hall et al. (1999) analysed the pollutant removal from courtyards through lateral openings by means of wind-tunnel experiments. They found that, in an undisturbed approaching flow, openings can either worsen or improve the pollutant removal from the courtyards, depending on the orientation of the opening in relation to the mean wind direction. However, in a real-case scenario, courtyards are part of a complex urban building array with significantly different flow regimes compared to an undisturbed approaching flow. Also, in a real city case, pollutants are more often released outside of courtyards. Therefore, a study was conducted by means of LES to analyse the pollutant dispersion from street canyons into courtyards through lateral openings.

Several courtyards were placed in an artificial building array, that allowed to consider several orientations of the openings with respect to the main wind direction. Also, the arrangement of the courtyards allowed to distinguish between buildings placed at the windward end, the centre or the leeward end of a street, where different flow regimes inside the street canyon developed. Lastly, also the aspect ratio (AR, height-to-width ratio) of the courtyards was altered between 0.3 (wide courtyards) and 3 (deep courtyards). In total, 32 different courtyard configurations were analysed using three simulations. The focus lied on the pollutant dispersion into courtyards. Hence, pollutants were released along the streets resembling pollution by traffic. Besides pollutant concentration also the residence time is important to evaluate potential health risks (Beelen et al., 2014; Shah et al., 2015). To analyse the residence time of pollutants inside the courtyards, PALM's Lagrangian particle model (LPM) was applied and single particles were tracked.

The analysis of residence time showed that for aspect ratios of 1 or 0.3, courtyards with lateral openings were equally ventilated as closed courtyards. Wide courtyards were mainly

ventilated through the wide top opening and the influence of the relatively small lateral opening did not alter the residence times. For courtyards with an aspect ratio of 1, most lateral openings did not alter the ventilation patterns within the courtyard cavities, and hence, no influence was observed on the residence times. The only exception was the case where the courtyards were placed at the windward end of the street canyons with the opening placed at the windward wall (case "W front"). In this case, the oncoming wind was able to penetrate the courtyard cavity through the lateral opening unhindered. The re-circulation inside the courtyard was shifted upwards. As a result, detrainment of pollutants near the surface out of the cavity was reduced leading to longer residence times of pollutant particles for this courtyard setup.

For deep courtyards, the influence on the ventilation by openings was found to be more complex. While most opened courtyards showed comparable residence times to closed court-yards, those with openings positioned perpendicular to the wind direction and those with a leeward positioned opening at the end of a street canyon showed two peaks in the residence-time distribution. The majority of particles showed a long residence time, indicating a poor ventilation of the courtyard cavities. The secondary peak of the residence-time distribution, that was observed in some of the courtyards, was at short residence times. This points towards intermittent mixing events that transport pollutants quickly out of the cavities. These intermittent mixing events were also observed in the scalar time series recorded inside the courtyards. A detailed investigation on this phenomenon, however, was left for future studies.

To inspect the transport of pollutants from street canyons into the courtyards, the pollutant flux through the lateral and top openings were monitored. Deep courtyards showed entrainment of pollutants through the lateral opening for all considered cases. Inside deep courtyards, only a weak circulation was present close to the surface compared to the street-canyon flow. Pollutant-rich air could easily penetrate the courtyard cavity through the lateral openings, especially when the opening was situated at the windward walls of the buildings at the windward end of a street canyon. Due to the large entrainment, opened courtyards also showed significantly larger mean concentrations and experienced high-concentration events more often compared to closed courtyards.

Courtyards with an aspect ratio of 1 also showed a mean entrainment through the lateral opening except for those buildings placed at the centre and leeward end of the street having an opening at the windward wall. In these cases, the re-circulation inside the courtyard cavity and the street canyon in front of the opening promote a detrainment through the lateral opening. The mean concentration for these cases were similar to those of the closed courtyards.

Wide courtyards exhibited only minor influences on mean concentration and high-concentration events. Again, the strongest influence was found for the case where the approaching flow could directly enter the courtyard through the windward opening.

In all cases, lateral openings increased the pollutant concentration. The amount of the increase depends on the positioning of the courtyard along the street and the positioning of the opening in relation to the mean wind direction. Lateral openings impose only minor changes in pollutant concentration and ventilation behaviour for wide courtyards, but have a high impact on the ventilation and pollutant dispersion inside deep courtyards. Urban ventilation assessments should, hence, include courtyard openings if pollutant dispersion is focused on the building scale or the neighbourhood scale.

Moving from the building scale to the city scale, details of individual buildings become less important to the ventilation of entire city quarters, but the mean building properties like mean building height or building density correlate with ventilation. These correlations were found for neutral stratification (Hang et al., 2011). However, several studies found that ventilation patterns through built-up areas change significantly under unstable stratification

(Yang and Li, 2011; Park et al., 2013). To investigate if the correlation between mean building parameters and ventilation is also influenced by the stratification, simulations of Hong Kong City were conducted for neutral and unstable stratification. Differences in ventilation between both situations were analysed based on the velocity ratio V_r. In order to compare V_r for different stratification, a new definition was required that is not influenced by the vertical wind-speed distribution. Instead of defining the reference wind speed at a height of $500\,\mathrm{m}$, the wind speed at $2\,\mathrm{m}$ height (pedestrian height level) in a non-obstructed area outside of the city was used as reference for V_r. This definition only accounts for the wind-speed change caused by buildings but neglects any variation in height distribution.

Under unstable conditions, the mean ventilation improved by a factor of two inside the entire city area. This was attributed to the increased vertical mixing which mitigated the velocity reduction by the blocking effect of the buildings. However, increased vertical mixing also reduced V_r in areas where strong corner flows occurred under neutral stratification. The reduction was up to $40\,\%$ in these areas. This showed the general influence of stratification on city ventilation and agreed with the findings of Yang and Li (2011) and Park et al. (2013).

The mean building height H_avg and the plan area index λ_p, as a measure of building density, were correlated with V_r. No correlation could be found between V_r and H_avg under neutral or unstable stratification. This is in contrast to other studies that focused on idealized homogeneous building arrays. The influence of H_avg might be overestimated by idealized building arrays because of the strong channelling of air through the perfectly aligned street canyons in such cases.

Under neutral stratification, the detected correlation between V_r and λ_p was only weak with a correlation coefficient of $R^2 = 0.104$. Ventilation decreased only slightly with increasing λ_p. In case of unstable stratification, however, the correlation coefficient increased to $R^2 = 0.511$. The influence of λ_p on the ventilation was attributed to the higher variation in wind direction. In the neutral case, only small variations in wind direction were observed. If wind came from an unfavourable direction, an area was only poorly ventilated. Because of the convective motions, and hence, a stronger variation in wind direction, wind from all directions ventilate the area. This reduces the impact on direction and increases the importance of the direction-independent plan area index.

In conclusion, urban ventilation assessments should consider different stratification. If ventilation is only analysed for neutral stratification, the mean ventilation might be underestimated. For conservative estimates, this might be acceptable. However, areas with high ventilation under neutral stratification also showed reduced ventilation by up to $40\,\%$ under unstable stratification. This reveals that a complete estimate of the ventilation potential of a built-up area can only be made if neutral and unstable stratification are considered.

6.2 Outlook

This thesis was aimed to improve the understanding of urban ventilation. Urban ventilation assessments profit from the findings because courtyard ventilation and the interaction between ventilation and mean building parameters are better understood. Consequences of neglecting courtyard openings and atmospheric stratification can be better estimated. However, certain questions arose from the findings of the presented studies which should be covered in future studies.

The evaluation study, presented in Section 3, revealed an overestimation of the roughness compared to the wind-tunnel experiments which was partly attributed to the building representation on the simulation grid. In a future study, this should be further investigated. The influence of non-aligned building walls on the roughness could be analysed by simulating the flow around a simple single cube-shaped building under different orientation of the

walls in relation to the grid layout. Measurements at multiple distances to the walls could be compared to the many reference wind-tunnel and simulation experiments available in the literature (e.g. Hussein and Martinuzzi, 1996; Nozawa and Tamura, 2002; Letzel et al., 2008).

In Section 4, intermittent mixing events were found for deep courtyards, that also influenced the residence times of pollutants. The cause of these intermittent mixing events, however, could not be identified. As residence time is of importance when focusing on health-risking pollutants, understanding the nature of mixing events is crucial to adequately assess air quality in courtyard cavities. Regarding health risks, also the pollutant concentration and the residence time should be connected, which could not be achieved in the presented study. Connecting concentration and the residence time should give a better insight if large amount of pollutants reside for long time periods within courtyard cavities. This is especially important if slow-reacting chemical components are studied that may transform into health-threatening pollutants. A strategy to couple residence time and pollutant concentration is to simulate pollutants using Lagrangian particles. These particles must be released inside the street canyons. The concentration could be calculated by the concentration of particles inside the courtyards, and the residence time is measured by tracking the particles like it was already done in the presented study. This, however, requires a large amount of released particles. Hence, a smaller simulation domain compared to the one used in the presented study, might have to be used.

Multiple studies revealed the importance of the building layout on the ventilation properties (e.g., Assimakopoulos et al., 2003; Xie et al., 2005; Kurppa et al., 2018). The presented study, however, only covered the orientation of courtyard openings and different aspect ratios of the courtyards. Other parameters, like height and width of the openings or the thickness of the surrounding building, might be of importance for courtyard ventilation and should be featured in future studies.

Hall et al. (1999) showed that high vegetation like trees influence the ventilation patterns inside courtyards. In Section 4, it was shown that the influence of lateral openings on the ventilation strongly depends on the ventilation patterns in the courtyard cavity. Trees or other obstacles might therefore alter the influence of courtyard openings on the ventilation. Trees decouple the near-surface air flow and potentially trap pollutants below the tree crowns. Other obstacles like fences or cars introduce higher roughness inside the courtyards and cause reduced wind speed and mixing. Reduced mixing would decrease the transport of pollutants out of the courtyards but might also limit the transport of pollutants into the courtyards as well. Because obstacles like trees, fences, cars or even small buildings are often present inside courtyards, future studies should analyse the change in ventilation considering lateral openings and obstacles inside courtyards.

Ventilation patterns can significantly change under different atmospheric stratification, as shown in Section 5 and by, e.g. Park et al. (2015) and Yang and Li (2011). It is therefore very likely, that thermally induced turbulence also affects the influence of lateral openings on courtyard ventilation. During night time, the surrounding warm building walls still provide enough energy to heat up the air within the courtyards. The lateral openings in combination with the rising warm air from the courtyard cavities then cause a chimney effect drawing potentially polluted air from the street canyons into the courtyards. This should be confirmed by future studies.

Section 5 covered the influence of unstable stratification during a weak-wind scenario on the ventilation at neighbourhood scale, and showed that the ventilation differs compared to neutral stratification. Stable stratification, however, was not considered. Stable stratification often occurs during night time, when good ventilation is required to reduce night-time heat stress in summer. Yang and Li (2011) showed, that the ventilation behaviour differs also for stable stratification compared to neutral stratification. However, only a simplified building

case was considered. As shown in Section 5, results from a simple building setup can differ from findings derived from realistic building setups. Hence, the effects of stable stratification on ventilation found by Yang and Li (2011) cannot be directly transferred to realistic building configurations. Future studies are hence necessary to analyse the difference in ventilation behaviour of real-case city setups under neutral and stable atmospheric conditions.

In Section 5, a real-case building setup was used, but differences in surface materials, anthropogenic heat emissions, and radiation effects were neglected. These effects cause heterogeneously distributed heat emissions, that have a significant impact on the wind field and may trigger secondary circulations (Raasch and Harbusch, 2001). For example, Wolf-Grosse et al. (2017) and Ronda et al. (2017) showed the influence of nearby water bodies on the ventilation on city scale. Using advanced surface models and considering radiation effects, a more realistic heat distribution can be achieved in simulations. The effects of evolving small-scale secondary circulations, especially during weak-wind scenarios, might have an additional strong effect on the ventilation behaviour. These heterogeneous effects should be covered for different stratification by future studies.

Acknowledgements

I would like to close this thesis by thanking all who supported me during the last years. I thank Prof. Dr. Siegfried Raasch for his support throughout my PhD studies. I highly value the many opportunities he gave me to improve my scientific capabilities and programming skills. I also thank Prof. Dr. Edward Ng for the scientific discussions during the Hong Kong ventilation study. I thank my co-authors, Prof. Dr. Bernd Leitl, Dr. Frank Harms, Dr. Kerstin Surm, and Dr. Björn Maronga for the great collaboration during the evaluation study. Many thanks go to Dr. Matthias Sühring, not only for the great collaboration during our courtyard-ventilation study, but also for the many scientific and private discussions throughout the last years.

I like to thank all members of the PALM group. It was a great time working with all of you. Especially, I thank my office room-mates, Dr. Farah Kanani-Sühring and Katrin Gehrke, the "care-taking" office, for the many constructive discussions we had. Also, I like to thank Helge Knoop, Lennart Böske, Dr. Fabian Hoffmann, and Dr. Micha Gryschka for their mental and specialist support.

I thank Kathrin Graw, Helge Knoop and especially Dr. Matthias Sühring and Dr. Farah Kanani-Sühring for critical proofreading of this thesis. Also, I thank Prof. Dr. Siegfried Raasch, Prof. Dr. Felix Ament and Prof. Dr. Günter Groß for reviewing this thesis.

Lastly, I thank my family and my friends, including those already mentioned, who never got tired to support me.

Bibliography

Arakawa, A. and Lamb, V. R.: Computational Design of the Basic Dynamical Processes of the UCLA General Circulation Model, in: General Circulation Models of the Atmosphere, vol. 17, pp. 173–265, Methods in computational Physics, 1977.

Assimakopoulos, V., ApSimon, H., and Moussiopoulos, N.: A Numerical Study of Atmospheric Pollutant Dispersion in Different Two-Dimensional Street Canyon Configurations, Atmos. Environ., 37, 4037–4049, doi: 10.1016/S1352-2310(03)00533-8, 2003.

Bady, M., Kato, S., and Huang, H.: Towards the Application of Indoor Ventilation Efficiency Indices to Evaluate the Air Quality of Urban Areas, Build. Environ., 43, 1991–2004, doi: 10.1016/j.buildenv.2007.11.013, 2008.

Barlow, J. F.: Progress in Observing and Modelling the Urban Boundary Layer, Urban Clim., 10, 216–240, doi: 10.1016/j.uclim.2014.03.011, 2014.

Beelen, R., Raaschou-Nielsen, O., Stafoggia, M., Andersen, Z. J., Weinmayr, G., Hoffmann, B., Wolf, K., Samoli, E., Fischer, P., Nieuwenhuijsen, M., Vineis, P., Xun, W. W., Katsouyanni, K., Dimakopoulou, K., Oudin, A., Forsberg, B., Modig, L., Havulinna, A. S., Lanki, T., Turunen, A., Oftedal, B., Nystad, W., Nafstad, P., Faire, U. D., Pedersen, N. L., Östenson, C.-G., Fratiglioni, L., Penell, J., Korek, M., Pershagen, G., Eriksen, K. T., Overvad, K., Ellermann, T., Eeftens, M., Peeters, P. H., Meliefste, K., Wang, M., Bueno-de-Mesquita, B., Sugiri, D., Krämer, U., Heinrich, J., de Hoogh, K., Key, T., Peters, A., Hampel, R., Concin, H., Nagel, G., Ineichen, A., Schaffner, E., Probst-Hensch, N., Künzli, N., Schindler, C., Schikowski, T., Adam, M., Phuleria, H., Vilier, A., Clavel-Chapelon, F., Declercq, C., Grioni, S., Krogh, V., Tsai, M.-Y., Ricceri, F., Sacerdote, C., Galassi, C., Migliore, E., Ranzi, A., Cesaroni, G., Badaloni, C., Forastiere, F., Tamayo, I., Amiano, P., Dorronsoro, M., Katsoulis, M., Trichopoulou, A., Brunekreef, B., and Hoek, G.: Effects of Long-Term Exposure to Air Pollution on Natural-Cause Mortality: An Analysis of 22 European Cohorts within the Multicentre ESCAPE Project, Lancet, 383, 785–795, doi: 10.1016/S0140-6736(13)62158-3, 2014.

Blocken, B.: Computational Fluid Dynamics for Urban Physics: Importance, Scales, Possibilities, Limitations and Ten Tips and Tricks towards Accurate and Reliable Simulations, Build. Environ., 91, 219–245, doi: 10.1016/j.buildenv.2015.02.015, 2015.

Blocken, B. and Carmeliet, J.: Pedestrian Wind Environment around Buildings: Literature Review and Practical Examples, Journal of Thermal Env. and Bldg. Sci., 28, 107–159, doi: 10.1177/1097196304044396, 2004.

Blocken, B., Stathopoulos, T., and van Beeck, J.: Pedestrian-Level Wind Conditions around Buildings: Review of Wind-Tunnel and CFD Techniques and Their Accuracy for Wind Comfort Assessment, Build. Environ., 100, 50–81, doi: 10.1016/j.buildenv.2016.02.004, 2016.

Bo, M., Salizzoni, P., Clerico, M., and Buccolieri, R.: Assessment of Indoor-Outdoor Particulate Matter Air Pollution: A Review, Atmosphere, 8, 136, doi: 10.3390/atmos8080136, 2017.

Briscolini, M. and Santangelo, P.: Development of the Mask Method for Incompressible Unsteady Flows, J. Comput. Phys., 84, 57–75, doi: 10.1016/0021-9991(89)90181-2, 1989.

Britter, R. and Hanna, S. R.: Flow and Dispersion in Urban Areas, Annu. Rev. Fluid Mech., 35, 469–496, doi: 10.1146/annurev.fluid.35.101101.161147, 2003.

Buccolieri, R. and Hang, J.: Recent Advances in Urban Ventilation Assessment and Flow Modelling, Atmosphere, 10, 144, doi: 10.3390/atmos10030144, 2019.

Chen, L., Hang, J., Sandberg, M., Claesson, L., Di Sabatino, S., and Wigo, H.: The Impacts of Building Height Variations and Building Packing Densities on Flow Adjustment and City Breathability in Idealized Urban Models, Build. Environ., 118, 344–361, doi: 10.1016/j.buildenv.2017.03.042, 2017.

Cheng, Y., Lien, F., Yee, E., and Sinclair, R.: A Comparison of Large Eddy Simulations with a Standard k–ϵ Reynolds-Averaged Navier–Stokes Model for the Prediction of a Fully Developed Turbulent Flow over a Matrix of Cubes, J. Wind. Eng. Ind. Aerodyn., 91, 1301–1328, doi: 10.1016/j.jweia.2003.08.001, 2003.

Cheung, C. S. C. and Hart, M. A.: Climate Change and Thermal Comfort in Hong Kong, Int. J. Biometeorol., 58, 137–148, doi: 10.1007/s00484-012-0608-9, 2014.

Chew, L. W., Nazarian, N., and Norford, L.: Pedestrian-Level Urban Wind Flow Enhancement with Wind Catchers, Atmosphere, 8, 159, doi: 10.3390/atmos8090159, 2017.

Courant, R., Friedrichs, K., and Lewy, H.: Über Die Partiellen Differenzengleichungen Der Mathematischen Physik, Math. Ann., 100, 32–74, doi: 10.1007/BF01448839, 1928.

Deardorff, J. W.: Numerical Investigation of Neutral and Unstable Planetary Boundary Layers, J. Atmos. Sci., 29, 91–115, doi: 10.1175/1520-0469(1972)029<0091:NIONAU>2.0.CO;2, 1972.

Deardorff, J. W.: Stratocumulus-Capped Mixed Layers Derived from a Three-Dimensional Model, Boundary-Layer Meteorol, 18, 495–527, doi: 10.1007/BF00119502, 1980.

Defraeye, T., Blocken, B., and Carmeliet, J.: CFD Analysis of Convective Heat Transfer at the Surfaces of a Cube Immersed in a Turbulent Boundary Layer, Int. J. Heat. Mass. Transf., 53, 297–308, doi: 10.1016/j.ijheatmasstransfer.2009.09.029, 2010.

Degrazia, G., Bodmann, B. E. J., Wittwer, A., Dorado, R. M., Degrazia, F., Demarco, G., Roberti, D., Loredo-Souza, A. M., Azevedo, O., and Martins, L. G.: Wind Tunnel Experiments with Neutral and Convective Boundary Layer Stabilities, Am. J. Environ. Eng., 8, 154–158, doi: 10.5923/j.ajee.20180804.12, 2018.

Dong, J., Tan, Z., Xiao, Y., and Tu, J.: Seasonal Changing Effect on Airflow and Pollutant Dispersion Characteristics in Urban Street Canyons, Atmosphere, 8, 43, doi: 10.3390/atmos8030043, 2017.

Etheridge, D. and Sandberg, M.: Building Ventilation: Theory and Measurement, John Wiley & Sons, New York, 1996.

Fanger, P. O.: Thermal Comfort: Analysis and Applications in Environmental Engineering, Danish Technical Press, Aarhuus, Denmark, 1970.

Fenger, J.: Urban Air Quality, Atmos. Environ., 33, 4877–4900, doi: 10.1016/S1352-2310(99)00290-3, 1999.

Ferziger, J. H.: Large Eddy Simulation, in: Simulation and Modelling of Turbulent Flows, edited by Gatski, T. B., Hussaini, M. Y., and Lumley, J. L., ICASE/LaRC Series in Computational Science and Engineering, pp. 109–154, Oxford University Press, New York, NY, USA, 1996.

Franke, J., Hellsten, A., Schlünzen, K. H., and Carissimo, B., eds.: Best Practise Guideline for the CFD Simulation of Flows in the Urban Environment: COST Action 732 Quality Assurance and Improvement of Microscale Meteorological Models, COST Office, Hamburg, 2007.

Frigo, M. and Johnson, S. G.: FFTW: An Adaptive Software Architecture for the FFT, in: Proceedings of the 1998 IEEE International Conference on Acoustics, Speech and Signal Processing, vol. 3, pp. 1381–1384, doi: 10.1109/ICASSP.1998.681704, 1998.

Geletič, J., Lehnert, M., Krč, P., Resler, J., and Krayenhoff, E. S.: High-Resolution Modelling of Thermal Exposure during a Hot Spell: A Case Study Using PALM-4U in Prague, Czech Republic, Atmosphere, 12, 175, doi: 10.3390/atmos12020175, 2021.

Grimmond, C. S. B. and Oke, T. R.: Aerodynamic Properties of Urban Areas Derived from Analysis of Surface Form, J. Appl. Meteorol., 38, 1262–1292, doi: 10.1175/1520-0450(1999) 038<1262:APOUAD>2.0.CO;2, 1999.

Gronemeier, T. and Sühring, M.: On the Effects of Lateral Openings on Courtyard Ventilation and Pollution—A Large-Eddy Simulation Study, Atmosphere, 10, 63, doi: 10.3390/atmos10020063, 2019.

Gronemeier, T., Raasch, S., and Ng, E.: Effects of Unstable Stratification on Ventilation in Hong Kong, Atmosphere, 8, 168, doi: 10.3390/atmos8090168, 2017.

Gronemeier, T., Surm, K., Harms, F., Leitl, B., Maronga, B., and Raasch, S.: Evaluation of the Dynamic Core of the PALM Model System 6.0 in a Neutrally Stratified Urban Environment: Comparison between LES and Wind-Tunnel Experiments, Geosci. Model Dev., 14, 3317–3333, doi: 10.5194/gmd-14-3317-2021, 2021.

Hackbusch, W.: Multi-Grid Methods and Applications, vol. 4, Springer, Berlin, Heidelberg, New York, 1985.

Hall, D., Walker, S., and Spanton, A.: Dispersion from Courtyards and Other Enclosed Spaces, Atmos. Environ., 33, 1187–1203, doi: 10.1016/S1352-2310(98)00284-2, 1999.

Hang, J., Sandberg, M., and Li, Y.: Age of Air and Air Exchange Efficiency in Idealized City Models, Build. Environ., 44, 1714–1723, doi: 10.1016/j.buildenv.2008.11.013, 2009.

Hang, J., Li, Y., and Sandberg, M.: Experimental and Numerical Studies of Flows through and within High-Rise Building Arrays and Their Link to Ventilation Strategy, J. Wind. Eng. Ind. Aerodyn., 99, 1036–1055, doi: 10.1016/j.jweia.2011.07.004, 2011.

Hang, J., Wang, Q., Chen, X., Sandberg, M., Zhu, W., Buccolieri, R., and Di Sabatino, S.: City Breathability in Medium Density Urban-like Geometries Evaluated through the Pollutant Transport Rate and the Net Escape Velocity, Build. Environ., 94, 166–182, doi: 10.1016/j.buildenv.2015.08.002, 2015.

Harlow, F. H. and Welch, J. E.: Numerical Calculation of Time-Dependent Viscous Incompressible Flow of Fluid with Free Surface, Phys. Fluids, 8, 2182, doi: 10.1063/1.1761178, 1965.

Hattori, H., Yamada, S., Tanaka, M., Houra, T., and Nagano, Y.: DNS, LES and RANS of Turbulent Heat Transfer in Boundary Layer with Suddenly Changing Wall Thermal Conditions, Int. J. Heat. Fluid. Flow., 41, 34–44, doi: 10.1016/j.ijheatfluidflow.2013.03.014, 2013.

Hellsten, A., Luukkonen, S.-M., Steinfeld, G., Kanani-Sühring, F., Markkanen, T., Järvi, L., Lento, J., Vesala, T., and Raasch, S.: Footprint Evaluation for Flux and Concentration Measurements for an Urban-Like Canopy with Coupled Lagrangian Stochastic and Large-Eddy Simulation Models, Boundary-Layer Meteorol, 157, 191–217, doi: 10.1007/s10546-015-0062-4, 2015.

Hong, B., Qin, H., and Lin, B.: Prediction of Wind Environment and Indoor/Outdoor Relationships for PM2.5 in Different Building–Tree Grouping Patterns, Atmosphere, 9, 39, doi: 10.3390/atmos9020039, 2018.

Hussein, H. J. and Martinuzzi, R. J.: Energy Balance for Turbulent Flow around a Surface Mounted Cube Placed in a Channel, Phys. Fluids, 8, 764–780, doi: 10.1063/1.868860, 1996.

Kampa, M. and Castanas, E.: Human Health Effects of Air Pollution, Environ. Pollut., 151, 362–367, doi: 10.1016/j.envpol.2007.06.012, 2008.

Kataoka, H. and Mizuno, M.: Numerical Flow Computation around Aeroelastic 3D Square Cylinder Using Inflow Turbulence, Wind and Structures, 5, 379–392, doi: 10.12989/WAS.2002.5.2_3_4.379, 2002.

Kato, S., Ito, K., and Murakami, S.: Analysis of Visitation Frequency through Particle Tracking Method Based on LES and Model Experiment, Indoor Air, 13, 182–193, doi: 10.1034/j.1600-0668.2003.00173.x, 2003.

Kazak, J. K.: The Use of a Decision Support System for Sustainable Urbanization and Thermal Comfort in Adaptation to Climate Change Actions—The Case of the Wrocław Larger Urban Zone (Poland), Sustainability, 10, 1083, doi: 10.3390/su10041083, 2018.

Kurppa, M., Hellsten, A., Auvinen, M., Raasch, S., Vesala, T., and Järvi, L.: Ventilation and Air Quality in City Blocks Using Large-Eddy Simulation—Urban Planning Perspective, Atmosphere, 9, 65, doi: 10.3390/atmos9020065, 2018.

Kwak, K.-H., Woo, S. H., Kim, K. H., Lee, S.-B., Bae, G.-N., Ma, Y.-I., Sunwoo, Y., and Baik, J.-J.: On-Road Air Quality Associated with Traffic Composition and Street-Canyon Ventilation: Mobile Monitoring and CFD Modeling, Atmosphere, 9, 92, doi: 10.3390/atmos9030092, 2018.

Lamb, R. G.: A Numerical Simulation of Dispersion from an Elevated Point Source in the Convective Planetary Boundary Layer, Atmos. Environ., 12, 1297–1304, doi: 10.1016/0004-6981(78)90068-9, 1978.

Lawson, T. V. and Penwarden, A. D.: The Effects of Wind on People in the Vicinity of Buildings, in: Proceedings of the 4th International Conference on Wind Effects on Buildings and Structures, pp. 602–622, Cambridge University Press, Heathrow, 1975.

Letzel, M. O., Krane, M., and Raasch, S.: High Resolution Urban Large-Eddy Simulation Studies from Street Canyon to Neighbourhood Scale, Atmos. Environ., 42, 8770–8784, doi: 10.1016/j.atmosenv.2008.08.001, 2008.

Letzel, M. O., Helmke, C., Ng, E., An, X., Lai, A., and Raasch, S.: LES Case Study on Pedestrian Level Ventilation in Two Neighbourhoods in Hong Kong, Meteorol. Z., 21, 575–589, doi: 10.1127/0941-2948/2012/0356, 2012.

Lilly, D. K.: The Representation of Small-Scales Turbulence in Numerical Simulation Experiments, in: Proc. IBM Sci. Comput. Symp. on Environmental Sci., pp. 195–210, IBM Form 320-1951, Thomas J. Watson Res. Center, Yorktown Heights, N.Y., Nov. 14–16, 1966, 1967.

Liu, S., Luo, Z., Zhang, K., and Hang, J.: Natural Ventilation of a Small-Scale Road Tunnel by Wind Catchers: A CFD Simulation Study, Atmosphere, 9, 411, doi: 10.3390/atmos9100411, 2018.

Lo, K. W. and Ngan, K.: Characterising the Pollutant Ventilation Characteristics of Street Canyons Using the Tracer Age and Age Spectrum, Atmos. Environ., 122, 611–621, doi: 10.1016/j.atmosenv.2015.10.023, 2015.

Lo, K. W. and Ngan, K.: Characterizing Ventilation and Exposure in Street Canyons Using Lagrangian Particles, J. Appl. Meteor. Climatol., 56, 1177–1194, doi: 10.1175/JAMC-D-16-0168.1, 2017.

Lund, T. S., Wu, X., and Squires, K. D.: Generation of Turbulent Inflow Data for Spatially-Developing Boundary Layer Simulations, J. Comput. Phys., 140, 233–258, doi: 10.1006/jcph.1998.5882, 1998.

Maronga, B., Gryschka, M., Heinze, R., Hoffmann, F., Kanani-Sühring, F., Keck, M., Ketelsen, K., Letzel, M. O., Sühring, M., and Raasch, S.: The Parallelized Large-Eddy Simulation Model (PALM) Version 4.0 for Atmospheric and Oceanic Flows: Model Formulation, Recent Developments, and Future Perspectives, Geosci. Model Dev., 8, 2515–2551, doi: 10.5194/gmd-8-2515-2015, 2015.

Maronga, B., Gross, G., Raasch, S., Banzhaf, S., Forkel, R., Heldens, W., Kanani-Sühring, F., Matzarakis, A., Mauder, M., Pavlik, D., Pfafferott, J., Schubert, S., Seckmeyer, G., Sieker, H., and Winderlich, K.: Development of a New Urban Climate Model Based on the Model PALM – Project Overview, Planned Work, and First Achievements, Meteorol. Z., 28, 105–119, doi: 10.1127/metz/2019/0909, 2019.

Maronga, B., Banzhaf, S., Burmeister, C., Esch, T., Forkel, R., Fröhlich, D., Fuka, V., Gehrke, K. F., Geletič, J., Giersch, S., Gronemeier, T., Groß, G., Heldens, W., Hellsten, A., Hoffmann, F., Inagaki, A., Kadasch, E., Kanani-Sühring, F., Ketelsen, K., Khan, B. A., Knigge, C., Knoop, H., Krč, P., Kurppa, M., Maamari, H., Matzarakis, A., Mauder, M., Pallasch, M., Pavlik, D., Pfafferott, J., Resler, J., Rissmann, S., Russo, E., Salim, M., Schrempf, M., Schwenkel, J., Seckmeyer, G., Schubert, S., Sühring, M., von Tils, R., Vollmer, L., Ward, S., Witha, B., Wurps, H., Zeidler, J., and Raasch, S.: Overview of the PALM Model System 6.0, Geosci. Model Dev., 13, 1335–1372, doi: 10.5194/gmd-13-1335-2020, 2020.

Marucci, D., Carpentieri, M., and Hayden, P.: On the Simulation of Thick Non-Neutral Boundary Layers for Urban Studies in a Wind Tunnel, Int. J. Heat. Fluid. Flow., 72, 37–51, doi: 10.1016/j.ijheatfluidflow.2018.05.012, 2018.

Masson, V.: Urban Surface Modeling and the Meso-Scale Impact of Cities, Theor. Appl. Climatol., 84, 35–45, doi: 10.1007/s00704-005-0142-3, 2006.

Mills, G.: Progress toward Sustainable Settlements: A Role for Urban Climatology, Theor. Appl. Climatol., 84, 69–76, doi: 10.1007/s00704-005-0145-0, 2006.

Ming, T., Fang, W., Peng, C., Cai, C., de Richter, R., Ahmadi, M. H., and Wen, Y.: Impacts of Traffic Tidal Flow on Pollutant Dispersion in a Non-Uniform Urban Street Canyon, Atmosphere, 9, 82, doi: 10.3390/atmos9030082, 2018.

Ministerium für Verkehr und Infrastruktur Baden-Württemberg, ed.: Städtebauliche Klimafibel: Hinweise für die Bauleitplanung, Druckfrisch Verlag für Druckerzeugnisse, Stuttgart, second edn., 2015.

Moeng, C.-H. and Sullivan, P. P.: A Comparison of Shear- and Buoyancy-Driven Planetary Boundary Layer Flows, J. Atmos. Sci., 51, 999–1022, doi: 10.1175/1520-0469(1994)051<0999:ACOSAB>2.0.CO;2, 1994.

Moeng, C.-H. and Wyngaard, J. C.: Spectral Analysis of Large-Eddy Simulations of the Convective Boundary Layer, J. Atmos. Sci., 45, 3573–3587, doi: 10.1175/1520-0469(1988)045<3573:SAOLES>2.0.CO;2, 1988.

Moin, P. and Mahesh, K.: Direct Numerical Simulation: A Tool in Turbulence Research, Annu. Rev. Fluid. Mech., 30, 539–578, doi: 10.1146/annurev.fluid.30.1.539, 1998.

Müller, N., Kuttler, W., and Barlag, A.-B.: Counteracting Urban Climate Change: Adaptation Measures and Their Effect on Thermal Comfort, Theor. Appl. Climatol., 115, 243–257, doi: 10.1007/s00704-013-0890-4, 2014.

Munters, W., Meneveau, C., and Meyers, J.: Shifted Periodic Boundary Conditions for Simulations of Wall-Bounded Turbulent Flows, Phys. Fluids, 28, 025 112, doi: 10.1063/1.4941912, 2016.

Ng, E.: Policies and Technical Guidelines for Urban Planning of High-Density Cities – Air Ventilation Assessment (AVA) of Hong Kong, Build. Environ., 44, 1478–1488, doi: 10.1016/j.buildenv.2008.06.013, 2009.

Ng, E., Tam, I., Ng, A., Givoni, B., Katzschner, L., and Kwok, K.: Feasibility Study for Establishment of Air Ventilation Assessment System - Final Report, Tech. rep., Chinese University of Hong Kong, 2005.

Ng, E., Yuan, C., Chen, L., Ren, C., and Fung, J. C.: Improving the Wind Environment in High-Density Cities by Understanding Urban Morphology and Surface Roughness: A Study in Hong Kong, Landsc. Urban. Plan., 101, 59–74, doi: 10.1016/j.landurbplan.2011.01.004, 2011.

Nguyen, C. V., Soulhac, L., and Salizzoni, P.: Source Apportionment and Data Assimilation in Urban Air Quality Modelling for NO2: The Lyon Case Study, Atmosphere, 9, 8, doi: 10.3390/atmos9010008, 2018.

Nozawa, K. and Tamura, T.: Large Eddy Simulation of the Flow around a Low-Rise Building Immersed in a Rough-Wall Turbulent Boundary Layer, J. Wind. Eng. Ind. Aerodyn., 90, 1151–1162, doi: 10.1016/S0167-6105(02)00228-3, 2002.

Ok, V., Yasa, E., and Özgunler, M.: An Experimental Study of the Effects of Surface Openings on Air Flow Caused by Wind in Courtyard Buildings, Archit. Sci. Rev., 51, 263–268, doi: 10.3763/asre.2008.5131, 2008.

Oke, T. R.: Boundary Layer Climates, Routledge, London, 1987.

Oke, T. R.: Towards Better Scientific Communication in Urban Climate, Theor. Appl. Climatol., 84, 179–190, doi: 10.1007/s00704-005-0153-0, 2006.

Orlanski, I.: A Simple Boundary Condition for Unbounded Hyperbolic Flows, J. Comput. Phys., 21, 251–269, doi: 10.1016/0021-9991(76)90023-1, 1976.

Panofsky, H. A. and Dutton, J. A.: Atmospheric Turbulence: Models and Methods for Engineering Applications, John Wiley & Sons, New York, 1984.

Park, S.-B., Baik, J.-J., Raasch, S., and Letzel, M. O.: A Large-Eddy Simulation Study of Thermal Effects on Turbulent Flow and Dispersion in and above a Street Canyon, J. Appl. Meteor. Climatol., 51, 829–841, doi: 10.1175/JAMC-D-11-0180.1, 2012.

Park, S.-B., Baik, J.-J., and Ryu, Y.-H.: A Large-Eddy Simulation Study of Bottom-Heating Effects on Scalar Dispersion in and above a Cubical Building Array, J. Appl. Meteor. Climatol., 52, 1738–1752, doi: 10.1175/JAMC-D-12-0255.1, 2013.

Park, S.-B., Baik, J.-J., and Han, B.-S.: Large-Eddy Simulation of Turbulent Flow in a Densely Built-up Urban Area, Environ Fluid Mech, 15, 235–250, doi: 10.1007/s10652-013-9306-3, 2015.

Patrinos, A. A. N. and Kistler, A. L.: A Numerical Study of the Chicago Lake Breeze, Boundary-Layer Meteorol, 12, 93–123, doi: 10.1007/BF00116400, 1977.

Raasch, S. and Harbusch, G.: An Analysis Of Secondary Circulations And Their Effects Caused By Small-Scale Surface Inhomogeneities Using Large-Eddy Simulation, Boundary-Layer Meteorol, 101, 31–59, doi: 10.1023/A:1019297504109, 2001.

Raasch, S. and Schröter, M.: PALM - A Large-Eddy Simulation Model Performing on Massively Parallel Computers, Meteorol. Z., 10, 363–372, doi: 10.1127/0941-2948/2001/0010-0363, 2001.

Roache, P. J.: Computational Fluid Dynamics, vol. VII, Hermosa Publishers, Albuquerque, NM, USA, 1972.

Ronda, R. J., Steeneveld, G. J., Heusinkveld, B. G., Attema, J. J., and Holtslag, A. A. M.: Urban Finescale Forecasting Reveals Weather Conditions with Unprecedented Detail, Bull. Amer. Meteor. Soc., 98, 2675–2688, doi: 10.1175/BAMS-D-16-0297.1, 2017.

Saiki, E. M., Moeng, C.-H., and Sullivan, P. P.: Large-Eddy Simulation Of The Stably Stratified Planetary Boundary Layer, Boundary-Layer Meteorol 95, 1–30, doi: 10.1023/A:1002428223156, 2000.

Santiago, J.-L., Rivas, E., Sanchez, B., Buccolieri, R., and Martin, F.: The Impact of Planting Trees on NOx Concentrations: The Case of the Plaza de La Cruz Neighborhood in Pamplona (Spain), Atmosphere, 8, 131, doi: 10.3390/atmos8070131, 2017.

Schatzmann, M., Olesen, H., and Franke, J., eds.: COST 732 Model Evaluation Case Studies: Approach and Results, University of Hamburg, Hamburg, Germany, 2010.

Scherer, D., Antretter, F., Bender, S., Cortekar, J., Emeis, S., Fehrenbach, U., Gross, G., Halbig, G., Hasse, J., Maronga, B., Raasch, S., and Scherber, K.: Urban Climate Under Change [UC]2 – A National Research Programme for Developing a Building-Resolving Atmospheric Model for Entire City Regions, Meteorol. Z., 28, 95–104, doi: 10.1127/metz/2019/0913, 2019.

Schmidt, H. and Schumann, U.: Coherent Structure of the Convective Boundary Layer Derived from Large-Eddy Simulations, J. Fluid Mech., 200, 511–562, doi: 10.1017/S0022112089000753, 1989.

Schumann, U. and Sweet, R. A.: Fast Fourier Transforms for Direct Solution of Poisson's Equation with Staggered Boundary Conditions, J. Comput. Phys., 75, 123–137, doi: 10.1016/0021-9991(88)90102-7, 1988.

Shah, A. S. V., Lee, K. K., McAllister, D. A., Hunter, A., Nair, H., Whiteley, W., Langrish, J. P., Newby, D. E., and Mills, N. L.: Short Term Exposure to Air Pollution and Stroke: Systematic Review and Meta-Analysis, BMJ, p. h1295, doi: 10.1136/bmj.h1295, 2015.

Shi, X., Zhu, Y., Duan, J., Shao, R., and Wang, J.: Assessment of Pedestrian Wind Environment in Urban Planning Design, Landsc. Urban. Plan., 140, 17–28, doi: 10.1016/j.landurbplan.2015.03.013, 2015.

Suszanowicz, D.: Optimisation of Heat Loss through Ventilation for Residential Buildings, Atmosphere, 9, 95, doi: 10.3390/atmos9030095, 2018.

Tan, Z. and Deng, X.: Assessment of Natural Ventilation Potential for Residential Buildings across Different Climate Zones in Australia, Atmosphere, 8, 177, doi: 10.3390/atmos8090177, 2017.

Thomson, D. J.: Criteria for the Selection of Stochastic Models of Particle Trajectories in Turbulent Flows, J. Fluid Mech., 180, 529–556, doi: 10.1017/S0022112087001940, 1987.

UN-Habitat, ed.: State of the World's Cities 2012/2013, Routledge, New York, NY, 2013.

UN-Habitat, ed.: World Cities Report 2020: The Value of Sustainable Urbanization, UN-Habitat, Nairobi, Kenya, 2020.

van Aalst, R., Edwards, L., Pulles, T., De Saeger, E., Tombrou, M., and Tønnesen, D.: Guidance Report on Preliminary Assessment under EC Air Quality Directives, Technical Report 11, European Environment Agency, Copenhagen, 1998.

VDI: Environmental Meteorology - Methods for the Human Biometeorological Evaluation of Climate and Air Quality for Urban and Regional Planning at Regional Level - Part I: Climate, Tech. Rep. VDI 3787 Part 2, VDI/DIN-Kommission Reinhaltung der Luft (KRdL) - Normenausschuss, 2008.

VDI: Environmental Meteorology - Methods for Describing and Evaluating Strong and Weak Winds in Built-up Areas, Tech. Rep. VDI 3787 Part 4, VDI/DIN-Kommission Reinhaltung der Luft (KRdL) - Normenausschuss, 2020.

Weber, S. and Weber, K.: Coupling of Urban Street Canyon and Backyard Particle Concentrations, Meteorol. Z., 17, 251–261, doi: 10.1127/0941-2948/2008/0286, 2008.

Weil, J. C., Sullivan, P. P., and Moeng, C.-H.: The Use of Large-Eddy Simulations in Lagrangian Particle Dispersion Models, J. Atmos. Sci., 61, 2877–2887, doi: 10.1175/JAS-3302.1, 2004.

Wicker, L. J. and Skamarock, W. C.: Time-Splitting Methods for Elastic Models Using Forward Time Schemes, Mon. Wea. Rev., 130, 2088–2097, doi: 10.1175/1520-0493(2002)130<2088:TSMFEM>2.0.CO;2, 2002.

Williamson, J. H.: Low-Storage Runge-Kutta Schemes, J. Comput. Phys., 35, 48–56, doi: 10.1016/0021-9991(80)90033-9, 1980.

Wolf-Grosse, T., Esau, I., and Reuder, J.: Sensitivity of Local Air Quality to the Interplay between Small- and Large-Scale Circulations: A Large-Eddy Simulation Study, Atmos. Chem. Phys., 17, 7261–7276, doi: 10.5194/acp-17-7261-2017, 2017.

World Health Organization: Global Health Risks: Mortality and Burden of Disease Attributable to Selected Major Risks, Tech. rep., World Health Organization, Geneva, 2009.

Xie, X., Huang, Z., and Wang, J.-s.: Impact of Building Configuration on Air Quality in Street Canyon, Atmos. Environ., 39, 4519–4530, doi: 10.1016/j.atmosenv.2005.03.043, 2005.

Xie, Z. and Castro, I. P.: LES and RANS for Turbulent Flow over Arrays of Wall-Mounted Obstacles, Flow. Turbul. Combust., 76, 291–312, doi: 10.1007/s10494-006-9018-6, 2006.

Xie, Z.-T. and Castro, I. P.: Large-Eddy Simulation for Flow and Dispersion in Urban Streets, Atmos. Environ., 43, 2174–2185, doi: 10.1016/j.atmosenv.2009.01.016, 2009.

Yang, L. and Li, Y.: Thermal Conditions and Ventilation in an Ideal City Model of Hong Kong, Energy. Build., 43, 1139–1148, doi: 10.1016/j.enbuild.2010.06.005, 2011.

Yang, X. I. A. and Griffin, K. P.: Grid-Point and Time-Step Requirements for Direct Numerical Simulation and Large-Eddy Simulation, Phys. Fluids, 33, 015 108, doi: 10.1063/5.0036515, 2021.

Yuan, J., Farnham, C., and Emura, K.: Inter-Building Effect and Its Relation with Highly Reflective Envelopes on Building Energy Use: Case Study for Cities of Japan, Atmosphere, 8, 211, doi: 10.3390/atmos8110211, 2017.

Zauli Sajani, S., Trentini, A., Rovelli, S., Ricciardelli, I., Marchesi, S., Maccone, C., Bacco, D., Ferrari, S., Scotto, F., Zigola, C., Cattaneo, A., Cavallo, D. M., Lauriola, P., Poluzzi, V., and Harrison, R. M.: Is Particulate Air Pollution at the Front Door a Good Proxy of Residential Exposure?, Environ. Pollut., 213, 347–358, doi: 10.1016/j.envpol.2016.02.033, 2016.

Curriculum Vitae

Personal Details

Name	Tobias Gronemeier
Date of Birth	10 August 1988
Birthplace	Herford, Germany
Nationality	German

Career

since Oct 2019	Consultant at iMA Richter & Röckle GmbH & Co. KG, Freiburg, Germany
since Apr 2015	Research Associate at Leibniz University Hannover, Germany
Apr 2014 – Mar 2015	Visiting Researcher at Tokyo Institute of Technology, Japan

Education

Dec 2013	Master of Science, Meteorology, Leibniz University Hannover, Germany
Oct 2011	Bachelor of Science, Meteorology, Leibniz University Hannover, Germany
Jun 2008	Abitur, Immanuel-Kant-Gymnasium Bad Oeynhausen, Germany

Scholarships

2018	JASSO (Japan Student Service Organization) Scholarship "Short-Term Study in Japan Program".
2014	One year scholarship for postgraduates of the DAAD (German Academic Exchange Service).

Awards

2018	Best Poster-Presentation, METTOOLS X, 25–27 September 2018, Braunschweig, Germany.
2013	Best Collaboration Award, 5th International Education Forum on Environment and Energy Science, 15–19 December 2016, San Diego, CA, USA.

Publications

Journals

Gronemeier, T., Surm, K., Harms, F., Leitl, B., Maronga, B., and Raasch, S.: Evaluation of the Dynamic Core of the PALM Model System 6.0 in a Neutrally Stratified Urban Environment: Comparison between LES and Wind-Tunnel Experiments, Geosci. Model Dev., 14, 3317–3333, doi: 10.5194/gmd-14-3317-2021, 2021.

Kadasch, E., Sühring, M., Gronemeier, T., and Raasch, S.: Mesoscale Nesting Interface of the PALM Model System 6.0, Geosci. Model Dev., pp. 1–51, in press.

Maronga, B., Banzhaf, S., Burmeister, C., Esch, T., Forkel, R., Fröhlich, D., Fuka, V., Gehrke, K. F., Geletič, J., Giersch, S., Gronemeier, T., Groß, G., Heldens, W., Hellsten, A., Hoffmann, F., Inagaki, A., Kadasch, E., Kanani-Sühring, F., Ketelsen, K., Khan, B. A., Knigge, C., Knoop, H., Krč, P., Kurppa, M., Maamari, H., Matzarakis, A., Mauder, M., Pallasch, M., Pavlik, D., Pfafferott, J., Resler, J., Rissmann, S., Russo, E., Salim, M., Schrempf, M., Schwenkel, J., Seckmeyer, G., Schubert, S., Sühring, M., von Tils, R., Vollmer, L., Ward, S., Witha, B., Wurps, H., Zeidler, J., and Raasch, S.: Overview of the PALM Model System 6.0, Geosci. Model Dev., 13, 1335–1372, doi: 10.5194/gmd-13-1335-2020, 2020.

Gronemeier, T. and Sühring, M.: On the Effects of Lateral Openings on Courtyard Ventilation and Pollution—A Large-Eddy Simulation Study, Atmosphere, 10, 63, doi: 10.3390/atmos10020063, 2019.

Knoop, H., Gronemeier, T., Sühring, M., Steinbach, P., Noack, M., Wende, F., Steinke, T., Knigge, C., Raasch, S., and Ketelsen, K.: Porting the MPI-Parallelised LES Model PALM to Multi-GPU Systems and Many Integrated Core Processors - an Experience Report, IJCSE, 17, 297, doi: 10.1504/IJCSE.2018.095850, 2018b.

Barlow, J., Best, M., Bohnenstengel, S. I., Clark, P., Grimmond, S., Lean, H., Christen, A., Emeis, S., Haeffelin, M., Harman, I. N., Lemonsu, A., Martilli, A., Pardyjak, E., Rotach, M. W., Ballard, S., Boutle, I., Brown, A., Cai, X., Carpentieri, M., Coceal, O., Crawford, B., Di Sabatino, S., Dou, J., Drew, D. R., Edwards, J. M., Fallmann, J., Fortuniak, K., Gornall, J., Gronemeier, T., Halios, C. H., Hertwig, D., Hirano, K., Holtslag, A. A. M., Luo, Z., Mills, G., Nakayoshi, M., Pain, K., Schlünzen, K. H., Smith, S., Soulhac, L., Steeneveld, G.-J., Sun, T., Theeuwes, N. E., Thomson, D., Voogt, J. A., Ward, H. C., Xie, Z.-T., and Zhong, J.: Developing a Research Strategy to Better Understand, Observe, and Simulate Urban Atmospheric Processes at Kilometer to Subkilometer Scales, Bull. Amer. Meteor. Soc., 98, ES261–ES264, doi: 10.1175/BAMS-D-17-0106.1, 2017.

Gronemeier, T., Kanani-Sühring, F., and Raasch, S.: Do Shallow Cumulus Clouds Have the Potential to Trigger Secondary Circulations Via Shading?, Boundary-Layer Meteorol, 162, 143–169, doi: 10.1007/s10546-016-0180-7, 2017b.

Gronemeier, T., Raasch, S., and Ng, E.: Effects of Unstable Stratification on Ventilation in Hong Kong, Atmosphere, 8, 168, doi: 10.3390/atmos8090168, 2017c.

Knoop, H., Gronemeier, T., Knigge, C., and Steinbach, P.: Porting the MPI Parallelized LES Model PALM to Multi-GPU Systems – An Experience Report, in: High Performance Computing, edited by Taufer, M., Mohr, B., and Kunkel, J. M., vol. 9945, pp. 508–523, Springer International Publishing, Cham, doi: 10.1007/978-3-319-46079-6_35, 2016.

Gronemeier, T., Inagaki, A., Gryschka, M., and Kanda, M.: Large-Eddy Simulation of an Urban Canopy Using a Synthetic Turbulence Inflow Generation Method, J. JSCE, Ser. B1, 71, I_43–I_48, doi: 10.2208/jscejhe.71.I_43, 2015a.

Conference Contributions

Knoop, H., Hahnfeld, J., Gronemeier, T., and Raasch, S.: PALM Meets OpenACC: Performance Portability of a Real-World CFD Code, Using OpenACC for Fluid Dynamics and Atmospheric Prediction Studies: Stories from Application Developers, talk, Platform for Advanced Scientific Computing (PASC) Conference 2019, 12-14 June 2019, Zürich, Switzerland, 2019.

Gronemeier, T., Knoop, H., and Raasch, S.: PALM – a Story of Developing and Maintaining a Scientific Model System, talk, deRSE 2019 - Konferenz für ForschungssoftwareentwicklerInnen in Deutschland, 4-6 June 2019, Potsdam, Germany, 2019a.

Knoop, H., Gronemeier, T., Hahnfeld, J., and Raasch, S.: PALM4GPU - an OpenACC User Story, OpenACC API User Experience, Vendor Reaction, Relevance, and Roadmap, talk, Supercomputing Conference (SC) 2018, 11-16 November 2018, Dallas, TX, USA, 2018a.

Gronemeier, T. and Sühring, M.: Effects on Courtyard Ventilation Caused by Openings, poster, METTOOLS X, 25-27 September 2018, Braunschweig, Germany, 2018.

Gronemeier, T., Raasch, S., and Ng, E.: Effects of Sea Breeze on City Ventilation - Important for Air Ventilation Assessments?, talk, METTOOLS X, 25-27 September 2018, Braunschweig, Germany, 2018a.

Gronemeier, T., Raasch, S., and Ng, E.: Effects of Sea Breeze on City Ventilation - Important for Air Ventilation Assessments?, poster, 10th International Conference on Urban Climate/14th Symposium on the Urban Environment, 6-10 August 2018, New York, NY, USA, 2018b.

Sühring, M., Gronemeier, T., Hellsten, A., Raasch, S., and Maronga, B.: Application of an LES-LES Nesting to Study Pollutant Dispersion in Residential Areas Using the Urban Microscale Model PALM-4U, poster, 10th International Conference on Urban Climate/14th Symposium on the Urban Environment, 6-10 August 2018, New York, NY, USA, 2018.

Gronemeier, T. and Raasch, S.: Influence of Diabatic Stratification on the Ventilation of Large Cities, talk, 8th Japanese-German Meeting on Urban Climatology, 25-29 March 2017, Osaka, Japan, 2017.

Gronemeier, T. and Raasch, S.: Influence of Diabatic Stratification on the Ventilation of Large Cities, talk, 5th International Education Forum on Environment and Energy Science, 15-19 December 2016, San Diego, CA, USA, 2016c.

Gronemeier, T., Knoop, H., Knigge, C., and Steinbach, P.: Porting the MPI Parallelized LES Model PALM to Multi-GPU Systems - an Experience Report, talk, First International Workshop on Performance Portable Programming Models for Accelerators, ISC 2016, 20-23 June 2016, Frankfurt, Germany, 2016.

Gronemeier, T. and Raasch, S.: Simulation Der Urbanen Grenzschicht Bei Schwachem Wind Und Labiler Schichtung - Technische Herausforderungen, talk, DACH 2016, 14-18 March 2016, Berlin, Germany, 2016b.

Gronemeier, T. and Raasch, S.: Der Einfluss von Schatten Flacher Kumulusbewölkung Auf Die Atmosphärische Grenzschicht, talk, DACH 2016, 14-18 March 2016, Berlin, Germany, 2016a.

Gronemeier, T. and Raasch, S.: The Effects of Shadows of Shallow Convective Clouds on the Atmospheric Boundary Layer Including Feedback on the Cloud Field, poster, CFMIP Meeting on Cloud Processes and Climate Feedbacks, 8-11 June 2015, Monterey, CA, USA, 2015.

Gronemeier, T., Inagaki, A., Gryschka, M., and Kanda, M.: Large-Eddy Simulation of an Urban Canopy Using a Synthetic Turbulence Inflow Generation Method, talk, 59th Conference on Hydraulic Engineering, 10-12 March 2015, Tokyo, Japan, 2015b.

Gronemeier, T. and Raasch, S.: Shadow Effects of Shallow Convective Clouds on the Atmospheric Boundary Layer Including Feedback on the Cloud Field, talk, 2nd International Education Forum on Environment and Energy Science, 13-17 December 2013, Huntington Beach, CA, USA, 2013.

Theses

Gronemeier, T.: Die Effekte von Schatten flacher konvektiver Wolken auf die atmosphärische Grenzschicht sowie ihre Rückwirkung auf das Wolkenfeld, Master thesis, Leibniz University Hannover, Hannover, Germany, 2013.

Gronemeier, T.: Vermessung der planetaren Grenzschicht mittels Sodar, Bachelor thesis, Leibniz University Hannover, Hannover, Germany, 2011.

Other

Gronemeier, T. and others: Dataset: PALM 6.0 R3921, doi: 10.25835/0046914, 2020.

Gronemeier, T., Surm, K., Harms, F., Leitl, B., Maronga, B., and Raasch, S.: Dataset: Evaluation of the Dynamic Core of the PALM Model System 6.0 in a Neutrally Stratified Urban Environment: Simulation Input Data and Measurement Data., doi: 10.25835/0015082, 2020.

Gronemeier, T., Knoop, H., and Raasch, S.: PALM – a Story of Developing and Maintaining a Scientific Model System, doi: 10.5446/42519, 2019b.

Gronemeier, T., Böske, L., Knoop, H., Maronga, B., and Müller, R.: Urban Pollution Dispersion - Large-Eddy Simulation of a Heavy Atmospheric Pollution Release Event in an Urban Environment, doi: 10.5446/32921, 2017a.

Knoop, H., Gronemeier, T., Inagaki, A., Keck, M., Kanda, M., and Raasch, S.: Non-Cyclic Turbulent Inflow - Turbulent Inflow versus Laminar Inflow for Large-Eddy Simulations, doi: 10.5446/17746, 2015.